Methodology and phantom studies for the development and assessment of motion correction in simultaneous PET-MR

Soultanidis, Georgios

Awarding institution:
King's College London

Methodology and phantom studies for the development and assessment of motion correction in simultaneous PET-MR

Georgios Soultanidis

Division of Imaging Sciences & Biomedical Engineering

King's College London

This dissertation is submitted for the degree of

Doctor of Philosophy

University of London

December 2015

Abstract

Simultaneous PET-MR imaging has recently emerged into routine clinical use, with significant role in diagnosis and treatment. The high sensitivity of a PET scanner, combined with the anatomical and functional information given by MR can focus to a molecular level and provide simultaneous information about individual but correlated parameters. The combination of these modalities has also brought new opportunities. One of these is the potential for the MRI to capture and measure patient motion during PET scanning. This motion information, in the form of motion fields can be applied back to the PET and correct any motion artefacts created. For the success of this study many methodological problems have to be resolved. This thesis investigates the methodology for motion correction of PET data by appropriate use of MR motion information, which could in due course become a standard motion correction method for both pre-clinical and human studies. In particular, this study utilized prototype pre-clinical MR-compatible PET inserts.

Following the phantom development and during the experimental procedures, various prototype simultaneous MR-compatible PET small-diameter scanners, in conjunction with a 3T clinical MR scanner, were used to validate the phantom and evaluate several different approaches to motion correction. All scanner combinations used were a combination of a removable PET insert operating within a clinical MR scanner so it was necessary to develop robust methods to ensure spatial alignment and temporal synchronization. The data obtained from simultaneous PET and MR acquisition was arranged into gates and reconstructed by deriving motion transformations from the MR data and using this to correct the PET data

for the effects of motion using several PET reconstruction approaches. The experimental results obtained with various PET-MR systems demonstrate the feasibility of this approach and the degree of motion correction that can realistically be expected in pre-clinical PET-MR investigations.

Table of Contents

List of figures

List of tables

To my father.

Declaration

This study has been funded by Greek State Scholarship Foundation (IKY).

Georgios Soultanidis

December 2015

Acknowledgements

At this point I would like to thank my supervisors; Professor Paul Kenneth Marsden and Dr Charalampos Tsoumpas. Through these years, their scientific and ethical guidance lead this study to a conclusion. Their expertise in the field of studies gave a steady foundation for the completion of this thesis.

I wish also to acknowledge people who provided assistance and guidance throughout this thesis. I would like to thank especially Dr Jane E. Mackewn for her aid during the experimental procedures, her contribution through her knowledge upon simultaneous PET-MR experiments and the valuable discussions upon practical and theoretical aspects of Imaging. I would like to thank Professor Tobias Schaeffter, Dr Christian Buerger Dr Geoff Charles-Edwards and Dr Alkystis Phinikaridou for their valuable input in MRI acquisition methodologies. I would like to thank Dr Irene Polycarpou for giving me advice in many aspects of my work. I would like to thank Dr Lefteris Livieratos for his valuable advises and for his contribution in SPECT/CT acquisitions. Also I would like to thank Dr Christoph W. Lerche, Mr Bjoern Weissler, Prof Volkmar Schulz and Mr Richard Ayres for constructing sharing their expertise upon the HYPERimage and Hyperion-II^D PET inserts. From the PET centre I would like to acknowledge Dr Paul Schleyer for his contribution with the clinical PET/CT scans and Philip Halsted for his contribution in hardware equipment. I would like to acknowledge Dr Istvan Szanda, for his assistance in preclinical PET imaging, using nanoPET. Finally, I would like to thank Dr Andrew King and Dr Christoph Kolbitsch for the valuable and fruitful discussions.

I dedicate this thesis to my family but especially to my father's memory.

Chapter 1

Introduction

1.1 Positron Emission Tomography

Positron Emission Tomography (PET) has an established role for the imaging and evaluation of cancer and also in cardiology and neuropsychiatric diseases. It is also widely used for clinical research in these areas. The use of PET with the proper radio-labelled molecule can give information about the function of an organism and can highlight abnormal function. The information obtained by PET gives the intensity of normal or abnormal metabolic activity inside the human body. For that reason, the best possible image quality is essential. Diagnosis of abnormalities is done by expert physicians and after visual inspection, their conclusions are recorded. Also, some tools are used for the better understanding and quantitative assessment of the radiotracer distributions. The most common is the use of a standardized uptake value (SUV). This is usually defined as the concentration of activity in the region of interest divided by the the average activity concentration in the entire body. SUV gives a numerical representation of which areas may be considered as lesions (in case of cancer). These numbers though are affected by external factors, such as photon attenuation and motion of the patient.

These factors can be faced as individual or interrelated, where motion brings alterations

to the physical structure of the organism and therefore also to the attenuation map. These effects change the measured SUV of the patient. The final image spreads over a larger area and the image intensity is blurred as a consequence of motion. The clinical result can be the underestimation of potentially malignant areas inside the image and underestimation of the disease severity.

1.1.1 Motion Capture

To capture the motion that is to be used as an input to any motion correction methodology requires the appropriate hardware and an established methodology. The most important motions are respiratory motion and the cardiac cycle. These motions are periodic and most likely to cause blurring to the PET images. Methods to capture respiratory motion include the use of respiratory flow meters, pressure belts or infra-red cameras to capture the rib cage extension or 4 dimensional Computed Tomography (CT) for the cinematic capture of respiratory motion. Another modality capable of capturing motion information is Magnetic Resonance Imaging (MRI). This modality, free of extra radiation, can provide motion information in every direction within the patient and continuously for long periods. This ability is a very beneficial factor, as it can be exploited in hybrid PET-MR systems.

1.2 Simultaneous PET-MR

PET is a modality that provides functional information and not anatomical. For that reason, the common anatomical modality used in conjunction with PET imaging is a sequentially acquired anatomical CT scan. A recent development in preclinical and clinical imaging is PET-MR; a hybrid system, capable of acquiring with both modalities simultaneously or sequentially. A direct benefit of this procedure is the reduction of administrated radiation dose to the patient. Along with the development of applications for this system, motion

capture can be used for the compensation of displacement during respiratory motion.

1.3 PET Motion Correction

Errors due to motion can be corrected with the use of specialized algorithms, which allow motion information to be incorporated into the PET reconstruction. Motion correction usually requires the PET data grouped into different clusters, sharing a similar characteristic. These are called "gates". Each gate corresponds to a certain phase or amplitude of a motion cycle. After that, algorithms can correct the data, according to motion information provided by the complementary modality, in this case dynamic MR.

1.4 Achievements described in the thesis

This thesis is concerned with the experimental development of hardware and methodologies to compensate motion information during simultaneous PET-MR acquisition.

A promising application for the simultaneous PET-MR is PET motion correction which requires to be developed and validated upon practical and technical issues in a controlled environment. In this thesis, many of these technical difficulties emerged during the utilization of a novel, non-rigid and deformable phantom. The purpose of this phantom is to mimic the PET-MR imaging and elastic properties of human tissue. For this development, a methodology has been generated to produce deformable phantoms, in a variety of shapes and with several distribution patterns of PET radiotracer, for simultaneous PET-MR imaging. The deformation of these phantoms is utilized by MR compatible motor units that can be programmed to perform a variety of motion patterns. During this thesis, multiple MR-compatible PET scanners have been used and features like temporal synchronization and spatial alignment had to be established prior to any motion correction experiment. Nevertheless, the experiments follow an incremental rise of complexity and realism for PET and

MR acquisition protocols. These experiments demonstrate the quantitative improvements of PET motion correction using MR motion data, even though these are limited due to the quality of PET data acquired on the small prototype PET scanners used.

The products of this study include:

- The introduction of a novel concept, where the PET phantom is flexible MR visible and compatible.
- The creation of a novel phantom, in solid but elastic form, capable of supporting motion correction studies with simultaneous PET-MR systems.
- Development of preparation methods to prepare, label and use this phantom.
- Exploration of multiple roles of this phantom, where PET-MR was in the epicentre, followed by other imaging modalities.
- Demonstration of the physical properties of this phantom; in particular elasticity and non-compressibility.
- Development of motor units, functional within MR environment, capable of reproducing realistic motion patterns.
- The establishment of a new acquisition methodology for truly simultaneous PET-MR scans, with continuous real time motion for three generations of PET inserts.
- The assessment and solution of many practical issues, regarding the implementation and assessment of PET-MR motion correction, such as temporal synchronization and spatial alignment and the impact of motion correction on the final reconstructed image quality.

The following is a summary, organized by chapter of the objectives and the necessary steps taken towards these achievements.

Chapter 2 gives a brief analysis of the physics behind PET imaging and MR imaging including the possibilities and the limitations of the modalities.

Chapter 3 is concerned with the creation of non rigid phantoms. The phantom technical characteristics are characterized in detail and optimized.

Chapter 4 describes simultaneous 2D PET-MR acquisition with use of the PANDA 2-D MR compatible PET scanner. This experimental procedure marks the initial step for understanding the implications of a simultaneous acquisition of a continuously moving non-rigid phantom, and subsequent MR-based motion correction.

Chapter 5, extends this work to a 3D PET-MR scanner; the HYPERimage MR-compatible PET insert. In this chapter, methods for creating variable motion of a non-rigid PET-MR visible phantom and imaging this simultaneously with PET and MR are developed, requiring many practical issues to be solved in order to prepare the data for motion correction. Motion correction is then performed and assessed, using two established algorithms.

Chapter 6, contains the resulting data for simultaneous PET-MR acquisitions with use of Hyperion-II^D, a new generation digital SiPM PET insert with improved performance and much longer axial field of view. In this chapter, motion correction is applied to PVA phantom, where all the previous practical solutions being applied for maximum accuracy, prior to MR-based motion correction using the RTA algorithm.

Chapter 7, provides a general discussion upon the results and general conclusion with future perspectives.

Finally, The *Appendix* contains the source code, used to generate motion with the stepper and servo motor.

1.5 Contributors to the Thesis

This thesis is the work of the candidate, though some areas were aided by specialized people or software. In hardware, Dr J. E. MacKewn provided her knowledge and experience upon

the use of the PANDA II PET insert. Her contribution includes the acquisition handling of PET and signal processing until the production of the sinograms. Dr Paul Schleyer provided his assistance to perform the CT scans for the characterization of the PVA phantom, with the clinical PET/CT scanner. Mr Philip Halsted contributed into the design and production of experimental components.

Philips GmbH Innovative Technologies Aachen provided the HYPERimage PET insert, the Hyperion-II^D, and support was provided by Prof Volkmar Schulz, Mr Bjoern Weissler, Mr Pierre Gebhardt, Dr Ch. Lerche and Mr R. Ayres during the experiments. The original code for conversion of HYPERimage listmode to sinogram was generated by Dr J. E. MacKewn in " Interactive Data Language" (IDL) and translated by the candidate into C++ and implemented as a STIR library.

Prof Tobias Schaeffter and Dr Christian Buerger provided the basic MR sequences used for the dynamic PET-MR experiments. The sequence for relaxation time properties of PVA was developed by Professor Rene Botnar and executed by Dr Alkystis Phinikaridou. SPECT/CT acquisitions were performed by Ms S. M. Gould and Dr Lefteris Livieratos.

In software contributions, the open source Software for Tomographic Image Reconstruction (STIR) library (Thielemans et al. 2012) was used for the data simulations and reconstructions (http://stir.sourceforge.net/). The reconstruction for Hyperion-II^D PET insert was developed by Dr Andree Salomon. Rigid registration was performed with use of Image Registration toolkit (IRTK)(http://www.doc.ic.ac.uk/ dr/software/). The non-rigid registration of the MR data was performed with use of an open access software (Buerger *et al.* 2011) availiable online (https://www.isd.kcl.ac.uk/internal/hyperimage/). Dr Charalampos Tsoumpas and Dr Irene Polycarpou contributed their knowledge about motion correction using MR data.

1.6 Funding bodies

This work was supported in part by FP7 project SUBLIMA (No. 241711, www.sublima-pet-mr.eu) and HYPERimage (No. 201651, www.hybrid-pet-mr.eu). The candidate was individually funded by the Greek State Scholarship Foundation (IKY), Greece.

1.7 Publications and conference presentations

1. **Soultanidis G.M.**, MacKewn J.E., Tsoumpas C. and Marsden P.K., "*PVA cryogel for construction of deformable PET-MR visible phantoms*" IEEE *Trans in Nucl Science*, 60 (1), art. no. 6423849, pp. 95-102, February 2013

2. Mackewn J.E., Lerche C.W., Weissler B., de Rosales R.T.M., Phinikaridou A., Salomon A., Ayres R., Tsoumpas C., **Soultanidis S.M.**, Schaeffter T, Schulz V. and Marsden P.K.,"*PET Performance Evaluation of a pre-clinical SiPM based MR-compatible PET scanner*" IEEE *Trans in Nucl Science*, 62 (3), pp. 784-790, June 2015

3. Weissler B., Gebhardt P., Lerche C.W., **Soultanidis G.M.**, Wehner J, Heberling D. and Schulz V.,"*PET/MR Synchronization by Detection of Switching Gradients*", IEEE *Trans in Nucl Science*. 62 (3), pp. 650-657, June 2015

4. **Soultanidis G.M.**, Mackewn J.E., Lerche C.W., Tsoumpas C., Buerger C., Szanda I., Halsted P., Schaeffter T., Schulz V.and Marsden P.K.,"*Design and development of phantoms capable of continuous motion during simultaneous PET-MR acquisitions*",in 2011 IEEE Nuclear Science Symposium Conference Record, Valencia, Spain (oral). (in conference proceedings)

5. **Soultanidis G.M.**, Mackewn J.E., Tsoumpas C., Halsted P. and Marsden P.K.,"*Development and Characterization of a non-rigid PVA cryogel phantom for simultaneous PET-MR*

acquisition,in 2012 IEEE Nuclear Science Symposium, Anaheim, United States of America (oral).

6. Mackewn J.E., Lerche C.W., Sunassee K., de Rosales R.T.M., Phinikaridou A., Salomon A., Ayres R., Tsoumpas C., **SouItanidis G.M.**, Schaeffter T., Marsden P.K. and Schulz V., "*PET performance evaluation of a pre-clinical SiPM based MR-compatible PET scanner*",in 2012 IEEE Nuclear Science Symposium Conference Record, Anaheim, United States of America (poster). (in conference proceedings)

7. **Soultanidis G.M.**, Polycarpou I., Weissler B., Lerche C. W., Mackewn J.E., Tsoumpas C., Schulz V. and Marsden P. K., " *Demonstration of motion correction for PET-MR with PVA cryogel phantoms*", in 2013 IEEE Nuclear Science Symposium Conference Record, Seoul, Korea, (poster) (in conference proceedings)

8. Gould S.M., **Soultanidis G.M.**, Marsden P. K. and Livieratos L.,"PVA Cryogel Test Objects for Image-Based Quantification in Nuclear Medicine", in 2014 IEEE Nuclear Science Symposium Conference Record, Seattle, United States of America (poster).

9. Weissler B., Gebhardt P., Lerche C.W., **Soultanidis G.M.**, Wehner J, Heberling D. and Schulz V.,"*PET/MR Synchronization by Detection of Switching Gradients*", EJNMMI Physics, PSMR-4014 conference, Kos-Greece (oral)

Chapter 2

Theory and Background

Medical imaging modalities and methods help the diagnosis and treatment for various types of diseases. The continuous improvement and adaptation of these systems is important to increase their effectiveness. Positron Emission Tomography (PET) and Magnetic Resonance Imaging (MRI) are two methods of imaging, aiming towards the extraction of valuable information for the patient. PET imaging targets physiology and metabolism. MR can provide such information as well but with complementary anatomical information. In the past PET and MR have started as individual systems, with distinct roles. The technological evolution of solid state photo-detector has resulted in a hybrid system, capable of performing both PET and MR simultaneously. PET-MR systems can be used primarily for cancer imaging, but also other applications, such as imaging of heart and brain. A potentially important benefit is motion estimation, as it is captured by MR. This chapter describes the two imaging systems, including the physics background, the current instrumentation and future perspectives of this field of imaging. Because the components of a hybrid PET-MR scanner do not share a long history of coexistence, both PET and MR will be described as independent systems before the combining of the technologies is discussed.

2.1 Nuclear Physics

2.1.1 The positron

In the 1920s the English theoretical physicist Paul Dirac (1902-1984) developed a version of quantum mechanics that incorporated special relativity. This theory explains the origin of the electron's spin and its magnetic moment. However, Dirac's relativistic wave equation required solutions corresponding to both positive and negative energies for free electrons. This is observed from the expression for the total relativistic energy of an electron, which has both positive and negative roots.

$$E = \pm\sqrt{p^2c^2 + m_e^2c^4} \tag{2.1}$$

where E is the energy, p is a particle's energy state, c is the constant speed of light and m_e is the mass of the particle. The electron's antiparticle, the positron, has a rest energy of 0.511 MeV and a positive charge of $+1.60 \times 10^{-19}$ C (Dirac, 1931). An experimental observation was performed by Carl Anderson in 1932. In this experiment, Anderson observed the positron, as predicted by Dirac (Anderson, 1932). Positrons can result from pair production or radioactive decay. During pair production, a high energy gamma-ray photon interacts with a nucleus, and an electron-positron pair is created. Because the total rest energy of the electron – positron pair is:

$$2m_ec^2 = 1.02MeV \tag{2.2}$$

The photon must have at least this energy to create an electron-positron pair. In accordance with Einstein's relationship $E = mc^2$, the excess energy of the gamma-ray photo is transferred as kinetic energy to the produced particles. The reverse process can also occur. Under the proper conditions, an electron and a positron can annihilate each other to produce

two gamma-ray photons with a combined energy of 1.02 MeV (Sodickson et al., 1961).

Radioactive decay is another method of positron production, resulting from nuclear instability. The stability of a nucleus is determined by the combination of protons and neutrons. The "line of stability" is indicated when the neutron-proton ratio is around 1 for low Z nuclide and 1.5 for high. The higher neutron-proton ratio in heavier elements is to offset the Coulombic repulsive forces between protons by increasing the separation. Nuclei with odd neutron and proton number tend to be unstable where the opposite gives frequently stability (Bushberg, 1994).

In an unstable state, an atom can decay to another, more stable state. During this procedure, the nucleus of the atom transforms into a different element and excess energy or particles are emitted to the environment. This process is called radioactive decay. The products of this decay may include alpha, beta or gamma radiation, including the corresponding antiparticles. The decay process can be repeated multiple times, until the nucleus reaches a stable state. Also, each nucleus has a certain decay rate. The definition of this rate can be given from the half-life. Half-life ($T_{1/2}$) is the time required for a radionuclide to decay to 50% of its initial activity levels. The relationship correlation between decay and Half life can be described in the following equations in correlation with the decay constant λ.

$$T_{1/2} = \ln 2/\lambda \tag{2.3}$$

$$\lambda = \ln 2/T_{1/2} \tag{2.4}$$

With this information given, a positron emitting isotope can be used for the production of annihilation photons. In Table 2.1 we present a selection of positron emitting radionuclides (Cherry et al., 2012).

The distance covered by the positron, between the emission and the annihilation is related with its emission energy. The maximum energy of emission among clinically used

Radionuclide	Half-life	Maximum β^+ Energy	Production
^{11}C	20.4 min	960 keV	Cyclotron
^{13}N	9.96 min	1.19 MeV	Cyclotron
^{15}O	123 *s*	1.72 MeV	Cyclotron
^{18}F	110 min	635 keV	Cyclotron
^{62}Cu	9.74 min	2.94 MeV	Generator (^{62}Zn)
^{64}Cu	12.7 hr	580 keV	Cyclotron
^{68}Ga	68.3 min	1.9 MeV	Generator (^{68}Ge)
^{76}Br	16.1 hr	3.7 MeV	Cyclotron
^{82}Rb	78 *s*	3.35 MeV	Generator (^{82}Sr)
^{124}I	4.18 days	1.5 MeV	Cyclotron

Table 2.1 Positron emitting radionuclides

radio-nuclide ranges from 0.5 to 5 MeV. The emission energy of positrons though is described by an energy spectrum. The range of a positron is comparable with an electron of the same energy. Also, like the electron, the positron's path can be described as convoluted with multiple deflections. The final positron range is calculated as the distance between the emission and annihilation position of a positron. This may vary, according to the emission energy and the material of the medium (Serway and Jewett, 2004).

2.1.2 Interaction of gamma radiation with matter

The interaction of the 511 keV gamma photons with the environment will determine the path and use of them. The most common interactions of a 511 keV gamma photon with matter are presented in figure 2.1.

1) Photoelectric: During the interaction, the entire energy of the photon is absorbed by an atom. With the photon fully absorbed, the energy is transferred to an ejected electron. This electron is called *photoelectron*.

2) Compton scattering: It describes the interaction between a photon and an outer shell electron of an atom (i.e. essentially unbound). During this interaction, the photon does not disappear. It is deflected by an angle θ and part of its energy is transferred to the recoil

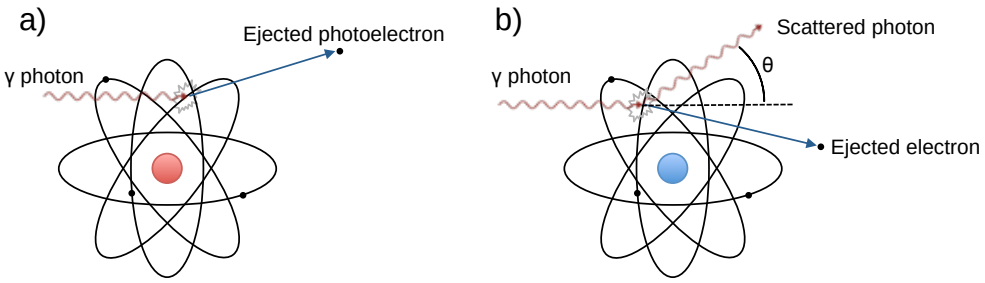

Fig. 2.1 Dominant interactions of 511 keV gamma photons with atoms a) photoelectric and b) Compton scatter

electron. The energy of the scattered photon is related to the scattering angle and the original energy. The mathematical formula is:

$$E_{sc} = \frac{E_0}{1+\left(E_0/m_e c^2\right)(1-\cos\theta)} \tag{2.5}$$

where E_{sc}, c is the constant for the speed of light and E_0 are the scattered and initial photon energies in *electron volts* respectively, and c is the constant for the speed of light.

2.1.3 Attenuation Coefficient

For a photon beam passing through matter, any interaction with it depends upon the initial photon energy as well as the composition of the medium. This decay of intensity is the attenuation effect. Attenuation is a probabilistic effect. Thickness, atomic mass, atomic number Z and density are the key factors to determine the intensity losses. When the photon beam is monoenergetic, the loss of intensity can be described with an exponential equation:

$$I(x) = I(0)^{-\mu_l x} \tag{2.6}$$

where $I(x)$ is the beam intensity after crossing x mm of the medium, $I(0)$ is the intensity before the crossing through the medium and μ_l is the linear attenuation coefficient (cm^{-1}). The attenuation coefficient therefore is a factor providing the means to predict any losses of

intensity due to interaction of gamma photons with matter.

2.2 Positron Emission Tomography

In the previous section we described positron annihilation and the generation of two anti-parallel photons of 511 keV. Coincidence detection of these gamma rays is the key principle of Positron Emission Tomography (PET). A PET scanner consists of a ring of detectors, surrounding the subject of study. The main purpose of this ring is to detect in coincidence pairs of annihilation photons originating from a positron annihilation event during the acquisition. After tomographic reconstruction of data, an image is created that represents the original distribution of the positron emitting radionuclide inside the subject.

The design of a standard PET scanner is presented in figure 2.2. The basic component and building block of a PET scanner is the detection module that detects individual 511 keV gamma rays. The detection module is presented in figure 2.3. From the crystal component to the electronics readout and storage system, each component of a PET scanner is optimized for optimum performance (Cherry et al., 2012).

2.2.1 PET scanner building blocks

The instrumentation of most PET systems can be divided into 3 main elements; the scintillation crystal, the photodetector and the readout/data recording system. The scintillation crystal and photodetector have the most influence on the properties and performance of the system. The following paragraphs give a brief description of these components.

2.2.1.1 Scintillation crystal

The first step in the detection of a 511 keV gamma ray is ionization within the scintillator. When ionization occurs inside a material, the electron causes neighbouring atoms and

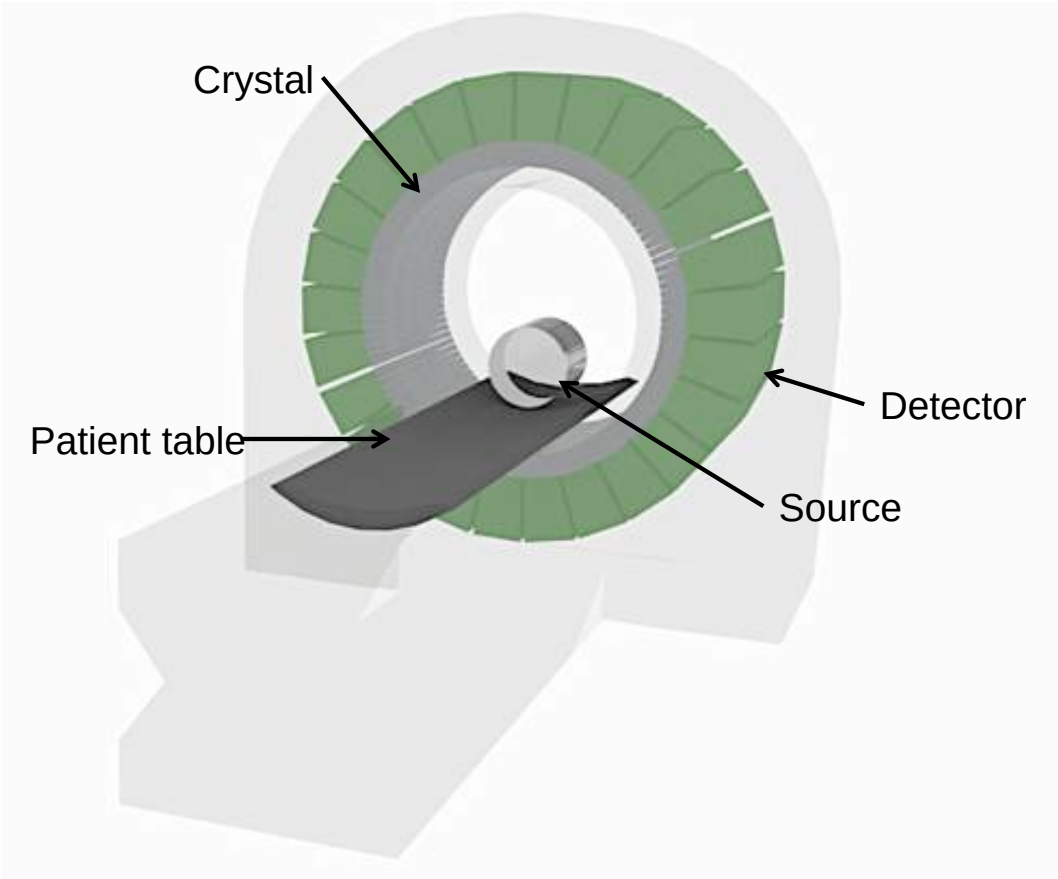

Fig. 2.2 Transparent representation of a PET scanner

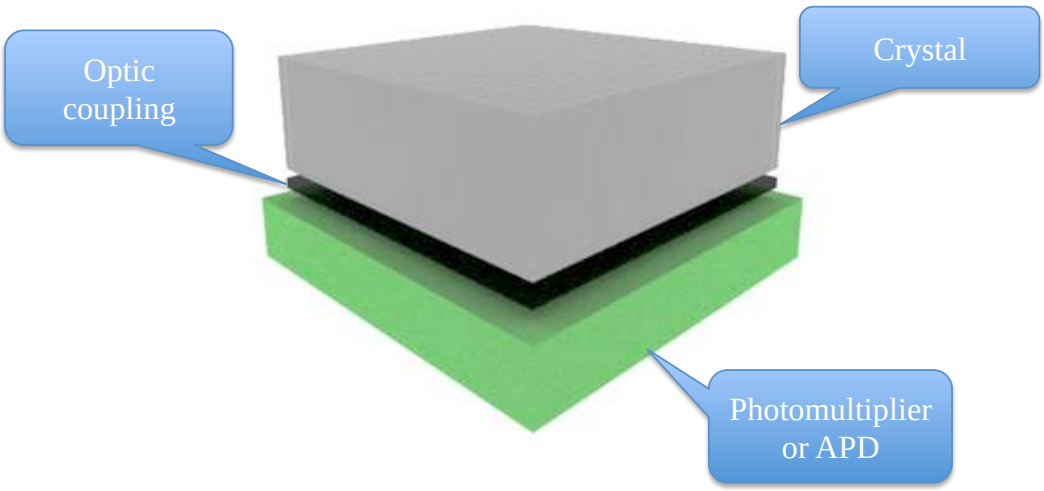

Fig. 2.3 PET scanner basic components

molecules to an excitation state. During the de-excitation energy is released. In certain materials such as scintillators, this energy is released as light inside the visible light spectrum. The most common form of scintillator in PET imaging is an inorganic crystal with high atomic number and high density. In any application of nuclear medicine, when a scintillation event takes place, the total yield of light from the interaction is proportional to the total energy deposited during the interaction. The outcome of this event is a limited number of photons, ready to be detected by the photomultiplier or other types of photodetector.

In Positron Emission Tomography, a photon has energy of 511 keV. This energy is higher than the common 140 keV of a SPECT camera or 120 keV peak in CT. Therefore, NaI, the most common crystal for nuclear medicine is not suitable for use. The crystals have to fulfil the criteria of high stopping power, sufficient light yield, and fast response time. Even if NaI has high light yield, the stopping power and the response time at 511 keV are poor. Bismuth Germanate (BGO) crystals have higher stopping power but the light yield is lower and response time are slower, by comparison with other crystals. Lutetium oxyorthosilicate (LSO) provides good stopping power, acceptable light yield and fast response time and this has become the most widely used scintillator for PET. Similar characteristics are observed in lutetium-yttrium oxyorthosilicate (LYSO) crystal.

2.2.1.2 Photodetectors

The photodetector is responsible for the conversion of an optical signal from the scintillation into an electrical signal. The most common photodetector in nuclear medicine is the photomultiplier. Figure 2.4 gives a graphical representation of a cross-section. The important parts of a photomultiplier are: the photocathode, the dynodes and the anode. The conversion process begins with the first interaction of an optical photon with the photocathode and the creation of one or more photo-electrons. These photo-electrons escape the photocathode and collide with the first dynode as they are attracted by the high voltage. The repetition

of this process brings a situation of multiplication between dynodes, producing a substantial amount of electrons and signal that can be measured by the readout electronics. Many pre-clinical PET scanners tend to use position sensitive photomultipliers as they are very compact.

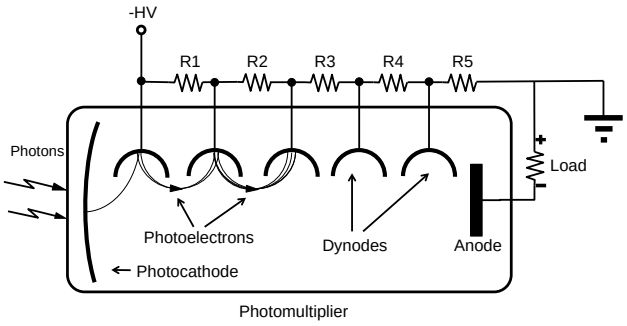

Fig. 2.4 Cross section of a photomultiplier

There is a trend to replace photomultipliers with solid state photo-detectors in PET, initially with the use of an avalanche photodiode (APD) photo-detector. The APD is a promising tool because of its compact size, the possibility of mass production and cost reduction. A disadvantage is the small sensitive area and the very low gain compared to the photomultiplier tubes. The APD is used mostly in linear mode, with the possibility of achieving Geiger mode by increasing the bias voltage above the breakdown voltage (Renker, 2002). Finally, an advantage of an APD is the capability to function inside a magnetic field. Studies have investigated the possibility of using APD inside strong magnetic fields with acceptable degradation of the acquired data (Pichler et al., 1998).

The advanced version of an APD is the silicon photomultiplier (SiPM). It consists of an array of small APDs. The density to this detector is from 500 to 4000 APDs per mm^2. Each of these APDs is operated in Geiger mode, with voltage above the breakdown voltage. With a single optical photon interaction, the cell triggers, by producing an avalanche current. Finally, the current is limited by a resistor connecting the cell and the conductive grid on the front side. The final signal is the superposition of all the firing cells. Because the number

of cells to fire corresponds to the number of photons detected, this compensates the lack of the dynamic range of each single APD. This setup results in an intrinsic gain which is between 10^5 to 10^6 and is more stable with respect to temperature compared to the APD (Buzhan et al., 2006). The most advanced version of SiPM until now is the Digital SiPM. The Digital SiPM, by integrating the signal digitization into the detector eliminates the need of a readout ASIC (Frach et al., 2009).

2.2.2 Scatter and random events

In addition to the true coincidences there are also scattered and random coincidences, as shown in Figure 2.5. Both of these can be corrected for, but they still reduce the signal to noise ratio (SNR) in PET images.

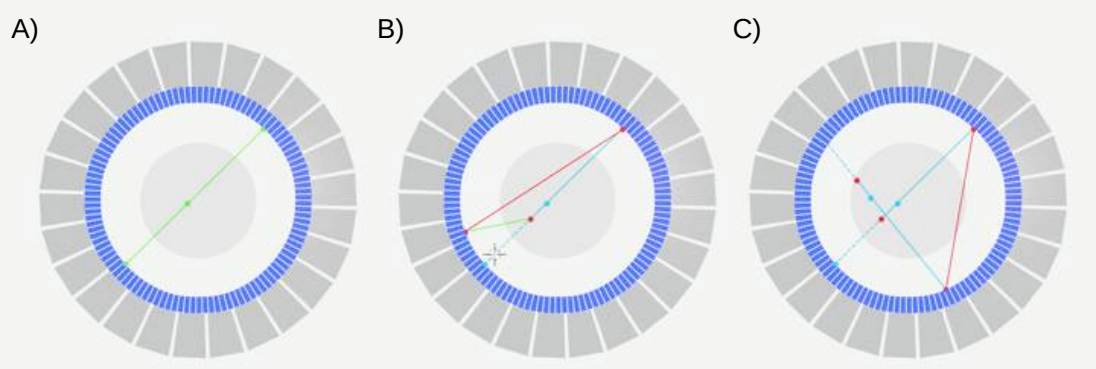

Fig. 2.5 Photon pair detection, where A) is a true pair detection, B) is a false (red line) after single scatter (red dot) and C) is false (red line) after two random photon detections

2.2.2.1 Data readout

Each coincidence pair corresponds to detection along a given line of response (LOR) between two detectors. We can store these data in two ways: as a histogram, where each element corresponds to a LOR, or by recording each coincidence pair individually in a long list. These two methods are referred as sinogram or list-mode acquisition.

2.2.2.2 Sinogram format

A sinogram is the most common method to store PET data. Figure 2.6 gives a representation of the sinogram. Given that in the middle of the scanner there is an emitting object. The emission is approximately isotropic. In the simple case of a 2D scanner, each LOR can be represented by the polar coordinates (x',θ). θ is defined as the angle of the LOR with the x axis of the Cartesian plane and x' as the distance of the LOR from the centre of the Cartesian plane. Each angle θ corresponds to different row in the sinogram, and each x' to each column. The numbers in a sinogram represent the total number of interactions that happen along the given LOR. There is a 2D sinogram like this for every 2D imaging plane in the scanner, For 3D acquisition additional sinograms are required to store data acquired in angled planes between scanner rings.

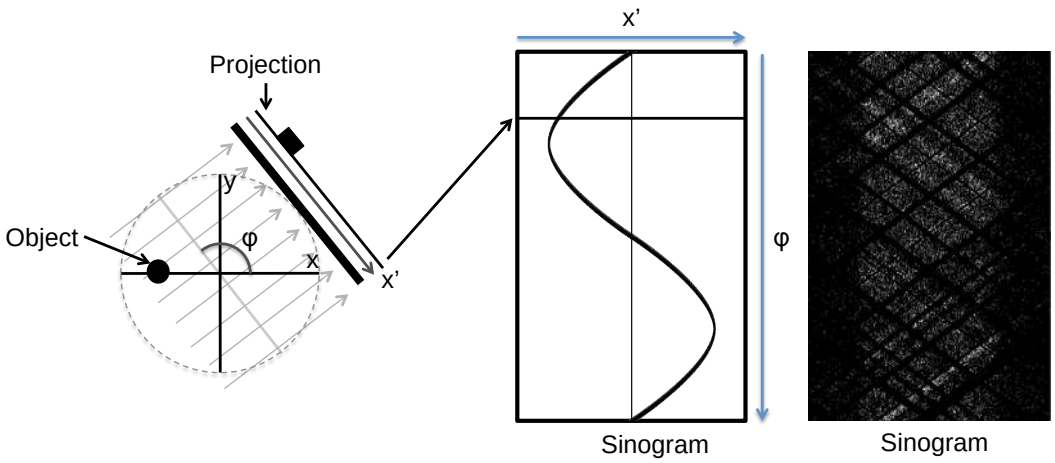

Fig. 2.6 Forward projection of an object and generation of a sinogram

2.2.2.3 Listmode format

Listmode acquisition is a data storage method, applied for clinical and preclinical PET systems. The difference with sinogram is that every event is stored as an individual event and it is not histogrammed as in the sinogram. The listmode file format has the advantage that

the user may choose to obtain additional information about each coincidence pair such as photon energies, time difference between photons arrival or global time of the PET system. Listmode also allows the data to be divided up into time frames that are chosen after the acquisition has been completed. Naturally, listmode files contain information about the detected LOR either with format similar to sinograms (x', θ) or by directly storing the coordinates (or a label) of each detector. The reconstruction algorithm must have the information on how to interpret a given listmode format to geometrical information.

2.2.2.4 Reconstruction

The information gathered and stored either in sinograms or listmode files can be used for the reconstruction of the distribution inside the field of view. Figure 2.7 gives a simple representation of PET reconstruction with the backprojection algorithm with 6 views. The equation of backprojection for N views is described by:

$$f'(x,y) = \frac{1}{N} \sum_{i=1}^{N} p(x\cos\theta + y\sin\theta, \theta) \tag{2.7}$$

where θ represents the projection angle, $p(r,\theta)$ is the sinogram and $f'(x,y)$ is the approximation of the true radioactivity distribution.

The simple backprojection gives a very blurred reconstruction. Pre-filtering of the sinograms leads to filter back projection (FBP), a common reconstruction algorithm. The filtering removes the backprojection lines leaving an accurate image of the object itself.

The second method of reconstruction is iterative reconstruction. Iterative reconstruction benefits against analytic are; the improvement signal to noise ratio, where the reconstructed image does not have the streak artefacts of an analytic reconstruction. Also, iterative reconstruction allows the incorporation of corrections, such as the detection efficiency map, the attenuation correction or Point Spread Function (PSF) correction algorithms (Vandenberghe et al., 2001). This method proceeds by iterations. In one iteration, it forward projects an

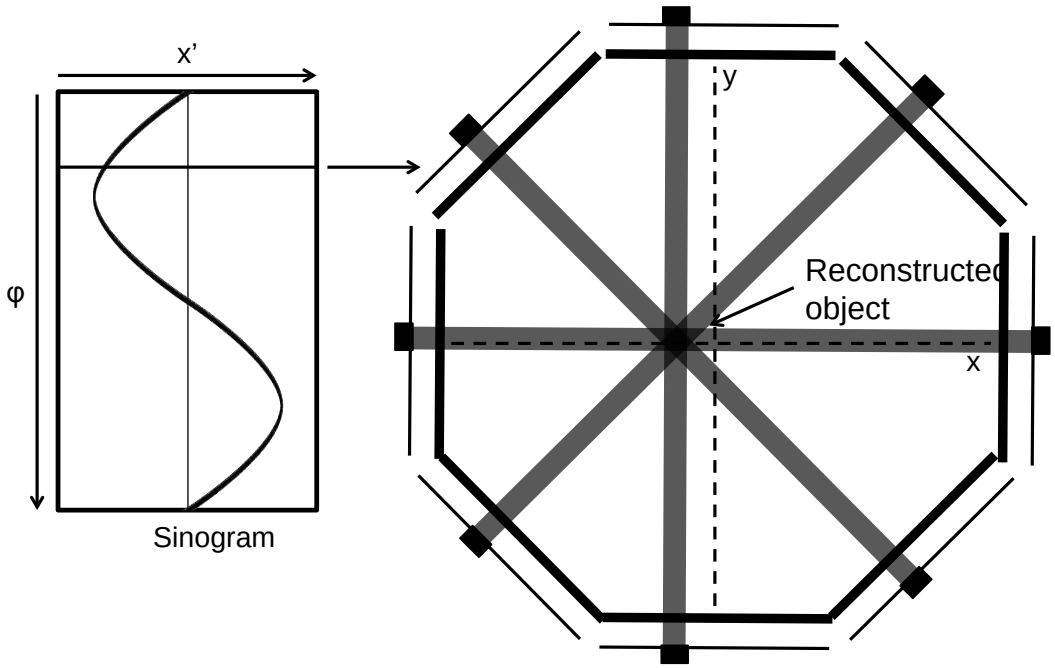

Fig. 2.7 Reconstruction of object with use of back projection

estimate of the object and compares the produced sinogram with the acquired data. The result of this comparison is used to create a better estimate of the object, which is the input for the next iteration. The final goal is to maximize the convergence with the acquired data. This is the basis of the Expectation Maximization (EM) algorithm.

The most common iterative reconstruction algorithm on clinical scanners is the Ordered Subsets Expectation Maximization (OSEM) algorithm. The difference of it with the simple EM is the grouping of projection data into different subsets. A pass through all the specified subsets is an iteration. The use of subsets improves the execution time, comparing with standard EM (Hudson and Larkin, 1994). Also, images created with the use of OSEM tend to have less noise than FBP. The extra benefit is that with iterative reconstruction, motion modelling can be included to the reconstruction (Manjeshwar et al., 2006).

2.3 Magnetic Resonance Imaging

Nuclear Magnetic Resonance (NMR) of hydrogen nuclei at certain frequencies is the basis of MRI or Magnetic Resonance Imaging - a method to obtain information about the surrounding environment and not the nuclei. This section is focused upon the physics behind MR, the image acquisition methodology and instrumentation, and its potentials and limitations. The basic components of an MR scanner are given in figure 2.8.

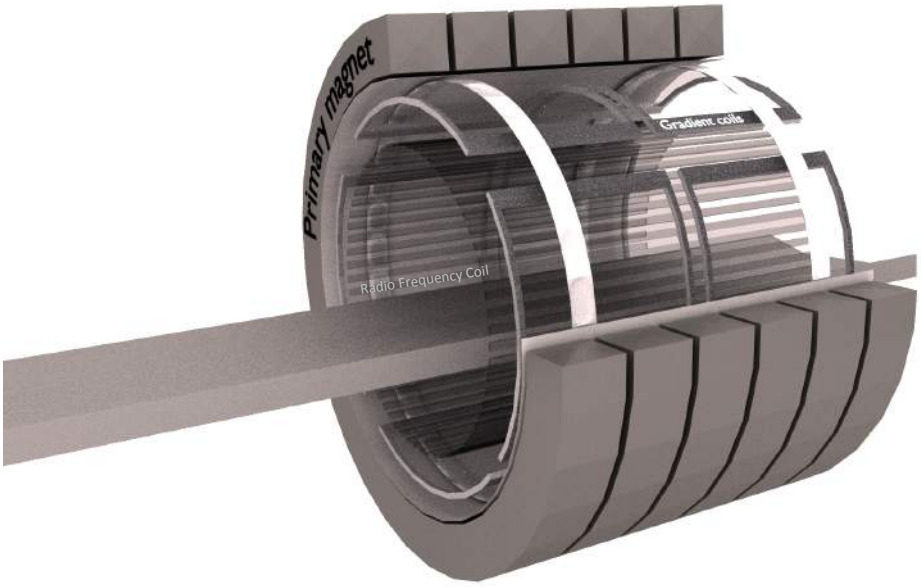

Fig. 2.8 MRI cross section

2.3.1 Larmor frequency

Hydrogen has the smallest atomic mass, with one proton. The hydrogen atom acts like a magnet. In normal environmental conditions shown in figure 2.9 the magnetic poles of each hydrogen atom have random orientations. When a strong, static magnetic field is introduced, hydrogen nuclei tend to align their magnetic poles with the lines of this magnetic field. The nuclei align parallel or anti-parallel with the magnetic field in two different energy states.

The ratio of protons aligning parallel or anti-parallel to the magnetic field depends on the strength of the field and the thermal energy of the nuclei.

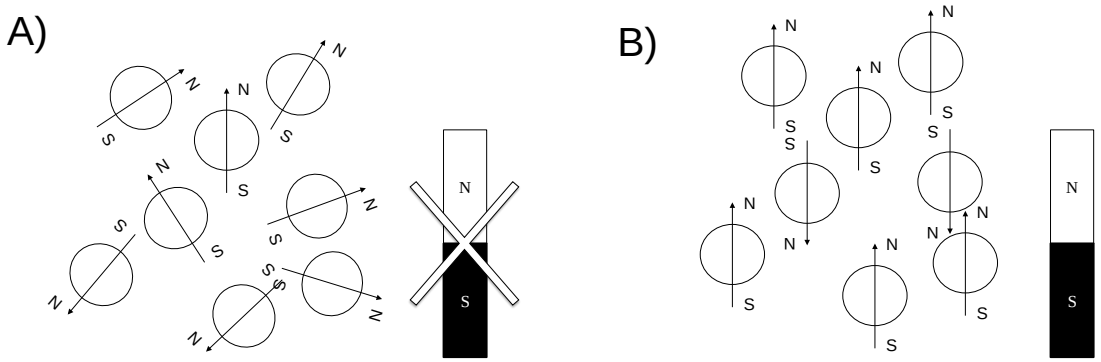

Fig. 2.9 Hydrogen's magnetic behavior A) without magnetic field and B) within a magnetic field

In this state of alignment with the magnetic field, hydrogen nuclei move around the magnetic field direction in a motion known as precession. The graphical representation of a precessing Hydrogen nucleus can be observed in figure 2.10 where the proton spin follows a path with specific frequency called the *precessional frequency*.

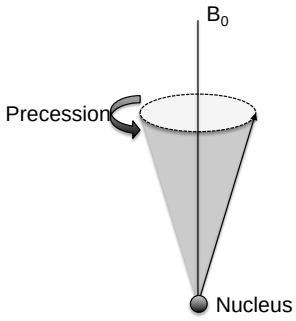

Fig. 2.10 Precession of the hydrogen nucleus

The precessional frequency is determined by the Larmor equation:

$$\omega_0 = B_0 \times \gamma \tag{2.8}$$

where B_0 is the magnetic field strength. γ is the gyro-magnetic ratio, which expresses the

relationship between the angular momentum and the magnetic moment of the nucleus. The gyro-magnetic ratio for hydrogen is $42.57 MHz/T$. The gyro-magnetic ratios of other nuclei differ with that of hydrogen, even at the same field. The Larmor frequency of hydrogen in a 3 Tesla magnet is 127.68 MHz.

When a nucleus is exposed to RF radiation with the same frequency as the Larmor frequency, it gains energy. Therefore, in this example a radio frequency (RF) of 127.68 MHz can resonate the hydrogen atoms. This RF pulse, depending on its duration and amplitude, can flip the angle of alignment between the nucleus and B_0, from the lower to higher energy level. During the return from the excited level (relaxation), the absorbed energy is released as an RF signal. This is transformed in to voltage through read out coils and this is the MR signal. The frequency is the same with the Larmor frequency.

During this relaxation period two factors influence the output signal. The relaxation times *T1* and *T2*. *T1* and *T2* vary across different tissues leading to contrast between different types of tissue. In *T1*, the energy released to the surrounding lattice causes nuclei to recover the longitudinal magnetization. *T1* relaxation times are on the order of 500 to 1500 ms for tissues other than water. *T2* decay is the result of decayed transverse magnetization. For tissues other than liquids *T2* decay time is less than 100 *ms* (Westbrook and Kaut, 1998).

2.3.2 Spatial localization and image acquisition

During an MR acquisition, gradient coils are used to provide linear magnetic field gradients in x, y, and z directions. These gradient magnetic fields are complementary to the B_0 magnetic field. Applying a gradient to the B_0 field results a change in the Larmor frequency as a function of position. The gradient coils are assigned for slice selection, frequency encoding and phase encoding. Figure 2.11 demonstrates the basic gradient echo sequence.

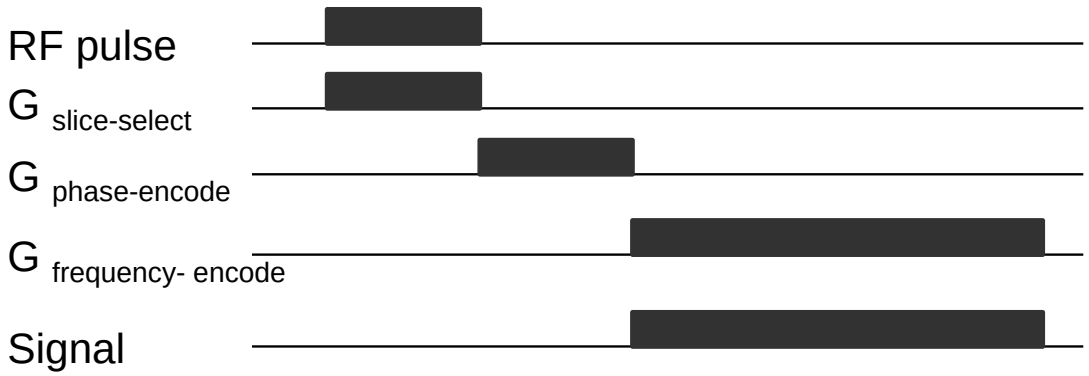

Fig. 2.11 Basic gradient-echo MR imaging sequence. The combination of slice selection, phase encoding and frequency encoding allow the creation of a 2D image in the selected slice

2.3.2.1 Slice selection

A slice selection gradient field is applied during the RF pulse. It is applied along a selected axis; most likely Z axis. A gradient applied during the RF excitation ensures the alteration of the ideal Larmor frequency in every other area, except the slice where $\Delta B_z = 0$.

2.3.2.2 Phase encoding

The phase encoding gradient field is applied after the RF excitation. The graduated magnetic field is applied along the remaining dimension, not covered by the slice selection and frequency encoding gradients. With the application of this gradient, the precessional frequency changes in linear fashion, along the applied gradient. When the gradient stops,the precessional frequencies returns the initial state, before the excitation, but variations in phase have been created during this application. The same slice is acquired multiple times, with the same frequency encoding and slice selection gradient. The variation comes to the phase encoding gradient which is varied with a different gradient strength each time. The total number of iterations corresponds to the total number of picture elements along this axis.

2.3.2.3 Frequency encoding

After the excitation of a specific slice and the application of phase encoding gradient, a frequency encoding gradient is applied along with the signal readout. The application of the gradient along this axis alternates the precessional frequency in linear fashion along the applied axis, creating a frequency shift.

2.3.3 Contrast agents

As for the other imaging modalities during an MR acquisition common practice is the use of contrast agents for enrichment of the information obtained from a region of interest. In MR, the contrast agent influences the T1 and T2 relaxation times of hydrogen. The most common contrast agent is Gadolinium, a metallic element with ferromagnetic properties (Lentschig et al., 1998). The effect of gadolinium in MR is the shortening of relaxation time T1 within tissue where it is taken up. For that reason, T1 weighted images of these tissues are recommended for maximum signal enhancement. Another group of contrast agents is the SPIO (Super-Paramagnetic Iron Oxide), used for carcinoma detection (Nakamura et al., 2000). Also other chemical elements are used as contrast agents such as Superparamagnetic iron platinum particle (SIPP) or Paramagnetic Manganese (Taylor et al., 2008, 2011). With wide variety of formulations it reduces the T2 values adjacent to it (Lee, 2006).

2.4 PET-MR

Instrumentation and methodology for combined PET and MR has progressed slowly and only very recently it has become possible for PET-MR to be used for clinical imaging of humans with emerging applications in cancer imaging. The brain insert and the whole body scanner can provide simultaneous acquisition and consequently new imaging methodologies can be developed. In addition to applications in humans, innovative methodologies, have

been developed for small animal imaging.

The initial research results for physical combination of PET detectors within an MR environment began in 1994 (Hammer et al., 1994). In this experiment, a pair of photodiodes were used to demonstrate the improvement in PET spatial resolution with and without the presence of a strong magnetic field. Cherry et al. (1996), for the purposes of the microPET (PET-only scanner) development, coupled an 8 by 8 crystal array to a 64 pixel position sensitive photomultiplier with use of optical fibres (Cherry et al., 1996). This concept was adapted to create an MR-compatible PET scanner(Garlick et al., 1997; Shao et al., 1997). These scanners were used for simultaneous imaging of perfused rat hearts inside 9.4 Tesla NMR. The concept of using optical fibres to transfer the light outside the magnetic field influence have also been revisited with the design of the microPET - MR (Lucas et al., 2006), PANDA II insert (Mackewn et al., 2005) and the APD based PET insert (Catana et al., 2006). The introduction of APD as a photodetector, led to the creation of the first human PET/MR insert for simultaneous brain imaging (Kolb et al., 2012) and finally, the creation of the biograph mMR, whole body PET-MR scanner (Delso et al., 2011). During that period, the SiPM technology was introduced for PET-MR applications with the HYPERimage small animal PET insert (Schulz et al., 2009) and the SiPM small animal PET insert by (Yoon et al., 2012).

During the last few years of development, a common design has been established for the integration of PET with MR. Figure 2.12 describes the main design adopted for simultaneous PET-MR scanners, where the PET scanner is enclosed inside the MR. The RF coil is placed within the PET scanner so it is closer to the subject for better signal recovery.

The current uses of a preclinical PET-MR include the evaluation of bimodal agents, visible with PET and MR (de Rosales, 2014) and dynamic acquisitions in cancer imaging for small animals (Judenhofer and Cherry, 2013). The use of clinical PET-MR systems, includes brain metabolism with use of the brain PET insert. Furthermore, cancer imaging

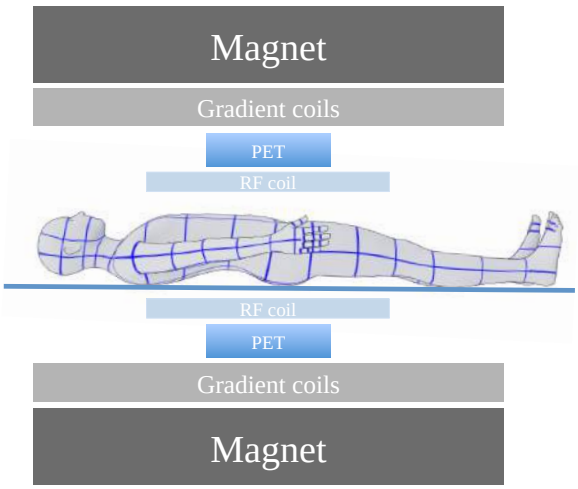

Fig. 2.12 Design concept of a simultaneous PET-MR scanner

utilizes the PET-MR to investigate a range of malignancies, such as pancreatic, lung, colorectal or ovarian cancer. An advantageous application of PET-MR is its use for paediatric studies because of the reduced radiation dose, compared to PET/CT (Herrmann et al., 2013).

A limiting factor for the PET-MR is that an accurate attenuation map is not available. Research points out the use either of Ultrashort Echo Time (UTE) sequences for bone imaging (Keereman et al., 2010) or use of Tissue atlas and template attenuation maps (Malone et al., 2011).

2.4.1 PET-MR data processing

PET-MR is an integrated system, and it has to perform in unity. This aspect brings many new challenges to data processing, among them, the need for accurate spatial alignment via registration, attenuation correction and temporal synchronization. These areas of investigation are explained in detail in the following paragraphs.

2.4.1.1 Spatial alignment

Accurate spatial alignment of images among different modalities is necessary for the extraction of complementary information. Whilst PET-MR images are acquired simultaneously in the same gantry, this does not ensure that the images are spatially aligned. Thus, a calibration procedure is required. The phantoms developed for PET/CT may not be compatible with the new system of PET-MR. This led to the re-engineering of the alignment phantom. A viable solution was proposed by Ng et al. (2010). His study proposed the use of small tubes filled with water and PET radiotracer. The system used for this evaluation was a PET insert for the Bruker Biospin 7T magnett, fitted with a Bruker B-GA12 gradient coil set. The PET insert consists of Lutetium Oxyorthosilicate (LSO) crystals and Position-sensitive Avalanche Photomultiplier Diode (PSAPD) detectors. During the experiment, the rods were filled with 50 μCi of ^{18}F-deoxyglucose (^{18}F-FDG). The rods were made of glass with external diameter 1.2 mm and internal 0.68 mm. Both ends of each tube were sealed. All PET acquisitions were reconstructed with a maximum *a posteriori* algorithm. The arrangement of the tubes is given in figure 2.13. After registration (see chapter 2.4.1.2), registration error for this phantom was between 0.12 *mm* in the centre of the Field of View to 0.28 *mm* at 12 *mm* from the centre of the field of view (Ng et al., 2010).

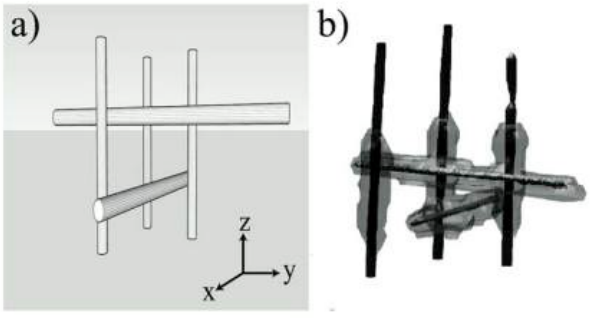

Fig. 2.13 PET/MR FOV alignment phantom, a) graphical representation of the 5 rods of the phantom, b) PET/MR phantom image overlay (Ng et al., 2010).

2.4.1.2 Image Registration

The means for spatial alignment in PET-MR is given by image registration. Image registration is a technique to combine spatially two images of the same object and can be used to find the transformations used for motion correction. The registration algorithm aligns these images by warping the one to the other. The registration can be performed with two images of the same modality (intramodality registration) or between different modalities (intermodality registration) The components to achieve registration are the following:

1. *Similarity*: The calculation of the similarity between the image being transformed and the target.

2. *Transformation*: This controls whether the deformation is rigid or non-rigid and to what degree.

3. *Optimization*: Registration is achieved by finding the transformation that maximizes the similarity measurements.

In the Cartesian coordinate system (x,y,z), rigid transformation allows 3D translation and 3D rotation, which in total is 6 degrees of freedom. This registration algorithm is used for simple motion models.

Affine transformation allows twelve degrees of freedom with 3 scale and 3 shear components added to the previous stage.

Moreover, more complex, non-rigid transformations are usually required. Many algorithms have been developed for this. One method is to base on transformation of control points and afterwards, interpolated motion fields are applied to the entire image (Crum et al., 2007).

Another method is to combine local and global transformations like rigid and/or affine(Little 1996). In the hierarchical multiple local registration methods, the image is subdivided into

rectangular blocks and within each block a transformation takes place. The hierarchical splitting occurs while dividing the single blocks into smaller equally spaced blocks.

The optimisation of these algorithms depends on the adaptivity of the box selection. In the method of Buerger et al. (2011) studies, a hierarchical adaptive local affine registration algorithm is created, which, as it progresses with the registration, subdivides the images to areas with similar motion. With this technique, areas with small motion amplitude can be considered as rigid, and large deformation can be processed as a group (Buerger et al., 2011).

2.4.1.3 Attenuation correction

The artefacts and loss of accuracy due to attenuation can be restored partially with attenuation correction. The attenuation correction takes under account the attenuation coefficient of the subject. Until this point, CT could provide the equivalent attenuation coefficient factors for the scanned subject of study. The use of MR imaging may have improved the imaging of soft tissue but the transmission methodology of the CT was capable to provide the attenuation information, something that MR cannot provide.

Different approaches have been executed for the generation of attenuation maps from MR data. An approach is the classification of tissue to different known categories. For example, one approach uses a 2-point Dixon sequence (Siemens inc.) in order to discriminate fat from water. The produced images generate a fussed attenuation map, using known attenuation coefficient values previusly derived CT. This methodology can image soft tissue but not bones, which aren not visible on MR images (Martinez-Möller et al., 2009). The lack of bones imaging can be addressed by the use of Ultrashort Echo Time (UTE) acquisitions.With this scanning methodology, bone structures are visible, where the T2* relaxation time is very short (0.05 - 2 ms). Finally, another approach is to use an atlas of the region of interest. This atlas derived for example from a library of CT images is registered to fit the

acquired MR image and the corresponding attenuation matrix is used for the correction.

2.4.1.4 Temporal synchronization

PET-MR is the first truly simultaneous imaging. This brings the challenge of exactly synchronizing the PET and MR acquisitions. In the early stages of PET-MR imaging, the synchronization is performed with coordinated manual initiation of the two acquisitions. Catana et al. (2011), in his studies describes the methodology to synchronize the brainPET prototype scanner with the MR. In this study, an output trigger pulse was provided to the PET module by the MR. This trigger pulse was repeated every 0.2 ms were an MR motion estimate was obtained (Catana et al., 2011).

2.5 Motion in PET-MR

Subject motion can affect both PET and MR image quality for human and preclinical studies. Motion can introduce artefacts and reduce the accuracy of quantification. It can also reduce the possibility of identifying small regions of uptake such as small tumours. One of the possible advantages of simultaneous PET-MR acquisition is the use of simultaneous MR images to correct PET images for these effects of motion. There are many different aspects to the problem of motion correction which are described below.

2.5.1 Motion in humans

In the human body, muscles are responsible for the motion in each part of it. Musculoskeletal, smooth and cardiac muscles are the main factors for human mobility. This motion is defined as systematic (motion of vital organs of the subject i.e. heart, lungs, diaphragm) or spontaneous (musculoskeletal, spontaneous, non-repetitive motion i.e. head motion, peristalsis or random body movements).

During torso scanning, the heart and the respiratory system normally consist the most significant systematic motion sources in humans and rodents. The heart follows two different patterns of motion. The first is defined by its own function, where the contacting ventricles pump the contained blood through the circulatory system. The other motion is defined by respiration. The motion of the diaphragm creates a deformation and dislocation of the internal formation of the surrounding organs. Liver, stomach, kidneys and heart are all organs affected by respiratory motion. The basic principles of respiratory motion depend on the mode of respiration pattern. Motion of the human diaphragm and the effects of this motion on the surrounding organs have been studied extensively for two different patterns of respiration by Langen and Jones (2001). These patterns are normal and deep breathing ((Langen and Jones, 2001). By this study the average motion of the diaphragm ranges from 9.1 $\pm$ 2.4 mm to 17 $\pm$ 3 mm for normal breathing and from 43 $\pm$ 10 mm to 103 $\pm$ 22 mm for deep breathing. Similarly, the motion of the liver varies from 8 $\pm$ 2 mm to 25 mm for normal breathing and by 37 $\pm$ 8 mm to 55 mm for deep breathing. The amplitude of motion varies a lot between individual patients. In addition to the displacement of each structure during motion, the volume and shape of the organs may change. For example, Liu et al. (2007) characterized tumours as solid, semi-solid and diffused (Liu et al., 2007). Furthermore, Rietzel et al. (2005) provides quantitative features of the tumour deformation, for liver and lung tumours. For a single study, inside liver, the volume deformation is about 3% and inside lung, the volume deformation is about 30.4% (Rietzel et al., 2005). Studies about the breathing pattern revealed a variation of motion path between inspiration and expiration. More than two forces are applied to each position in the thoracic cavity, during breathing. These forces match in frequency but vary in phase. This leads to variations of motion and an ellipsoidal pattern is created for each cycle. This phenomenon is called intra-cycle variability or hysteresis.

2.5.2 Motion of Small animals

Human and rodent anatomy share features behaving in a similar way with respect to motion. In particular, diaphragm and cardiac motion function similarly; though in different spatial and time scales. Artefacts occur to the obtained images because of the systematic motion of the animal's organs. An additional factor is the increase of motion frequency. According to Segars et al. (2004), during regular mouse breathing, diaphragm motion is about 1 mm and the rib cage expansion is at 0.7 mm. From the same study, data is presented from MR mouse scans, placing the maximum diaphragm motion at 1.2 mm (Segars et al., 2004). As a graphical representation, Figure 2.14.a demonstrates the respiratory pattern, as described by Segars et al. (2004). Figure 2.14.a corresponds to the respiratory pattern of a rat under isoflurane anaesthesia, as presented by Bartling et al. (2007). The explanation for the respiratory pattern difference is an effect of Isoflurane/Oxygen anaesthesia, which makes rodents gasp (Bartling et al., 2007).

In literature, there are PET studies where the rodent is awake (Kyme et al., 2014). Nevertheless, the standard procedure is to anesthetize the rodent for minimization of motion artefacts. Studies have provided information about the behaviour of rodents under anaesthesia. Figure 2.14 presents the respiration of a human (a) and of a rodent under anaesthesia.

The need of anaesthesia brings an alteration between the respiratory pattern of humans and animals. If that part of respiratory motion is excluded by the data acquisition with gating, the total signal loss will be less than 10%.

2.5.3 Motion effects in MR and PET imaging.

Motion during PET studies can result in artefacts in the final image. This paragraph is concentrated on data from human applications. Figure 2.15 is an example, where the end inspiration and end expiration positions of a tumour from a 4D CT match with the extremities of the stretched volume, as PET obtains it.

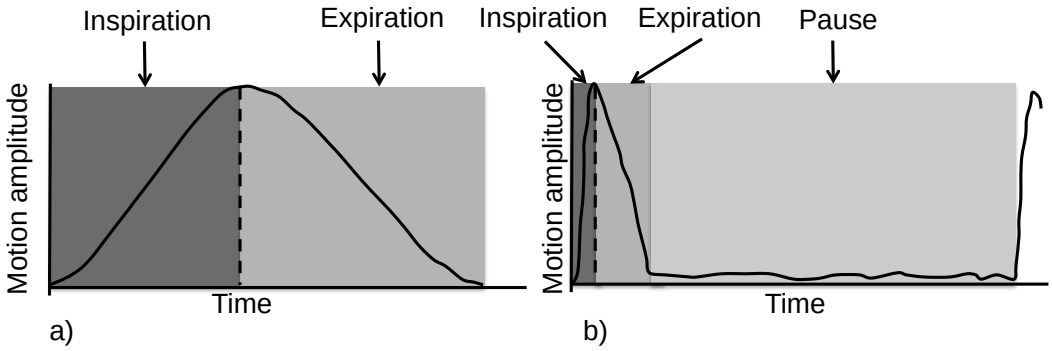

Fig. 2.14 Respiratory pattern, a) of human and b) a rat under Isoflurane anaesthesia

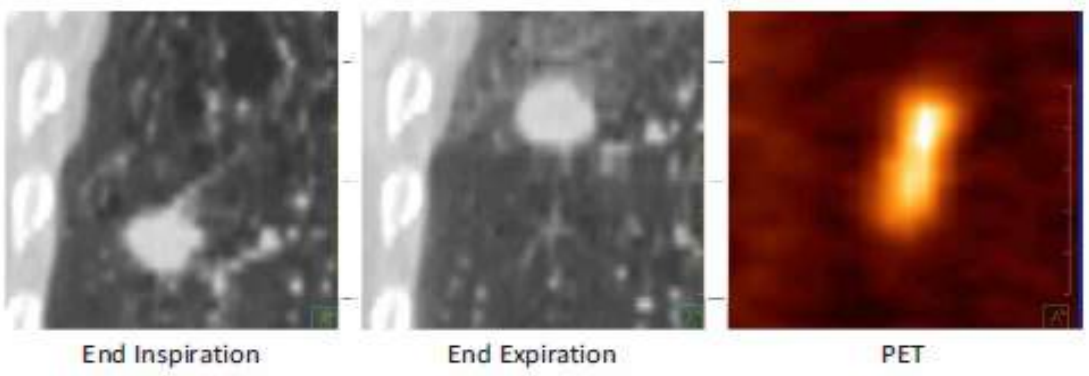

Fig. 2.15 End inspiration phase of 4D-CT, end-expiration phase of 4D-CT, and PET images of moving lung tumour in human. All images are coronal slices. Note the blurred appearance of the moving tumour in the PET image, which is acquired over several breathing cycles (Riegel et al., 2010)

In PET imaging, data is typically acquired for several minutes per bed position, which leads to time averaging for many breathing cycles. The respiratory motion will blur the image and degrade contrast leading to overestimated volumes and poor quantification. Figure 2.16 demonstrates such artefacts for an oscillating point source where motion simulates that of breathing. The result of this motion is the spread of counts, the volume increases artificially and eventually, the SUV is underestimated. Also, the attenuation correction is possibly wrong, due to the fact that is a product of a static image instead of a dynamic moving PET image (Dawood et al., 2006).

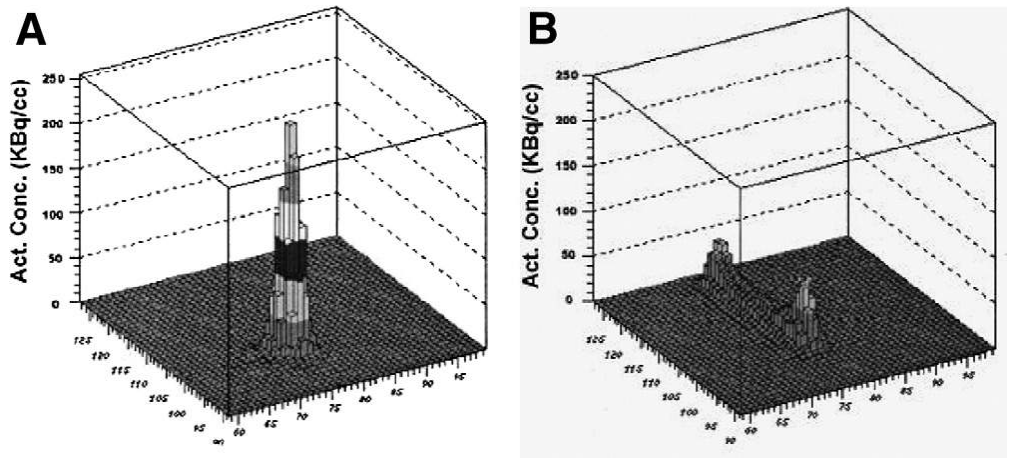

Fig. 2.16 (A) Apparent activity concentration for a stationary point source showing the expected Gaussian distribution. (B) The apparent activity concentration is "stretched" when the point source is oscillating, resulting in overestimation of the object volume and underestimation of SUV (Nehmeh and Erdi, 2008).

For MR imaging, motion brings artefacts to the image. As White et al. (2010). state, in short sequences such as dynamic 2D or echo planar imaging, the in between scans motion can introduce significant variance to the voxel time courses and disrupt the spin excitation history of the acquisition (White et al., 2010). The motion causes artefacts on scans, with the nature of ‘ghost’ images along the phase-encoding direction. The number and the sensitivity of ghost images depends on the regularity of the motion, ranging from just a few high-intensity ghosts of the chest wall, to a generalized low-intensity blurring due to the non-

periodic motion of the bowels. In figure 2.17 a simple example of motion artefacts along the phase-encoding direction is presented.

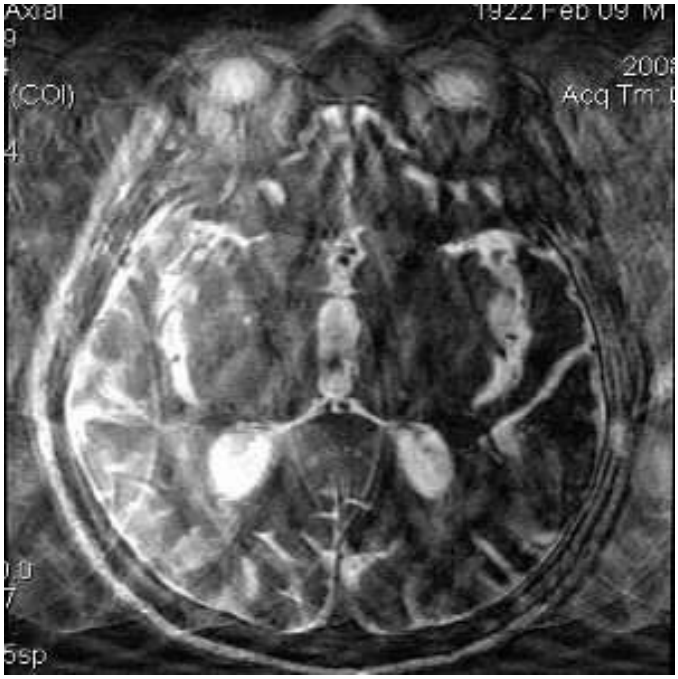

Fig. 2.17 Gross motion artefacts due to patient moving continuously throughout a scan

2.5.4 PET motion capture

Due to the artefacts described previously, it is necessary to correct for the motion and provide an artefact free image. The first objective is to track the motion.

External devices have been used in the past for PET/CT studies, where the patient had to be connected with one or more of the following systems:

i. Pressure sensor, capable to be connected with an elastic belt. The tension created by the respiratory motion is captured by the pressure sensor and translated into displacement. Pressure sensors have been used in radiotherapy (Dietrich et al., 2006; Li et al., 2006a), 4D-CT (Kubo and Hill, 1996) and PET (Martínez-Möller et al., 2007).

ii. Also, a spirometer can provide the necessary information for motion estimation. Instead of motion amplitude variation, spirometer provides volume variation. Also, the data are stored in a computer, along with the PET acquisition for motion estimation uses. It has been also used in radiotherapy (Kubo and Hill, 1996; Zhang et al., 2003), CT (Kalender et al., 1990) and PET imaging(Martínez-Möller et al., 2007).

iii. As an alternative method of tidal volume measurement, the temperature variation from the air flow indicates the respiration cycle of the patient. This is a method also used in radiotherapy (Kubo and Hill, 1996) and PET (Martínez-Möller et al., 2007).

iv. Visual capture of the respiratory motion can be performed with Real-time Position Management system (RPM). The RPM introduces a camera, which tracks the motion of a marker placed upon the patient's thorax. This method has been used for radiotherapy, 4D-CT, respiratory-gated CT and respiratory-gated PET (Nehmeh and Erdi, 2008). Markers have been used for small animal tracking during PET. Kyme et al. (2008), in his study describes the marker design and camera setup for motion tracking and use of this information for motion correction.

v. Use of markers in combination with video tracking is not the only way. Kyme et al. (2014) developed a method to track motion information by physical landmarks upon rat's head. For human use, Alnowami et al. (2010) proposed a method of respiration tracking, with video capture of the torso and use of a B-spline model for parametrization of it.

vi. MR is also capable of tracking and measuring respiratory motion (Shechter et al., 2004). By use of navigator echoes, it tracks the displacement of the diaphragm. Typically, the navigation echo is extracted by the right hemidiaphragm, at the lung-liver interface. While the patient breathes freely, navigator echoes track the craniocaudial motion of the diaphragm over time, with no interference with the simultaneously obtained images.

The techniques above provide a one dimensional signal, representing the respiratory phase. The need is to generate a 3D volume, which will be used for the extraction of motion fields of the deformation. 4D CT is a method, where 1-D signal can be used to rebin the acquired 4-D data into the corresponding gates. The reconstructed gates create a cinematic representation of the respiratory motion in multiple positions. These images can be used afterwards for motion correction of any complementary acquisitions (Nehmeh et al., 2004). MR imaging can follow the methodologies developed for CT. To be more specific, Cao et al. (2003) proposes a method where the MR acquires fast 2D axial images in random respiratory positions which are sorted retrospectively to the corresponding respiratory phases, depending on the respiration amplitude (Cao et al., 2003). The sequence selection criteria are the short acquisition time and optimization of image quality.

The effects of motion in PET images can be addressed with motion correction given by a sequential scanner. Until now, the only available method was the use of CT and especially 4D-CT. 4D-CT is based on data acquisition over several respiratory cycles which is then sorted into different groups (gates) according to the respiratory phase. A subsequent PET acquisition is then sorted to the same number of gates. A disadvantage of this method is the poor spatial alignment because of the registration errors. Temporal miss-alignment is an effect of respiratory motion, where a typical scan for the CT is 15 s (i.e. for few breath cycles) and for PET is several minutes per bed position. Another issue related with the image quality is the respiratory pattern. Variations can be observed in period or amplitude of each separate breath. Therefore, the patients are instructed to have free tidal breathing during the PET scan with the same pattern as reasonably achievable .

Recent investigations presented the possibility of PET motion correction, using the same dataset. Schleyer et al. (2014) in his study proposed a method, where the PET data are handled in the frequency domain to locate the regions within raw PET data that are subject to respiratory motion and to generate the respiratory curve.

Tsoumpas et al. (2010) proposed a method for motion data acquisition and correction by use of simultaneous PET-MR system. The benefits of this method are the lack of additional radiation to the patient and the fact that the motion information can be obtained simultaneously with the PET data, giving an advantage against the sequential PET/CT system (or PET/MR). Also the motion fields derived by the MR can be used to correct the PET data (Tsoumpas et al., 2010).

2.5.5 Motion estimation

The capture of motion is the first step. The second step is the estimation of the internal motion and use of this information for correction of PET data. In a study by Abd Rahni et al. (2011), the motion of organs, estimated with a low-dose 4D-CT and combined with the motion information by a markers grid, is used to create a motion model. The application of this model to the markers grid motion leads to organ motion estimation.

In MR, a method proposed by Buerger et al. (2011) proposed a method, where a free-breathing dynamic scan, combined with the local affine registration algorithm, can be used for motion estimation during the acquisition. Given the nature of the acquisition, each MR dynamic frame has a finite temporal resolution. The method to estimate motion alterations with shorter temporal resolution than the one proved by a scan is by motion modelling. The first step is to acquire a dataset of the respiratory cycle with low temporal resolution but high spatial. This dataset is used to train the motion model algorithm. Afterwards, pencil beam navigators, single 2D slices or multiple 2D slices are acquired with high temporal resolution. The image features are correlated with the motion model and the 3D estimate is produced. Use of motion models can improve the temporal resolution of MR and consequently PET frames (King et al., 2012; Smith et al., 2013).

2.5.6 PET gating

Gating is a common method to handle respiratory motion. In order to gate the data, a respiratory cycle is divided into a number of gates. These gates share a common characteristic, and are confined to a smaller threshold, compared to the entirety of data. There are two main types of gating. *Phase* and *amplitude* gating.

In phase gating, the respiratory cycle is divided in equal time intervals and coincidences that correspond with the time interval are rebinned to the corresponding gate. This method ensures the equal counts distribution among the gates. In studies though the phase correlation of motion changes over time thus may not represent the motion amplitude correctly for all the respiratory cycles (Ozhasoglu and Murphy, 2002).

Amplitude gating splits the respiratory cycle based on the motion amplitude, while breathing. Motion amplitude may vary for each respiratory cycle. Dawood et al. (2009) demonstrated that using amplitude gating could result in noise reduction, but under regular breathing both amplitude and phase gating performed similarly.

2.5.7 PET motion correction

After acquiring motion information, synchronizing and spatially aligning PET and MR data, and data rebinning into gates, motion correction can be applied to PET data. Motion information is estimated either from CT or MR images. Algorithms used for motion estimation measure the deformation between gates and motion fields are estimated. The two main approaches to applying known motion information to correct the PET data are *Reconstruct Transform Average* (RTA) and *Motion Compensated Image Reconstruction* (MCIR).

In RTA, an image for each gate is reconstructed with a standard reconstruction algorithm and after that, the relevant transformation is applied to each gate. Various registration algorithms can be used to obtain the transformations with respect to respiratory motion correction, Dawood et al. (2006) used an optical flow method calculated and rebinned the

PET data to the corresponding gates and performed motion correction of the reconstructed images. During RTA, the non-linearity of the reconstruction is not taken under account, because is a post-reconstruction process. Even though, RTA remains a practical approach in PET motion correction because there is no need to modify the standard reconstruction algorithms (Dawood et al., 2006; Picard and Thompson, 1997).

On the other hand, In MCIR, the image transformations are incorporated directly into the reconstruction algorithm and the data from all gates are processed simultaneously to create a single motion corrected image(Lamare et al., 2007; Li et al., 2006b; Qiao et al., 2006).

Chapter 3

PolyVinyl alcohol phantom for simultaneous PET-MR applications

3.1 Introduction

In the previous chapter, we introduced the necessity of motion correction in PET and the currently available tools. The development of a new platform for PET motion correction investigations has to be established. The motivation behind this is to increase motion realism and complexity to resemble the sort of respiratory motion seen for the liver for example. Therefore, there is a need for the development of an MR compatible PET-MR phantom with non-rigid motion and programmable motion patterns. This phantom, has to be compatible with all the modalities used, predictable and reproducible and to cover as many realistic cases as possible.

In the case of a PET-MR scanner, as already discussed, the platform for the development and evaluation of motion correction has to contribute equally to both of the systems. Also, new parameters of realism have to be introduced into motion correction evaluation platforms. A robust and reliable platform of evaluation in any system is a phantom. A controlled environment, determined by the user for performance evaluation. This chapter

describes the utilization of PolyVinyl Alcohol (PVA) cryogel as a PET-MR phantom for motion correction (Soultanidis et al., 2013a).

3.2 PVA cryogel for construction of deformable PET- and MR-visible phantoms

Recent phantom investigations indicate that it is possible to measure motion through sequential PET/CT (Bai and Brady, 2011; Gigengack et al., 2012; Wollenweber et al., 2012; Yang et al., 2012) or simultaneous PET-MR systems (Chun et al., 2012; Tsoumpas et al., 2010). For example, Tsoumpas et al. (2010) used a locally rigid moving phantom visible in both PET and MR constructed from Perspex, and Guerin et al. (2011) used a rigid PET source inside a deformable medium (Guerin et al., 2011). Finally, a human torso phantom was presented by Fieseler et al. (2013). There are indications from literature that the motion of a lesion inside the human body is not limited to rigid-body spatial displacement but also can include general non-rigid deformations. The deformation of tumors has been investigated by Kyriakou and McKenzie (2012), who showed evidence of deformation during respiratory motion inside the lungs (Kyriakou and McKenzie, 2012). This physical property of the tumors and the need for even higher accuracy in designing even more realistic phantoms prompted the design of a phantom capable of containing a radioactive source that can deform along with the medium when motion occurs. Until now, the vast majority of motion experiments use rigid phantoms, but there is some progress towards deformable phantoms. To show what makes a deformable phantom more realistic, we examine the behaviour of an entire organ under respiratory motion. In this case, the liver is the organ under examination because of its location. It is located beneath lung and it follows the motion of it. The motion of it is not either rigid or linear. Fig 3.1 provides a graphical representation of liver surface deformation according to location (Nguyen et al., 2008).

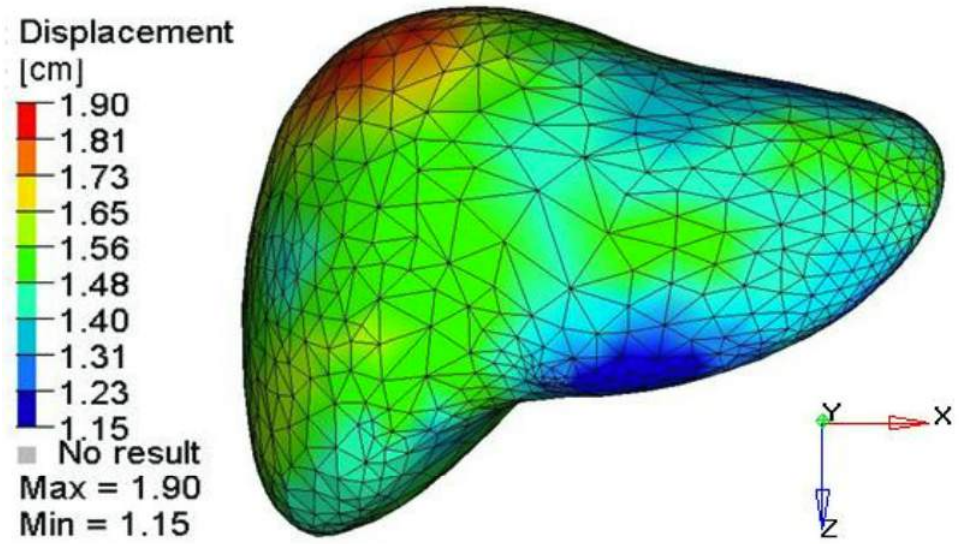

Fig. 3.1 A colour scale representation of deformation map of a liver (Nguyen et al. (2008), © IEEE 2008)

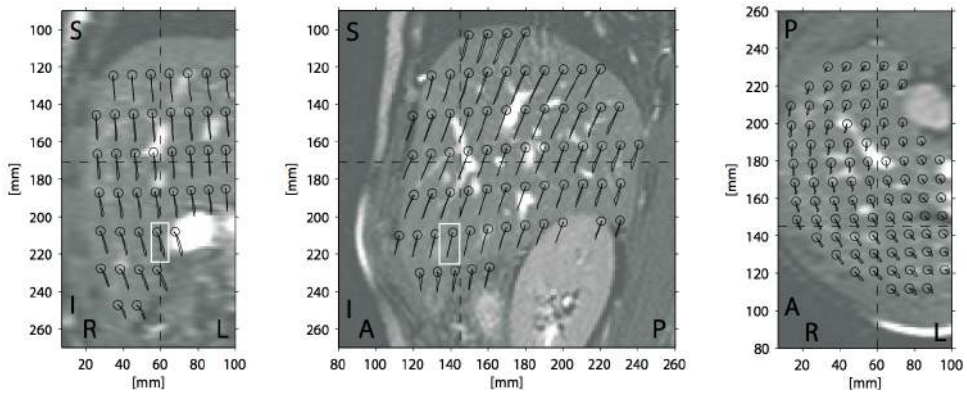

Fig. 3.2 Trajectories of a motion field grid inside the liver caused by respiratory motion (Von Siebenthal, 2008).

Furthermore, the direction of the motion is not constant either. In Figure 3.2, it is understood that the motion fields do not follow the same direction within a plane (Von Siebenthal, 2008). This is evidence that motion production and simulation of solid organs has to be performed with use of deformable phantoms.

More specifically, studies performed by Tsoumpas et al. (2013) describe the maximum

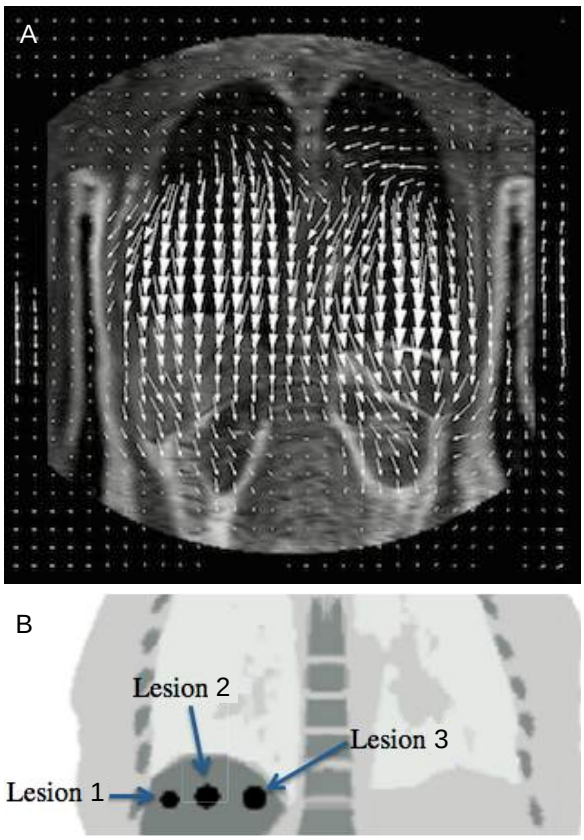

Fig. 3.3 Respiratory motion of human torso, where A) shows motion fields derived from a dynamic MR sequence and B) Shows the three liver lesions to which these motions are applied (Tsoumpas et al., 2013).

motion amplitude of multiple lesions of a computational human torso phantom. The motion fields of this torso phantom are derived by real MR motion acquisitions. Figure 3.3 is a gives a visual representation of these motion fields and the lesions we are going to focus upon. Table 3.1 provides information about the maximum displacement of each lesion. Inside the same organ it is observed that there is difference of displacement for the closely spaced, maximum to be 6.5 mm. Through these studies, it is clear that an organ does not follow a rigid displacement during a respiratory cycle but it is deformed non-rigidly.

Standard PET and MR phantoms usually contain uniform radioactivity distributions, i.e. liquid filled volumes, that can undergo only very simple and unrealistic deformations (Madsen and Fullerton, 1982; Mathur-De Vre et al., 1985; Muehllehner et al., 1981). Such

Table 3.1 Maximum lesion displacements

	Inferior-superior (*mm*)	Posterior-anterior (*mm*)	Left-right (*mm*)
1^{st} lesion	11.9	3.5	8.4
2^{nd} lesion	15.4	1.8	7.6
3^{rd} lesion	16.9	2.7	1.9

uniform liquid filled volumes also result in very unrealistic MR images leading to untypical behavior of image registration algorithms and incorrect estimates of motion fields.

There is great interest in using mass-preservation as a constraint in image registration algorithms, particularly when used in motion correction schemes (Gigengack et al., 2012). Most currently used non-rigid image registration algorithms however, do not have this feature, so even though most tissues (with the notable exception of the lung) are approximately non-compressible, this is usually not accounted for in the registration process resulting in physically unrealistic motion fields.

There is therefore a need for phantoms that can simulate realistic mass-preserving non-rigid deformations and that are both PET and MR visible. Whilst the simple configuration described here does not represent of any particular organ, the technique allows the production of (independent) PET and MR visible distributions that undergo complex non-rigid deformations. This will be of value in the assessment and further development of accurate corrections for non-rigid motion, which is an area that is still at a very early stage of development.

MR phantoms are usually water based. One of the materials from which MR phantoms are constructed is the Poly-Vinyl alcohol (PVA) cryogel. A cryogel is a material that consists of water and a polymer, in this case, polyvinyl alcohol. Freezing and thawing is the method used to cross-link the hydroxyl groups on PVA molecules by hydrogen bonding (Chu and Rutt, 1997). The product of this procedure is an elastic material with a high concentration of water. Cryogel has been characterized as an 'ideal' MR phantom for elastography, where

for a 10% by weight solution, T1 and T2 relaxation times are 718 – 1034 *ms* and 108 – 175 *ms*, respectively (Surry et al., 2004).

PVA cryogel can be generated by a procedure described in the literature (Surry et al., 2004). This procedure guarantees excellent stability and homogeneity of the material. The first step is to mix PVA powder with water. An autoclave is used to heat the PVA at 121 °C for 30 *min*. The cooled solution is then poured into a mould and frozen at –20 °C for 12 *hours*. Then, the freezer is unplugged and the material is allowed to thaw naturally over 8 to 9 *hours* after which time it is stored in de-ionized water.

The procedure above results in a material with elastic properties which can be used for the creation of a phantom capable of volume deformation. This study aims to investigate different aspects of adapting cryogel for PET-MR purposes by creating a structured phantom that is both PET- and MR-visible introducing radioactivity and MR contrast into the cryogel. The impact of the various modifications made to the standard production procedure is investigated below.

3.3 Materials and methods

3.3.1 Preparation of cryogel phantom

3.3.1.1 Phantom structure

The elasticity of cryogel gives the opportunity to fabricate a phantom that can be repeatedly deformed by an applied force. The phantom also has structural complexity which makes its visualization more similar to the structure of human tissue. The design used for this study consists of an 'active' cylinder contained within a 'cold' cylinder where the internal cylinder contains PVA, radioactivity and gadolinium solution, as shown in Figure 3.4. The diameter of the phantom is similar to the diameter of a rat (4 *cm* in approximation).

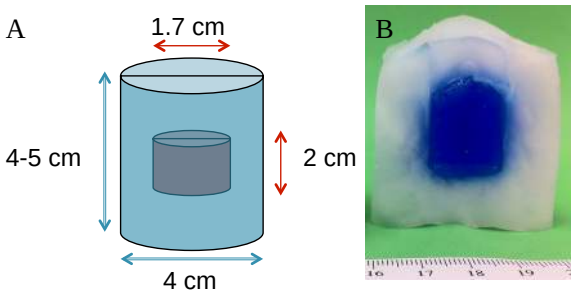

Fig. 3.4 Cryogel phantom with dimensions dedicated for small animal imaging systems; (A) and a cross-section of a phantom (B), where the external part is 10% p.w. PVA and the internal, coloured part contains also 2.25 *MBq/ml* of ^{18}F-FDG and 50 $\mu l/ml$ of Gadolinium solution. (Soultanidis et al. (2013a), © IEEE 2013)

3.3.1.2 Determination of optimum PVA concentration

A range of PVA concentrations are referred to in the literature, from 10% to 20% by weight (Chu and Rutt, 1997; Fromageau et al., 2007; Surry et al., 2004). We examined three different concentrations: 5%, 10% and 15% by weight of PVA in water. The most appropriate of these was used in the subsequent procedures described below. The success of the phantom will be evaluated using two criteria; the preservation of its shape, without additional load and the motor unit's efficiency to compress it without extreme stress.

3.3.1.3 Introduction of contrast agents into the phantom

The radioactive solution and contrast agents could be introduced in the phantom using different approaches. The first method investigated was the soaking of the phantom in a solution containing the radiotracer or gadolinium until it is absorbed. An indication of diffusion was obtained from published literature. The diffusion of Fe^{3+} was measured in a 20% per weight PVA cryogel and it was found to be 0.14 $mm^2\ h^{-1}$ (Chu et al., 2000). Therefore, the approach was rejected because the speed of diffusion is very slow. Nevertheless, an experiment has been performed in order to determine the diffusion rate. A cylinder of PVA cryogel with diameter of 14 mm was created. The goal is to determine the progression of

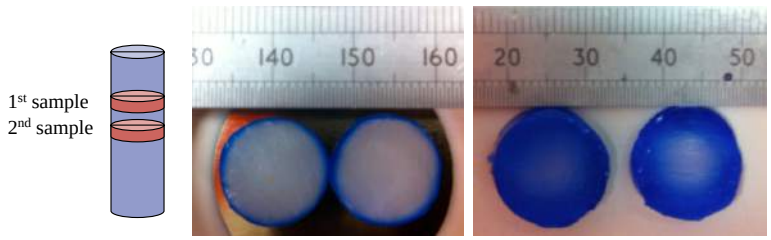

Fig. 3.5 10% PVA cryogel after 2 and 20 hours of immersion in 5% ink concentration solution.

the ink into the cryogel against time. The time points determined to be 2 hours after the immersion and 20 hours after the immersion. After this time period, slices from the centre of each cylinder where sliced and observed. Figure 3.5 gives an optical evaluation of the color progress after 2 and 20 hours. Clearly, 2 hours after the immersion, is about 1 mm.

Another approach is to inject the phantom with liquid contrast agents' solution or a second PVA solution containing radioactivity and / or MR contrast agents. However, the solution leaks when the phantom is compressed. The only viable method to create a radioactive phantom within reasonable time period is to mix the PVA solution prior to the freeze-thaw process. During this method, due to the high viscosity of PVA, care must be taken to ensure the solution is uniformly mixed to create a homogeneous tracer distribution.

3.3.1.4 Modifications to freeze-thaw production process

The standard cryogel production procedure has been described above. The total preparation time is about 20 to 21 *hours*. As the half-life of Fluoride-18 is approximately 2 *hours*, the standard preparation procedure is impractical. The solution is to decrease the freeze-thaw time. The first approach is to freeze the PVA cryogel with liquid nitrogen. Nitrogen boils at -196 ^{o} C. The use of this compound could ensure fast freezing process. The first experiments were performed without presence of radioactivity for structural integrity check. A 10% concentration PVA container was immersed into liquid nitrogen for 1 min. The freezing

process was successful with no obvious problems. During the thaw process though, the phantom had shattered structure with cracks everywhere, destroying the phantom.

An alternative solution is to decrease the time of the freeze-thaw process to 6 *hours* with use of freezers. The initial results of a freezer use is that the phantom does not have structural integrity issues. The initial structure of the phantom is created by freezing a first layer of the PVA that is used as a base (or external compartment) for a second layer of PVA (the internal compartment). This enables a partition to be created within the phantom. The compartmentalization of the phantom, as shown in Figure 3.4, enables the phantom to be realized in two freezing stages and a single thaw time period. In the first stage, the PVA solution is introduced into a plastic mould and the external compartment is frozen for 12 *hours* at –20 °C. After that period, the PVA solution with the radioactive molecules is introduced and the whole phantom is frozen for 3 *hours* at –80 °C. Finally, the phantom is removed from the freezer and thawed within 3 *hours*. The thaw process is natural and not accelerated by an external factor.

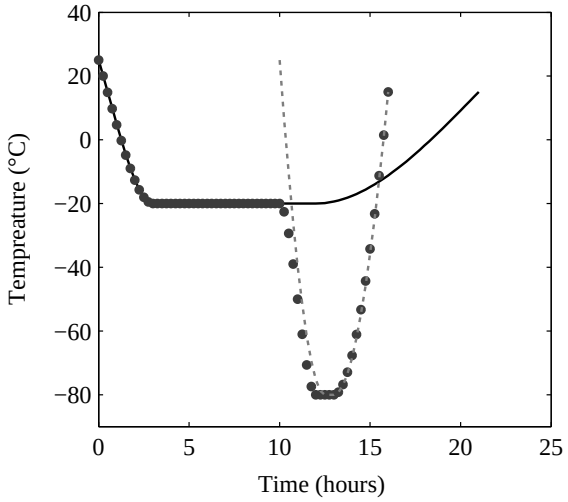

Fig. 3.6 Temperature progression for different freeze-thaw methods where; *method 1* is with solid line; *method 2* with • ; and *method 3* with dotted line. (Soultanidis et al. (2013a), © IEEE 2013)

3.3.2 Young's modulus measurements

An alteration to the procedure is likely to affect the elasticity of the cryogel which can be characterized in terms of its Young's Modulus. Duboeuf et al. (2009) proposed a simple mechanism, along with the methodology to measure Young's modulus of a PVA cryogel phantom (Duboeuf et al., 2009). The first sample was made according to the standard production procedure, hereafter named as *method 1*. The second sample represents the external compartment-freezing pattern, named as *method 2*, with 12 *hours* of freezing at –20 °C, 3 *hours* freezing at –80 °C and 3 *hours* of thaw. The third sample represents the internal compartment freezing pattern, named as *method 3*, where it freezes at –80 °C for 3 *hours* followed by 3 *hours* of thaw. A graphical representation of the freeze-thaw process is given in Figure 3.6. Two sample phantoms were created for each procedure. These samples have the same dimensions and cylindrical shape. Stress over strain was measured and the Young's modulus was calculated with the Eq. 3.1.

$$E = \frac{\sigma}{\varepsilon} = \frac{F/A_0}{\Delta L/L_0} \tag{3.1}$$

where F is the force applied to the phantom, A_0 is the initial area where the force is applied, L_0 is the initial height of the phantom and ΔL is the variation of length. Eq. 3.2 gives regularization of the area A, in order to eliminate the "barrel" effect. The barrel effect is the expansion of the central part of the PVA while the top and bottom diameter remains small (Duboeuf et al., 2009).

$$A = A_0 \frac{L_i}{L_i - \Delta L_i} \tag{3.2}$$

Where L_i is the height after compression and ΔL_i is the variation of height. The same set of measurements have been applied to each phantom for 4 times in order to have an estimate of the standard deviation upon Young's modulus.

3.3.3 Diffusion of the radiotracer

The phantom developed in this study has no physical boundary between the two cylindrical volumes. This fact, combined with the large amount of water may lead to diffusion of radioactive and gadolinium molecules through the phantom. Hence the labelled areas of the phantom might change over time due to diffusion. For this investigation, phantoms have been created, following the methodology presented above. The radiotracer used was ^{18}F-FDG, diluted inside a 10% per weight PVA cryogel phantom. The concentration of ^{18}F-FDG inside the phantom was 2.5 *MBq/ml* at the beginning of the experiment. A dynamic PET scan was performed with the NanoPET/CT™ preclinical PET scanner (Bioscan Inc., Mediso Ltd.), where 12 acquisitions of 10 *min* were obtained every 15 *min* period (Szanda et al., 2011). The alignment of acquisitions was ensured by not moving the phantom between every 10 *min* acquisition. The reconstruction used for these data was a Single Slice Re-Binning (SSRB) OSEM algorithm with 8 iterations and 6 subsets per iteration. This reconstruction algorithm does not perform any post filtering. The data were corrected for physical decay of ^{18}F and attenuation correction. Scatter correction was not applied to the data. The progression of diffusion can be captured as the radiotracer diffuses into previously unoccupied or unevenly distributed areas. Samples with same volume are examined for changes cause by diffusion.

3.3.4 Relaxation values of PVA cryogel

The MR properties of the phantom were determined. In this experiment, a 10% PVA cryogel phantom was used. The phantom was divided into two compartments, with the external compartment containing 10% PVA and 90% water. The internal compartment has an additional 50 $\mu l/ml$ gadolinium solution (Gadopentetic acid). The experiment was performed in a 3T MR Philips Achieva with use of 3 dimensional T1, T2 and T2* mapping sequences. The coil used for this experiment is the head and neck sense coil. T1 mapping was per-

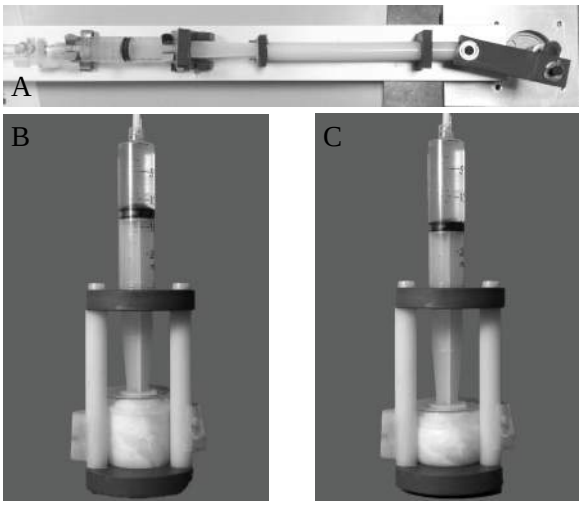

Fig. 3.7 Hydraulic motor unit for the cryogel. The rotational motion of the stepper motor is translated to regressing motion to the piston (A), which deforms the phantom from a position without stress (B) into full stress position (C). (Soultanidis et al. (2013a), © IEEE 2013)

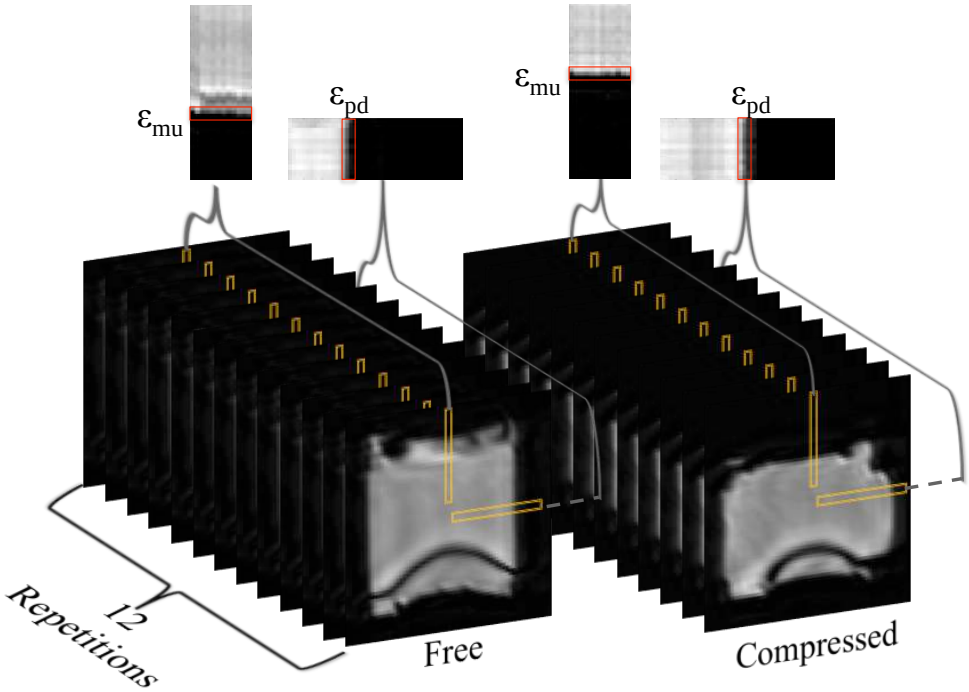

Fig. 3.8 Graphical representation of the method for "*motor unit error*" (ε_{mu}) and the "*phantom deformation error*" (ε_{pd}) calculation. (Soultanidis et al. (2013a), © IEEE 2013)

formed with the use of a sequence that employs 2 non-selective inversion pulses with inversion times ranging from 20 to 2000 *ms*, followed by 8 segmented readouts for 8 individual images. The 2 imaging trains resulted in a set of 16 images per slice with increasing inversion times. For T1 mapping, the acquisition parameters were as follows: 3D fast-field multi-echo sequence with FOV = $50 \times 50 \times 62$ *mm*, matrix = 64×51, in-plane resolution = 0.8×1.2 *mm*, measured slice thickness = 2 *mm*, slices = 25, repetition time/echo time = $3/1.6$ *ms*, flip angle = 10°. T1 values were computed on a pixel-by-pixel basis with the use of in-house Matlab software (Blume et al., 2009; Makowski et al., 2011). T2* mapping was performed using a 3D coronal fast-field multi-echo sequence. transverse images were acquired with TR = 107 *ms*, TE = 4.6 *ms*, echo spacing = 6.9 *ms*, 6 echoes, flip angle = 35°, FOV = $50 \times 50 \times 62$ *mm*, acquired matrix = 64×61, acquired resolution = 0.8×1 *mm*, slice thickness = 1 *mm*, slices = 50, averages = 1. T2 mapping was performed using a coronal turbo spin echo sequence with multiple echoes with, TR = 380 *ms*, TE = 14 *ms*, echo spacing = 14 *ms*, 5 echoes, FOV = $50 \times 50 \times 62$ *mm*, acquired matrix = 64×61, acquired resolution = 0.8×1 *mm*, slice thickness = 1 *mm*, slices = 50. Multiple regions of interest were classified according to compartment and relaxation values were obtained.

3.3.5 Motor unit and motion reproducibility

In this experiment a motor unit is designed to compress the phantom in order to deform it in a controllable and reproducible manner. An inexpensive hydraulic system, as presented in Figure 3.7, comprises the main part of the motor unit so that it remains MR compatible. For that purpose, a stepper motor (Sanyo Denki CO., Ltd.) is used to produce a continuous rotation, which is then translated into a sinusoidal motion by a piston. The motion pattern could be sinusoidal or more complex as long as it is programmed by the user. Utilization of long water-filled tubes transfers the compression into a second piston located inside the MR bore, which then applies the force to the phantom. A computer interface board controls the

stepper motor (PhidgetStepper bipolar 1-motor controller, Phidgets Inc.). This motor unit is capable of providing continuous sinusoidal motion or stop & shoot acquisition. During the experiments, the maximum compression achieved was about 17 mm. The experiment is set up accordingly, so not to reach the compression threshold.

The reproducibility of motion is estimated by measuring the error of positioning reproducibility. The experimental set-up included the motor unit, along with a 10% PVA homogeneous cryogel. The phantom was repositioned consecutively, from uncompressed to full compression for 12 times and scanned with a 3T MR Philips Achieva. A gradient echo sequence for dynamic acquisitions with 1.2 *mm* isotropic spatial resolution was acquired . The scan duration was 15.45 *s* (TR / TE 2.4 *ms* / 0.85 *ms*, 20° flip angle). The images were classified according to the position (compressed - uncompressed). A large amount of 1D profiles were used to evaluate the deformation reproducibility. Figure 3.8 represents the methodology to measure the error in motor unit and deformation of the phantom, for one profile at each case. The edge of the phantom was defined by calculating the position of the half maximum intensity (in *mm*). The error is derived by averaging the standard deviations of the edge positions and shown in Eq. 3.

$$\varepsilon = \frac{1}{M}\sum_{i=0}^{M}\sqrt{\frac{1}{N}\sum_{j=0}^{N}(x_{i,j}-\bar{x}_i)^2} \tag{3.3}$$

where $x_{i,j}$ is the edge of the phantom at each profile (in *mm, i*) upon sequential images *(j)*. Even if the deformation is identical, the errors introduced by the motor unit may affect the homogeneity of the distribution. For that reason the measurements of error are divided in two parts. The first source of error is the motor unit (ε_{mu}). It is assessed by comparing multiple line profiles at the compression surface (upper part of the cylinder). The second source of error comes from the deformation of the phantom (ε_{pd}). This aspect is assessed by comparing multiple line profiles at the cylindrical surface.

3.3.6 Compressibility of PVA cryogel

This part of the study evaluates the compressibility of the cryogel. For that purpose, a Computed Tomography (CT) experiment was performed. The goal was to measure the variation of volume between uncompressed and fully compressed phantom. For this experiment, a homogeneous 10% PVA cryogel phantom was created, following the internal compartment's preparation process. The scanner used was a General Electric Discovery STE PET/CT. By using the CT unit with 140 *kV* and 500 *mAs* we obtained images with $0.2 \times 0.2 \times 0.62$ *mm* voxel size for the PVA phantom in two states; uncompressed and with 1 *cm* compression approximately. The total volume was then measured by use of ITK-SNAP (*version 2.2*, *itksnap.org*), along with the mean and standard deviation. The calculation of the volume's variation is performed with multiple volumetric estimations. A variation of the volume will indicate if the density has changed by compression (Yushkevich et al., 2006).

3.3.7 Use of PVA cryogel for SPECT/CT acquisitions

As a nuclear medicine phantom, PVA cryogel phantom can been used for image quantification experiments in SPECT imaging. SPECT imaging belongs to the family of nuclear medicine, where the radiomolecules emit gamma radiation. In SPECT, projections of the single photons are acquired in multiple angles and the reconstructed image presents the distribution of the radiomolecules inside the compound object.

In this experiment, spherical moulds were created for the generation of spherical phantoms. These phantoms contain 10% PVA, ^{177}Lutetium colouring and water. The sphere diameters are 5 *mm*, 10 *mm*, 15 *mm*, 20 *mm*, 30 *mm* and 40 *mm* as shown in Figure 3.9. The activity concentration is approximately 0.3 MBq/ml. The scans were performed with the Philips Precedence system (dual-head gamma camera with 5/8 NaI detector crystals and a diagnostic 16-slice CT scanner) using a protocol for 177Lu-Dotatate therapy dosimetry imaging: 128 projections (64 angles per camera head) at 20 seconds per projection with a

matrix of 128×128 and a zoom of 1.18.

3.3.8 Acquisition of simultaneous PET and MR data

A demonstration experiment has been performed for the PVA cryogel with a simultaneous PET-MR system. The acquisition was performed with the use of the HYPERimage scanner and the 3T MR Philips Achieva (Schulz et al., 2009). The HYPERimage scanner, which will be described in the next chapter with more details, contains an integrated 2-channel T/R coil for the MR. In this experimental setup a stop and shoot acquisition was followed with 9 different positions of compression. For each of these 9 positions of the phantom, an MR scan was performed using a gradient echo sequence for dynamic acquisitions with 1.2

Fig. 3.9 The PVA cryogel moulds. The sphere diameters are: 5 *mm*, 10 *mm*, 15 *mm*, 20 *mm*, 30 *mm* and 40 *mm*

mm isotropic spatial resolution and 0.515 *s* temporal resolution for a total volume acquisition (TR / TE 2.4 *ms* / 0.85 *ms* 20° flip angle). The purpose of using this sequence is to emulate any dynamic acquisition in a real time PET-MR motion tracking experiment (Soultanidis et al., 2011). Each PET acquisition lasted 3 *min*. 2D filtered back projection (FBP-2D) for each gate of PET data has been performed using the STIR library (Thielemans et al., 2012). The phantom itself consists of 10% PVA cryogel, combined at the interior volume with 2.25 *MBq/ml* of ^{18}F-FDG and 50 $\mu l/ml$ of Gadolinium solution (Gadopentetic acid). The latter was used to enhance MR contrast and create more realistic tissue non-uniformities.

3.4 Results

3.4.1 Preparation of cryogel phantom

The purpose of this first step of the study was to determine the optimum percentage of PVA. Three options were evaluated: 5% 10% and 15% by weight PVA. A phantom constructed using the 5% option was not capable of sustaining its shape, therefore it was rejected. Using 10% PVA the phantom sustains its original shape. The 15% PVA cryogel could sustain the original shape of the phantom, but our motor unit did not have the power to overcome its resistance. Therefore, the most appropriate percentage of PVA concentration for our experimental design was determined to be 10% by weight. By applying the new methodology, a phantom was constructed, with well-defined shape and size appropriate for small animal imaging. This phantom has an internal compartment which follows the motion of the external cell and contains the radiotracer that makes it visible to PET as well. The combination of the radiotracer with the gadolinium solution gives complementary information needed for motion correction and a new approach to the design of PET-MR phantoms for simultaneous experiments.

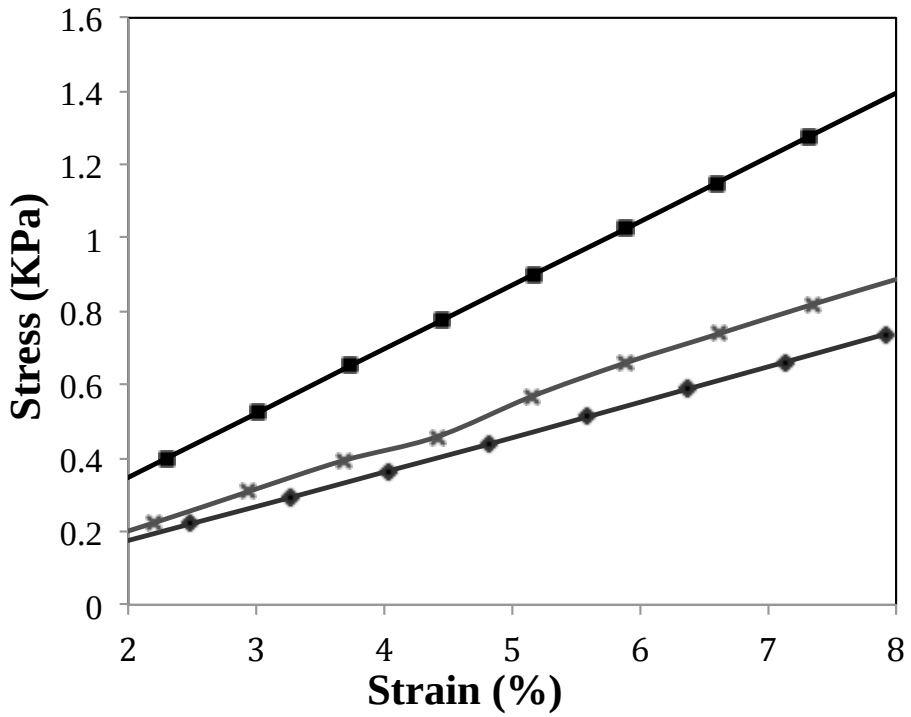

Fig. 3.10 Stress as a function of the strain where marked with ■ is the standard process with 12 *hours* freezing and 8 to 9 *hours* process (*method 1*), with ✖ is the 3 *hours* freezing at –80 °C with 3 *hours* thaw (*method 2*) and with ♦ is a 10 *hours* freezing at –20 °C followed by a 3 *hours* freezing at –80 °C and 3 *hours* thaw (*method 3*). (Soultanidis et al. (2013a), © IEEE 2013)

Table 3.2 Young's modulus in kPa

	method 1	method 2	method 3
1^{st} phantom	17.4 ± 0.2	7.9 ± 0.8	10.8 ± 0.5
2^{nd} phantom	14.7 ± 2.0	9.2 ± 0.2	11.1 ± 0.5

3.4.2 Young's Modulus

An example of stress over strain results is presented in Figure 3.10 for the phantom made of 10% PVA and the Young's modulus are presented in Table 3.2. Error values are extracted by calculating standard deviation of multiple measurements. The reproducibility of the elasticity results is measured by comparing the phantoms created with the same method. The difference of elasticity between methods 2 and 3 is not as big as the variation when using method 1. The large measurement variation in method 1 can be explained by the increased roughness of the phantom's mounting surface, obstructing a clean measurement of Young's modulus. The fast freezing procedure of water creates lumps on the free surface of the phantom. Thus, the compression mechanism does not force uniformly the surface leading to inaccurate measurements.

3.4.3 Diffusion of the radiotracer

In Figure 3.11 an example of the two images is presented from the dynamic scans with a difference of 45 *min* between each scan start time, with the radiation decay taken under consideration. It is observed that higher concentration areas lose activity, which is redistributed to low concentration areas (dark areas in the subtraction image). From the line profiles created and by investigating various positions through the phantom, the edge of the distribution advanced approximately 2 $mm\ h^{-1}$.

Over a time span of 3 hours, 12 PET scans were performed. Two samples of the entire image for total intensity were taken by the 1^{st} and 12^{th} scan. Results are presented in Table

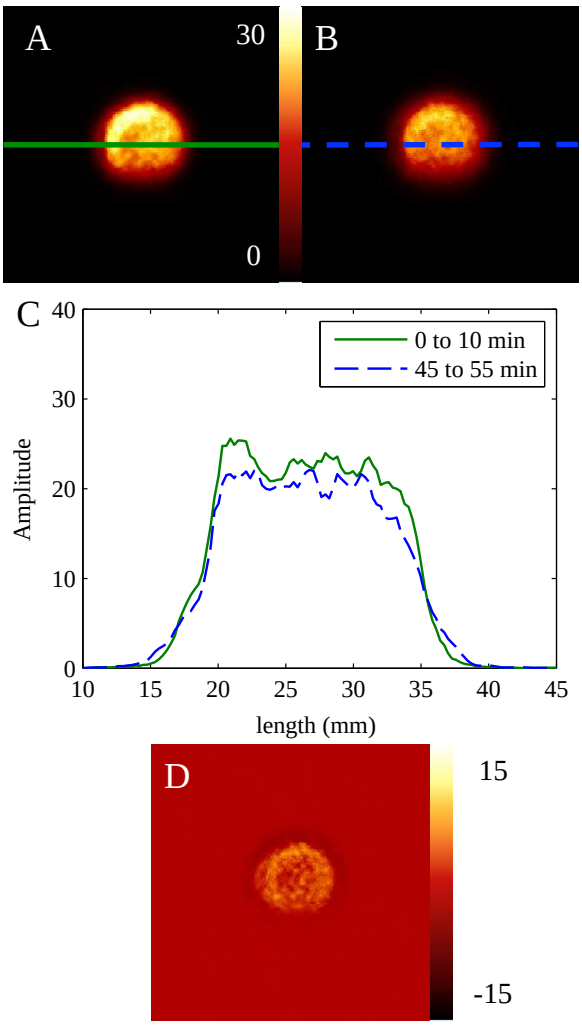

Fig. 3.11 Example of 10 *min* acquisitions for investigation of diffusion inside a phantom: (A) is the acquisition between 0 and 10 *min*; (B) is the acquisition between 45 and 55 *min*; (C) is the line profile for (A) and (B); (D) is the difference of distribution between (A) and (B). (Soultanidis et al. (2013a), © IEEE 2013)

Table 3.3 Total image uptake

Uptake of 1^{st} scan (0-10 min)	Uptake of 12^{th} scan (165-175 min)	Variation (%)
181583	178647	1.63

Table 3.4 Radioactivity concentration over time

Sample number	line equation	R	variation of uptake per hour
$1^{st} sample$	$y = 0.023x + 15.57$	0.94	0.67
$2^{nd} sample$	$y = -0.017x + 25.93$	0.96	-0.52
$3^{rd} sample$	$y = 0.019x + 1.10$	0.99	0.58

3.3. It is important to remind that decay correction is active for this experiment. Samples of mean intensity in three position for each 12 scans were taken. These samples are cubic with edge size of 5 mm. The positions were selected to reflect the heterogeneity seen in the phantom. One position with high concentration, one with low concentration and one outside of the active area. These positions and the corresponding amplitude variations through time are presented in Figure 3.12. Trend-line equations for these three samples are presented in Table 3.4, with the predicted variation of intensity per hour, as it is calculated by the trend-line equations.

3.4.4 Relaxation values for PVA cryogel

From the images obtained, relaxation times were measured for multiple regions of interest. The overall mean values of relaxation measurements are given in Table 3.5.

Table 3.5 Relaxation Values For 10% PVA Cryogel

Compartment	T1 (ms)	T2 (ms)	T2* (ms)
External	1317 ± 23	98 ± 8	191 ± 36
Internal	106 ± 16	122 ± 30	4.5 ± 0.56

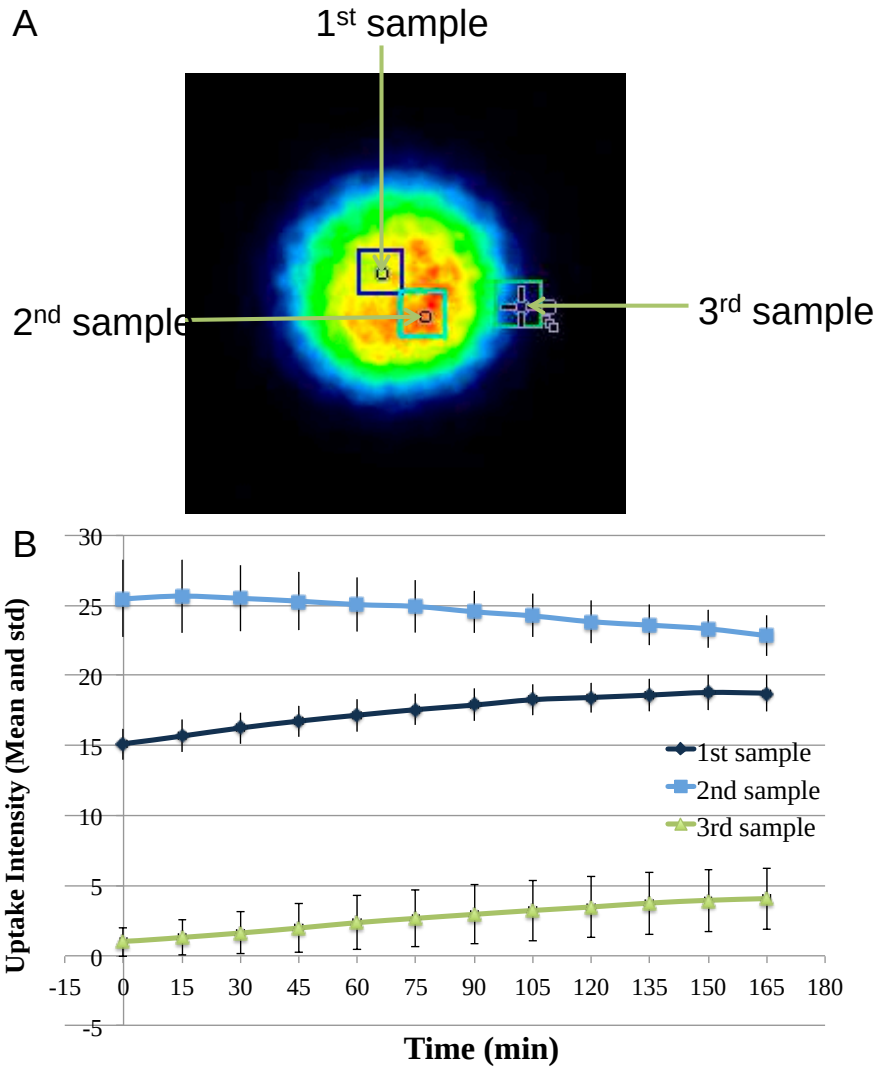

Fig. 3.12 A) Three samples of same volume in locations with various concentration. B) Activity concentration over 3 hours period.

3.4.5 Motor unit and motion reproducibility

In total, *296* profiles have been generated and the corresponding errors were calculated. Of those, 168 1D profiles were used for the motor unit error (ε_{mu}) and 128 1D profiles for the phantom deformation error (ε_{pd}). The values are given in Table 3.6.

Table 3.6 Error of Motion Reproducibility

	Uncompressed	Compressed
Motor unit - (ε_{mu})	0.88 *mm*	0.26 *mm*
Deformation - (ε_{pd})	0.26 *mm*	0.14 *mm*

3.4.6 Compressibility of PVA cryogel

The 3 dimensional surface renders of an uncompressed and a compressed phantom are presented in Figure 3.13, where the maximum compression of the phantom is about 1 *cm*. The variation in volume is given in Table 3.7. It is calculated that the variation of volume between these two states is about 0.2% of the initial volume (i.e it is negligible) and there is no significant difference in Hounsfield units (H.U.) and attenuation coefficients at 511 *keV* (μ) between the two states.

Table 3.7 Volume variation through compression

	Uncompressed	Compressed
Volume (cm^3)	40.2 ± 0.3	40.1 ± 0.3
H.U. ($mean \pm std$)	20.5 ± 3.9	21.3 ± 4.2
μ (cm^{-1})	0.0941 ± 0.0002	0.0942 ± 0.0002

3.4.7 Use of PVA cryogel for SPECT/CT acquisitions

Picture 3.14 presents the results of two different scans with the same spheres. The first step is to scan the PVA cryogel spheres in air. This experiment gave the recovery curve of the

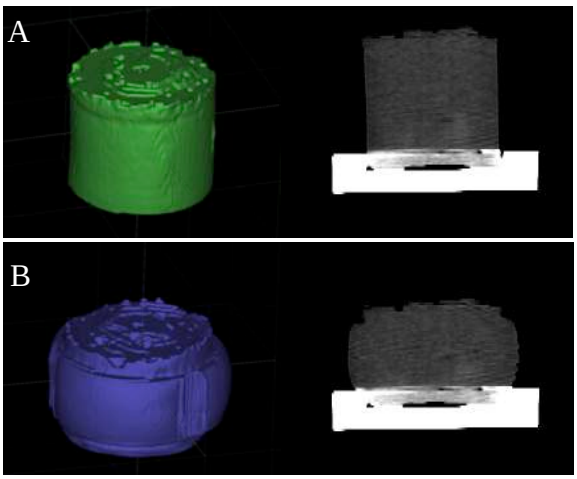

Fig. 3.13 CT acquisition of PVA cryogel in two states; (A) uncompressed and (B) compressed, with 3D volume rendering and coronal slice of the phantom. (Soultanidis et al. (2013a), © IEEE 2013)

spheres. The next step is to submerge the spheres within water. The diffusion is prevented by use of liquid latex. the spheres are scanned with the SPECT/CT and the result of this scan is given in figure 3.14.c.

3.4.8 Simultaneous Acquisition of PET and MR data

Data from the simultaneous acquisition are shown in Figure 3.15. The two compartments of the PVA phantom are visible. Except from the discretized compartments, the texture of the external compartment is heterogeneous, which is a realistic feature as it mimics the appearance of real tissue in MR experiments. This effect is a result of the alterations regarding the preparation procedure and the use of moulds. There appears to be a decrease of counts at the final compression point even with decay correction. This might indicate the alteration of attenuation characteristics of the phantom during the motion.

By analysing the figure 3.15 line profile, a Full Width at Half Maximum can be estimated. By acquiring this information it is realized that the phantom is compressed by 11.2 *mm* in the vertical axis.

Table 3.8 Axial FWHM for extreme PET positions

Gate No	FWHM (mm)
Gate 1	35.4 *mm*
Gate 9	24.2 *mm*

3.5 Discussion

The protocol followed was: a rat sized (i.e. 4 cm diameter), 10% PVA cryogel phantom, introduced with the most common radio-molecule (^{18}F-FDG) and with the time of preparation reduced by 14 *hours* to 6 *hours*. It has been demonstrated that the elastic properties are reproducible following multiple repetitions of the preparation procedure. The modification of the standard production procedure resulted in a reduction of elasticity up to 50%, which is acceptable for our purposes.

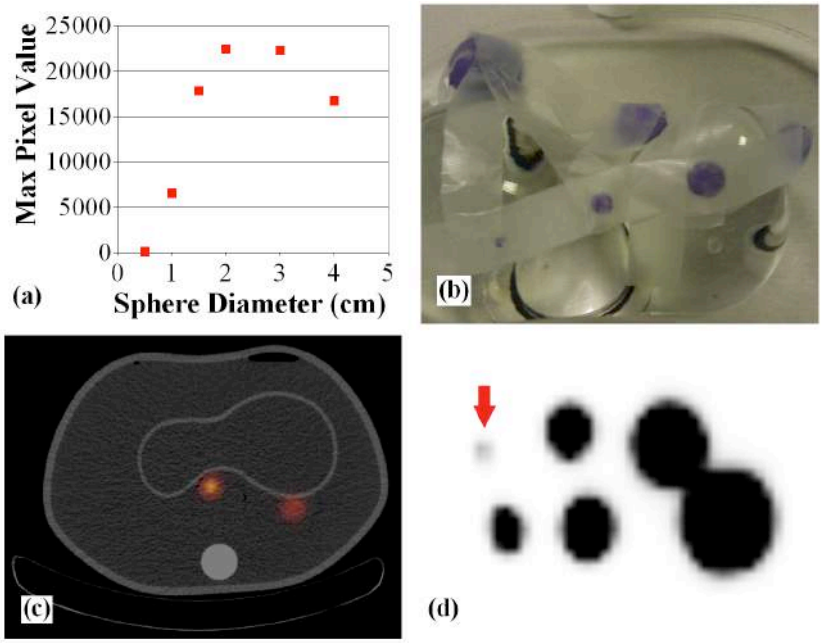

Fig. 3.14 (a) The recovery curve produced for the 'in air' data; (b) The position of the PVA spheres in the torso phantom; (c) A slice through the SPECT/CT image of the spheres in the torso phantom; (d) The maximum intensity projection (MIP) of the SPECT image windowed to show that the smallest sphere, indicated by the red arrow, is just visible

The stability of the elastic properties after repeated compressions was evaluated. The maximum deviation is observed in *method 1* with the standard deviation 17% of the mean

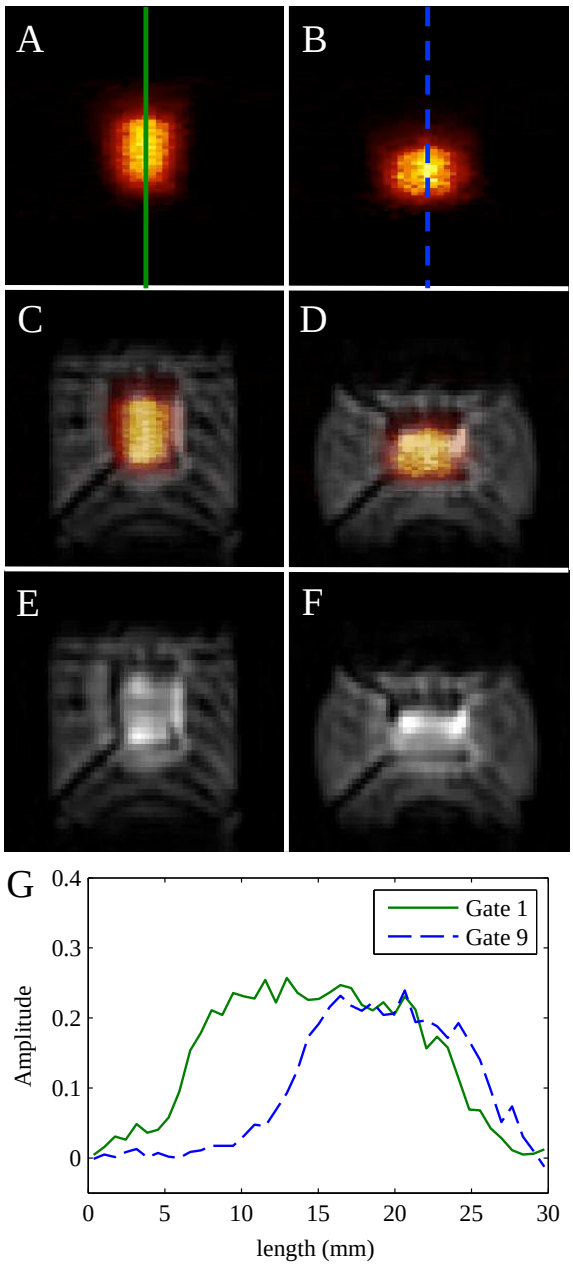

Fig. 3.15 The PVA cryogel in a simultaneous acquisition where, (A) and (B) are the PET extremities, (E) and (F) are the MR extremities and (C) with (D are) the fused extremities for the PET-MR acquisition. (G) is the line profile of PET data when uncompressed (Gate 1) and fully compressed (Gate 9). (Soultanidis et al. (2013a), © IEEE 2013)

value. *Methods 2* and *3* have 15% and 3% deviation respectively. Moreover, the elasticity variation between the various preparation methods is not large, indicating a similar behaviour for the two compartments in the phantom during compression.

The examined PVA cryogel has Young's modulus between 8 to 11 *kPa*. It is found that it has a higher elastic modulus than liver, which varies between 0.6 to 1.73 *kPa* (Yeh et al., 2002). By comparing with other soft tissues, PVA cryogel has a lower Young's modulus than normal breast tissue which varies from 18 *kPa* to 35 *kPa* with mild pre-compression of the tissue (5%) and prostate which varies between 55 *kPa* and 65 *kPa* (Krouskop et al., 1998). Finally, literature indicates a large difference in Young's modulus which is between the currently studied PVA cryogel and a healthy vascular adventicia, which is about 80 *kPa* (Fromageau et al., 2003).

PVA cryogel is created with 90% water, a poorly compressible liquid ($\beta = 4.6 \times 10^{-10}$). Consequently, density changes under compression are most unlikely to happen. The compressibility experiment results confirm this expectation, and the volume of the phantom does not change significantly when a load is applied.

For this protocol, the measured rate of diffusion of ^{18}F-FDG was 2 *mm/hr*. This means that the phantom cannot be used for long experiments involving many hours of acquisition. However, diffusion is relatively small for PET experiments with the acquisition time up to approximately 30 minutes. Any alteration of the preparation protocol is likely to change the diffusion characteristics of the phantom. Consequently the diffusion rate needs to be measured in phantoms made with different sizes, structures, PVA concentration, contrast / labelling agents, or freeze-thaw procedures.

In addition to the diffusion observed inside the PVA, the evaporation of water is another factor that affects the long-term use of PVA cryogel. Given that diffusion is accelerated inside water, the PET-MR phantom cannot be stored in a liquid medium as is common for MR phantoms. After exposure to room temperature and humidity for three to four hours,

the effects of drying are clearly visible on the external surface of the phantom. The external surface dries out. This leads to the conclusion that the phantom has to be used as soon as it has been produced and then safely disposed. In case the procedure requires radionuclide with long half-life (i.e. ^{64}Cu), various techniques have to be applied to conserve humidity such as the refreezing of the phantom after each use. This procedure has been performed by others with MR PVA phantoms but in this case an increase of Young's modulus was observed (Duboeuf et al., 2009).

The reproducibility of motion is satisfactory. In particular, the deformation error is lower than 1 *mm*. On the other hand, the motor unit introduces additional errors at the fully uncompressed position. This indicates that the repositioning of the uncompressed phantom is less accurate at the edges. For that reason, it is recommended to keep the phantom with a small compression during scan (e.g. 2 *mm*).

The alteration of the freeze-thaw process contributed to the creation of a compartmentalized phantom, capable of performing non-rigid motion and visible by PET and MR. Furthermore, because of the variations to the preparation procedures of this phantom, an heterogeneous signal is observed in the MR images. The additional structure provides a more realistic environment to validate registration algorithms for motion correction. Eventually, the use of a long half-life isotope such as ^{64}Cu, could avoid the need to alter the standard protocol, with dehydration remaining a limiting factor.

The size of the PET-MR PVA cryogel phantom is an important aspect. The current protocol is oriented towards the use of PVA inside small animal imaging systems. The diameter of the PVA cryogel is comparable with the diameter of a rat. In order to consider constructing a phantom for a human scanner, the stability of the material under its own weight must be considered. There are several options, of which two appear to be the most favourable: (i) The use of higher PVA concentration, or (ii) the use of rigid supporting materials. Of these, the second is more realistic as it more closely represents the anatomy of

a living organism, where the soft tissue is supported by stronger connective tissue and the entire structure is located upon a rigid structure.

The use of the PVA cryogel phantom for PET-MR studies is the initial step. The most significant part of this study has been to overcome the limitations of using locally rigid moving phantoms, which was the classical method used in a number of previous studies. The nature of tissue deformation and how this is modelled, e.g. by a process involving a registration algorithm, maybe useful in the development of procedures to correct PET images for the effects of motion using MR-derived motion fields (Gigengack et al., 2012). After applying this deformable motion inside MR - a hostile environment for motor units - the potential use of it could be expanded in SPECT-MR/CT and Ultrasound/MR for motion studies. The possibility of mixing PET-SPECT-MR-CT contrast agents or even the change of PVA concentration could lead to creation of customizable phantoms with a vast range of structures. An additional advantage of this phantom is the geometrical reproducibility which results from using the same moulds. With a reproducible structure, the experimental results will also be more reproducible.

Artefacts upon MR image are important to be acknowledged and accessed. The biggest artefact upon an MR image is at the bottom of the phantom. This is visible in MR (Figure 3.15) but the corresponding CT image does not give any deterioration (Figure 3.13). There are no evidence of how it is formed. The same effect is visible in all the phantoms created with this mould. In order to answer this conclusively, more investigation has to be performed upon the freezing-thaw process.

An aspect of a PVA cryogel phantom that can be investigated in further detail is the size of the smallest object we can create. This aspect requires future studies.

The potential uses of PVA cryogels have grown in a number of imaging modalities and it is also used in MR for temperature dosimetry (Lukas et al., 2001) and even in radiotherapy for internal dosimetry (Hill et al., 2002). The field of radiotherapy moves towards

4D treatment planning with dose painting of the target region (Ling et al., 2000). Towards this goal, PVA cryogel could be used for imaging with PET-MR/CT or ultrasound and 4D radiotherapy treatment planning.

3.6 Conclusions

We created a phantom with simple but realistic structure based on PVA cryogel material. This, PET-MR compatible phantom, can be utilized for evaluation of motion correction algorithms. The upgrade of the standard MR phantom to be PET visible led to modifications of the preparation procedure. The effects of the changes have been measured and taken into account for further investigations. This procedure can be applied with various alterations. Diverse structures with numerous shapes and sizes can potentially be created. Furthermore, this phantom has the advantage of being deformable in a reproducible manner, an important aspect for an investigation of motion correction of soft tissue structures. The free customization of the cryogel phantom combined with the low cost of production provides a valuable tool for use in applications of motion correction for a variety of simultaneous and / or sequential multi-modality experiments with PET-MR and beyond (e.g. SPECT, CT and ultrasound).

Chapter 4

Motion correction of 2D PET-MR data with continuous motion

4.1 Introduction

The aim of the experiments described in this chapter was to develop the methods for acquiring simultaneous PET and MR images from an object that is subject to non-rigid deformation continuously and demonstrate the feasibility of motion correction of PET images using motion information calculated from the MR data. Data from a similar phantom has been reconstructed before (Tsoumpas et al., 2010). However, this experiment was performed in a stop and shoot mode, the data were collected over very long scan times and there was no intra-frame motion. By controlling the motion automatically, the aim is to perform the acquisition in real time, with realistic data rates and realistic MR sampling times and to include intra-frame motion.

4.2 Materials and Methods

4.2.1 PANDA II PET insert

PANDA stands for PET and NMR Dual Acquisition (Garlick et al., 1997). This original system uses the technology of indirect detection of scintillation light. The light is transferred from scintillation crystals in the imaging ring out of the MR magnetic field influence with the use of 3 metre long optic fibres. There, non-MR compatible photomultipliers can be used for the signal detection.

PANDA was upgraded to PANDA II which is constructed with 4 rings of Lutetium Oxy-orthosilicate (LSO) crystals (Mackewn et al., 2005). This upgrade brought higher sensitivity to the system. With the increased sensitivity, the ring diameter could increase, leading to a ring with an interior diameter of 75.5 *mm* and transaxial field of view about 60 mm. The axial field of view contains only one ring and the axial field of view is 3 mm. The resolution of the scanner close to the centre was 1.5 *mm* and it dropped to 2.5 *mm* towards the edge of the field of view. The scanner was used in conjunction with a Philips Achieva 3T clinical MR scanner. The optical light is detected by 8 Position Sensitive Photomultipliers with 64 channel each. The read out is processed and stored as list mode events. These listmode events contained the two crystal coordinates and the time stamp for each coincident event. The coil used for this scanner was a Philips sense head 8 channel coil. Figure 4.1 presents the PANDA PET insert and the placement of the object to be imaged is shown in figure 4.2 .

4.2.2 Phantom and Motor unit

A PET-MR phantom capable of non-rigid deformation was used (Tsoumpas et al., 2010). This phantom, as presented in figure 4.3, consists of a rotational part (external ring) and a static part (internal disk). The external ring rotates rigidly, but the overall deformation of the phantom follows a non-rigid transformation. The phantom is divided into three groups of

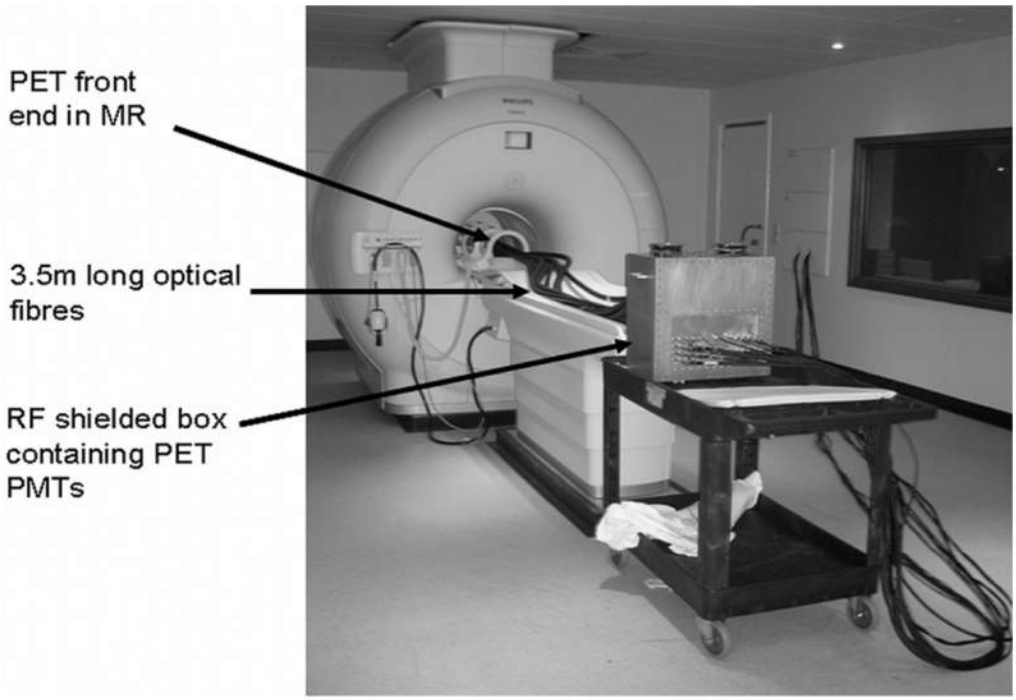

Fig. 4.1 PANDA II insert with the Philips Achieva 3T MR scanner. (Mackewn et al. (2005), © IEEE 2005)

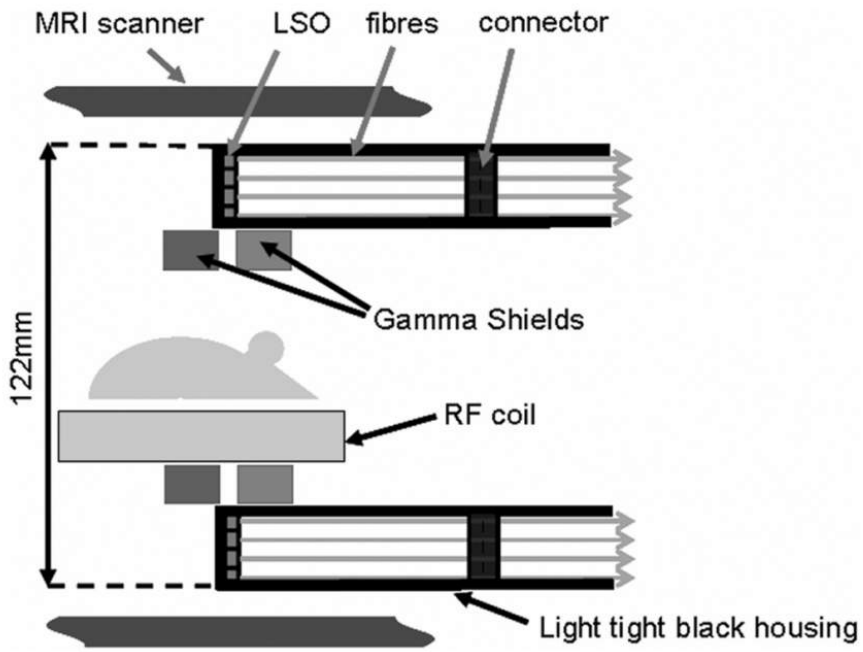

Fig. 4.2 Concept design of a PANDA II acquisition. (Mackewn et al. (2005), © IEEE 2005)

rods with diameters of 3, 4 and 5 mm. For this study the phantom is filled with ^{18}Fluoride, water and colouring ink.

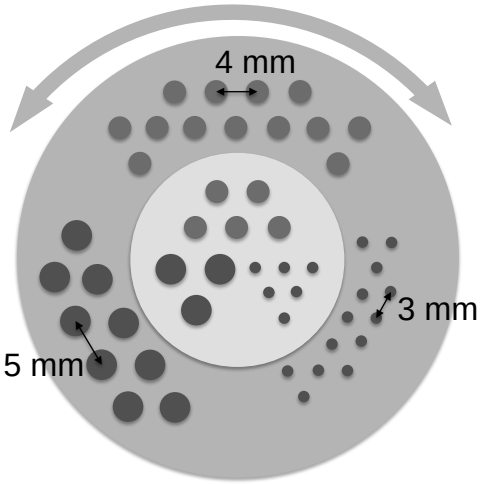

Fig. 4.3 CAD representation and physical image of the rotational phantom. In this phantom, the exterior part rotates freely around the interior static part with 360 ° freedom

The system has been modified such that continuous variable motion can be transmitted

during PET-MR acquisitions. This is achieved with the use of a carbon fibre rod and a stepper motor (Sanyo Denki CO., Ltd.). This stepper motor gets the signal from a Phidgets stepper driver, which is controlled via USB by a Macbook Pro. A specific C++ function was created for this study, where the Phidgets stepper motor dictates the period and the amplitude of the motion. For this experiment, the motion applied is rotational with the angle varying in a sinusoidal pattern, with period of 5 *s* and total rotation of 20°. This displacement corresponds to 8 mm average displacement for the hot rods. The stepper motor is placed at the edge of the MR table, firmly attached to the carrying trolley for MR safety reasons. Because the stepper motor cannot work inside the magnetic field, it was placed as far as possible from the MR scanner. A 3.5 m carbon fibre rod was used to connect the rotational part of the phantom to the stepper motor and motion is transferred through it as Figures 4.4 and 4.5 illustrated.

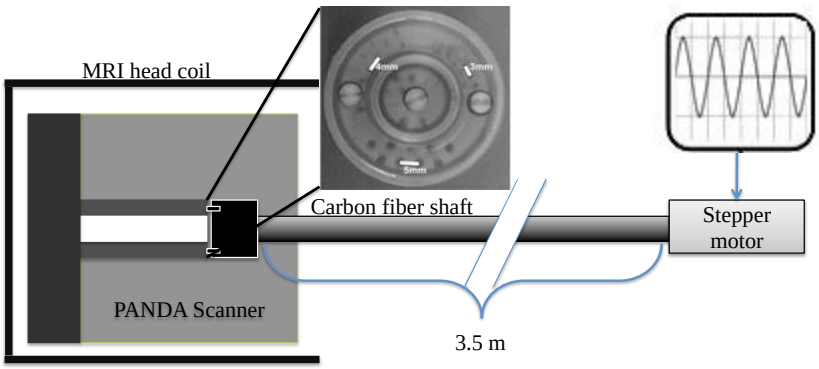

Fig. 4.4 Experimental setup for the rotational phantom, the phantom is shown in the inset box. The PANDA scanner encloses the rotational phantom where, through the carbon fibre rod, a sinusoidal motion is provided by the stepper motor to the external ring of the phantom. (Soultanidis et al. (2011), © IEEE 2011)

Fig. 4.5 PET-MR experimental setup with the PANDA II insert, the Philips Achieva 3T scanner and the rotational phantom, driven by a 3.5 m carbon fibre rod. (Soultanidis et al. (2011), © IEEE 2011)

4.2.3 Synchronization and alignment of PET and MR co-ordinate systems

Temporal synchronization was not performed at the hardware level for the PANDA II insert. The method used to synchronize the acquisitions was simply to initiate the PET and MR scanning at the same time, manually.

The alignment of the PET and MR co-ordinate systems was performed with use of the rigid registration algorithm of IRTK applied to the phantom data itself. The registration target area included only the non-rotating interior of the phantom itself. This transformation was then used to align all images before motion correction was applied.

4.2.4 MR and PET acquisition

The MR acquisition was performed with the sense 8 channel receiver head and neck coil. The spatial resolution of $1 \times 1 \times 10$ *mm*, was achieved with TR/TE of 3.4 *ms*/1.5 *ms* and

60 ° flip angle. The temporal resolution achieved with this MR scan for one dynamic image frame is 0.133 s. The acquisition lasted for 30 min in total, where PET and MR images were obtained simultaneously. The PET and MR data were gated according to phase into 16 different gates. Because the sinusoidal motion had a fixed period of 5 s, PET and MR data were segmented every 0312.5 ms (16 gates $\times$ 0312.5 ms $=$ 5 s) and rebinned into the corresponding gates. Phase gating ensured the equal distribution of time consumed for each frame, leading to no need to take under account the acquisition duration during motion correction. By keeping steady sinusoidal signal with the stepper motor, positioning reproducibility within phase is secured. The PET images were reconstructed with use of filtered back projection (FBP), provided by the STIR Library.

The method followed for motion correction is the Reconstruct-Transform-Average (RTA) with FBP reconstruction . The motion information was extracted from the MR with use of the hierarchical adaptive local affine registration toolkit, developed by Buerger et al. (2011). The applied methodology is described in figure 4.6. The data were divided into 16 different gates. Verification of synchronization between PET and MR is obtained by comparison of the reconstructed PET and MR images. After the verification that PET and MR are in the same phase, each MR gate is registered with the reference MR gate (position zero) in order to obtain the transformation matrix, required to correct the corresponding PET gate. The corrected PET gates were then averaged to obtain the final motion corrected image.

4.3 Results

Figure 4.7 gives some examples of the motion correction for a single PET and MR gate. This process has been applied to 16 gates and the corrected gates were averaged are presented in figure 4.8. In figure 4.8, the results of the motion correction can be compared, not only with the uncorrected PET image but with a similar, motionless acquisition. Line profiles are drawn through the three regions of interest for this picture and presented in figure 4.9.

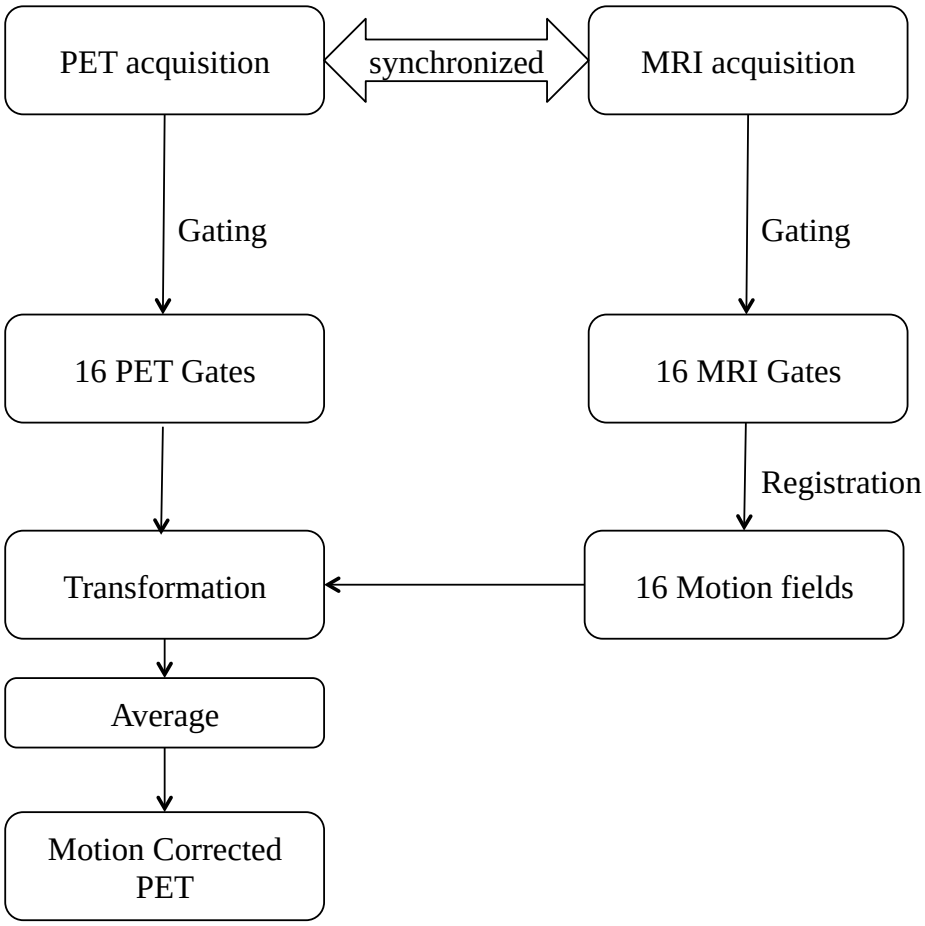

Fig. 4.6 Motion correction methodology

The motion correction can be characterized by measuring the peak to valley ratio in line profiles through the hot rods. The peak to valley ratios for static, blurred and corrected images and for different rod diameters are shown in Tables 4.1, 4.2 and 4.3.

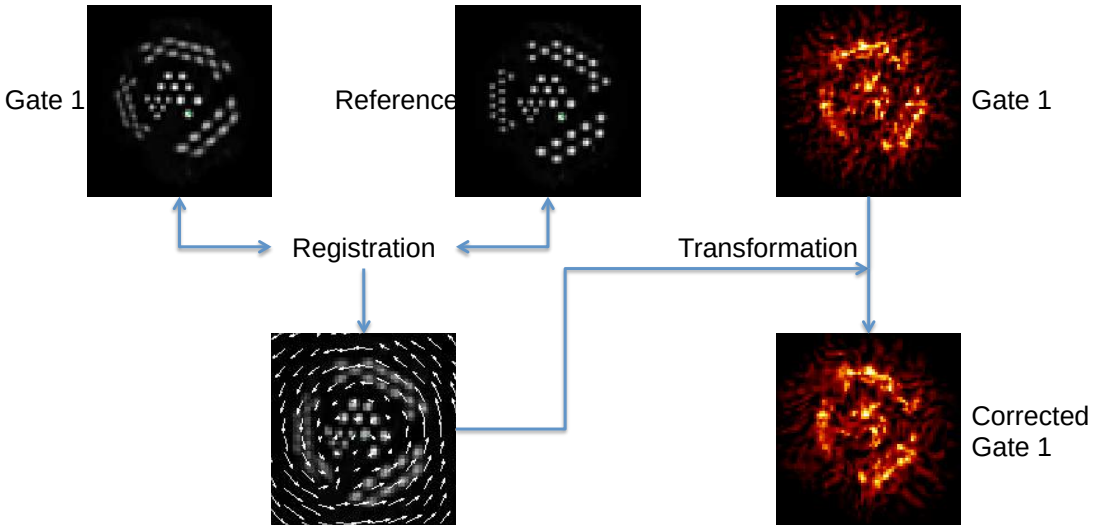

Fig. 4.7 Demonstration of a single frame motion correction, where MR Gate 1 is registered to the reference MR gate to obtain the motion field. The transformation is then applied to the corresponding PET gate

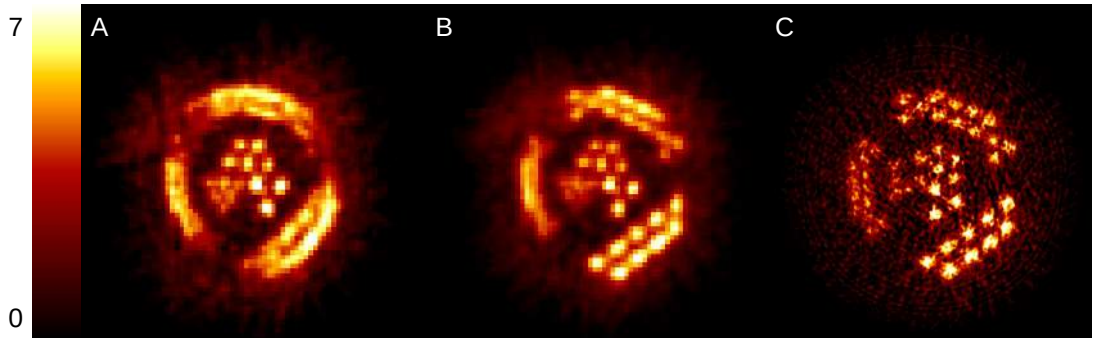

Fig. 4.8 PET images of the (a) uncorrected, and blurred PET data, compared with the (b) corrected PET, after using MR motion information and (c) similar acquisition, without motion. (Soultanidis et al. (2011), © IEEE 2011)

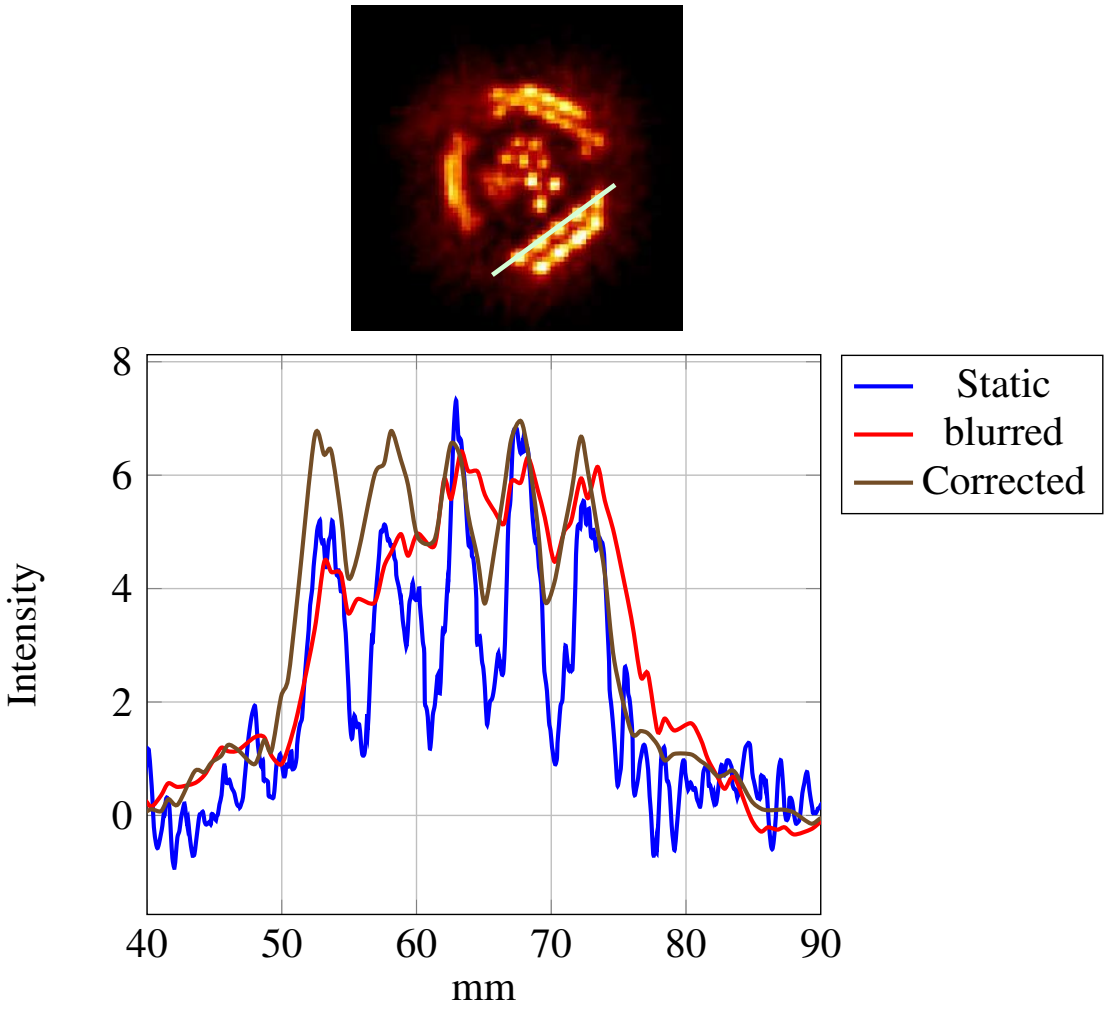

Fig. 4.9 Line of profile for the 5mm diameter cylinders

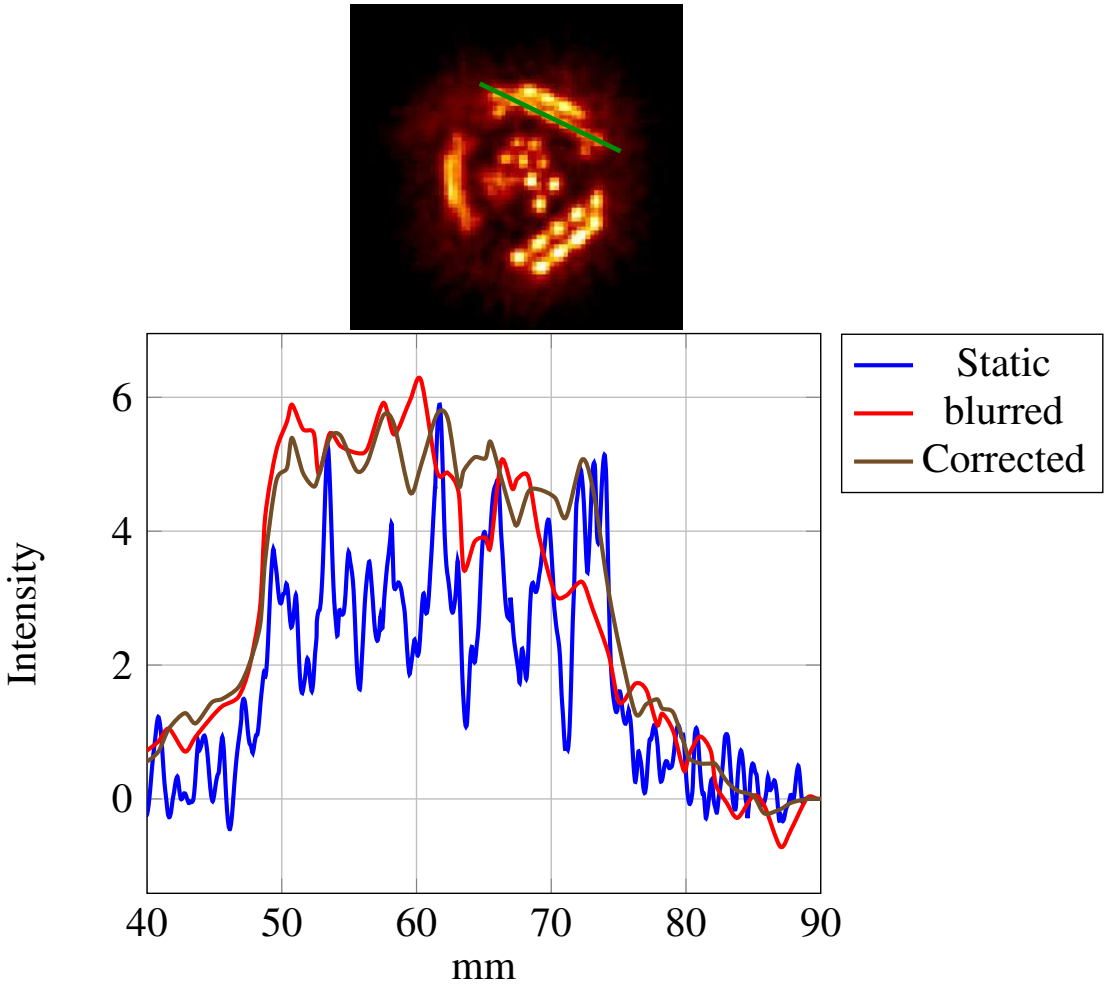

Fig. 4.10 Line of profile for the 4mm diameter cylinders

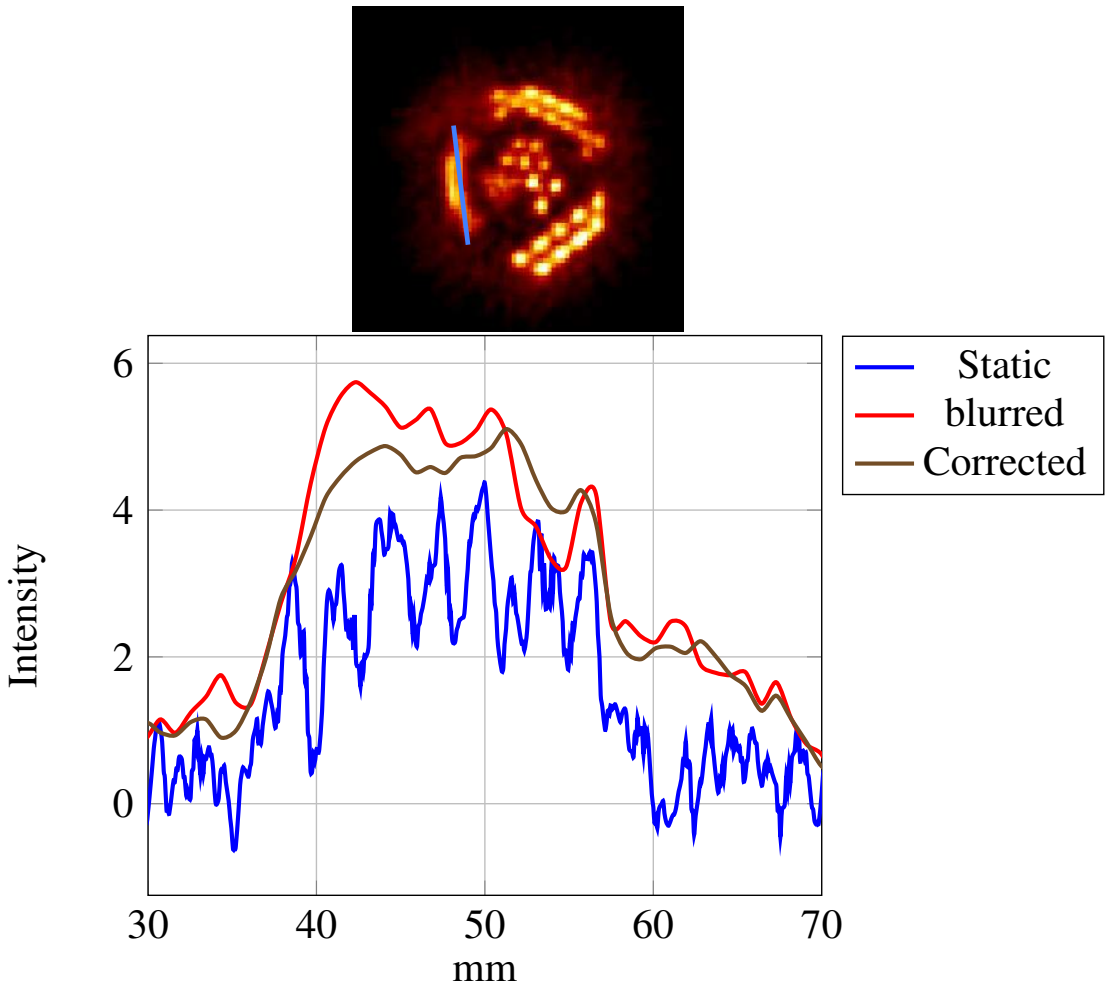

Fig. 4.11 Line of profile for the 3mm diameter cylinders

Table 4.1 Peak-Valley Intensity Ratio for 5 mm diameter

	Mean	Std Error
static	2.60	0.28
blurred	0.99	0.07
Corrected	1.64	0.09

Table 4.2 Peak-Valley Intensity Ratio for 4 mm diameter

	Mean	Std Error
static	2.07	0.32
blurred	1.03	0.11
Corrected	1.35	0.09

Table 4.3 Peak-Valley Intensity Ratio for 3 mm diameter

	Mean	Std Error
static	1.53	0.27
blurred	1.05	0.07
Corrected	1.07	0.06

4.4 Discussion

In this experiment, the main goal is to explore the methodology for a simultaneous PET-MR experiment with continuous motion. The first goal was to generate controlled motion. The motor unit has been developed to be compatible with the magnetic field and for that reason, it was placed as far away from the magnet as the photomultiplier box. The continuous motion of the phantom generates motion artefacts and intra-frame motion. This intra-frame motion is visible in figure 4.7, where the cylinders of the MR image in Gate 1 are slightly blurred.

Because we used a sinusoidal motion pattern, the post processing of the data was an easy task, because the phase was predetermined, and the necessary step was to create the temporal segments (i.e. gates). For that reason, we chose to perform the gating according to

phase and not amplitude.

The limitations of the scanner do not give the opportunity to use iterative reconstructions and investigate alternative methods of reconstruction and motion correction. For that reason, we followed the RTA methodology for correction. By taking into account visual representation and the peak-valley ratio, motion correction is mostly successful for the 5 mm rods, less successful with 4 mm rods and not successful with the 3 mm rods. Even if some recovery of the intensity of the rods is visible in the individual reconstructed images, the blurring due to the averaging of multiple gates brings blurring to the corrected images. Furthermore, according to calculations, the phantom's maximum velocity is 5 mm/*s* approximately. This means that a frame of 312.5 ms, the cylinders travel for 1.57 mm. This, intra-frame motion contributes to the elongation of the cylinders in the direction of motion, and it is not possible to correct for this. The method to overcome this problem could be the increase of the number of gates, but each gate would have poorer statistics and the final motion correction would not be usable. Probably, motion compensated image reconstruction could provide better perspectives (Qiao et al., 2006). Nevertheless, the final results are comparable with the results presented by Tsoumpas et al. (2010), by using the same scanner in a stop and shoot experiment.

4.5 Conclusions

In this section was performed an experiment with continuous motion. This helped to establish an experimental methodology, for more realistic simultaneous PET-MR experiments which includes hardware and data handling methodologies, and emphasize important aspects such as the synchronization by hardware and accurate spatial alignment of structures not identically visualized with these modalities. Motion correction was applied at the PET data and an improved delineation of the longer diameter structures is clearly seen. Improvement can also be seen in line profiles, but again this is less clear for the smaller features .

This is attributed mainly to the fairly poor signal to noise ratio with the PET scanner and the intra-frame motion.

Chapter 5

Motion correction for 3D PET-MR data with a limited field of view PET insert

5.1 Introduction

The aim of work described in this chapter is to demonstrate the implementation and evaluation of simultaneously acquired MR motion information to motion correct dynamic PET images, taking into account a more realistic 3D motion acquisition and correction. Experiments have been performed using the non-rigid phantoms described in the *chapter 3* and using the HYPERimage PET insert. This builds on the experiment designed in chapter 4 and extends it to doing a fully 3D dynamic acquisition and using an elastically deformable phantom.

5.2 Materials and Methods

5.2.1 Scanner

The HYPERimage scanner is an MR-compatible PET insert designed to be paired with the table of a Philips Achieva 3T MR scanner (Schulz et al., 2009). The purpose of the insert is the establishment and development of studies with small animals for simultaneous PET-MR acquisition.

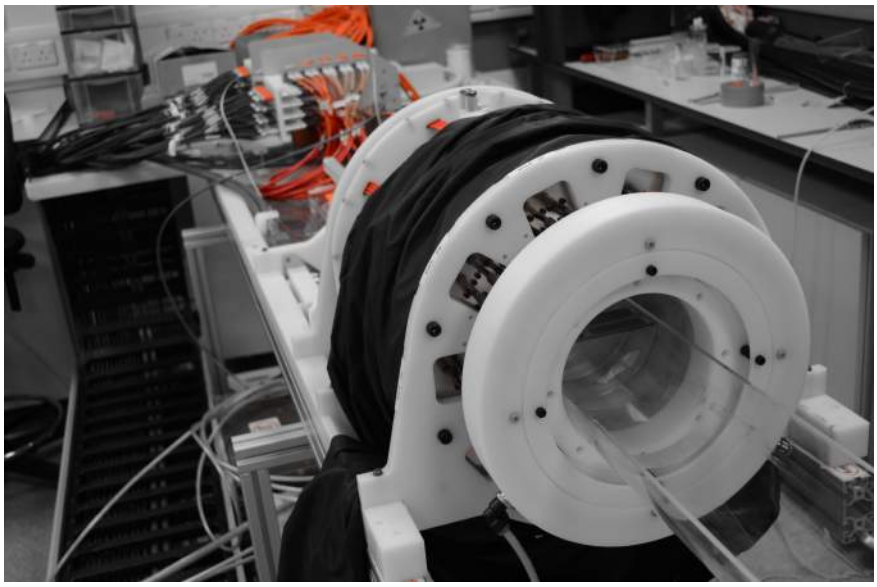

Fig. 5.1 HYPERimage PET insert

The PET element of the scanner consists of Lutetium Yttrium Orthosilicate (*LYSO*) crystals, coupled with Silicon Photomultiplier (SiPM) detectors, for higher magnetic compatibility. The crystals used are composed of a matrix of small elements, bound together. This is a 22 $\times$ 22 crystal array where each element's dimensions are 10 $\times$ 1.3 $\times$ 1.3 mm^3. The basic component of the PET system is the stack. Each stack of the scanner consists of three components. The crystal block, the ASIC tile and the interface tile - FPGA module. A group of 6 stacks makes up one 'module' and the PET annulus is made up of 10 modules. In the prototype system used, each module is only populated with two stacks out of the

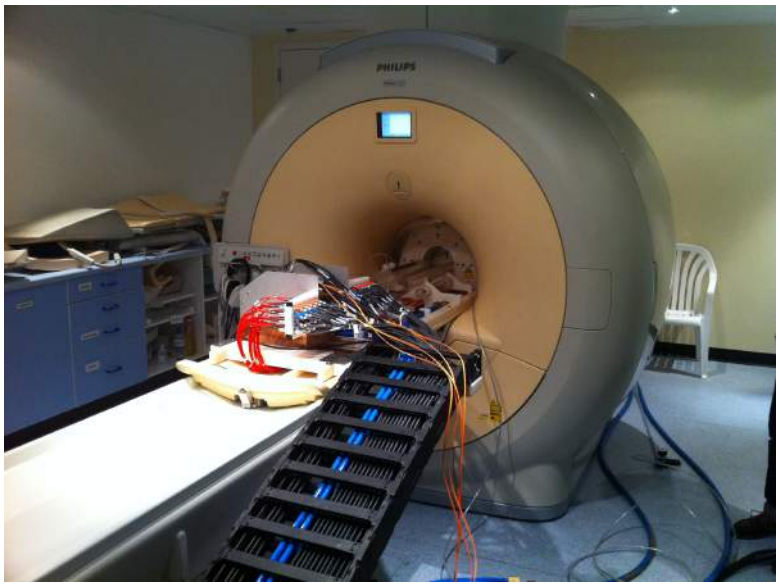

Fig. 5.2 HYPERimage PET insert inside the Philips Achieva 3 Tesla MR scanner

maximum capacity of six stacks. Signals are transferred to and from modules via optical fibre for minimum magnetic interference. Each module is shielded with a 50 μm thick copper RF - screen. The transverse field of view is 160 *mm* diameter. The potential axial field of view for this scanner is 99 *mm* but, as the modules are only populated with two stacks each, the axial field of view for PET is only 33 *mm*. The spatial resolution of the scanner is about 1.6*mm* or better (Schulz et al., 2011). Recent experiments Literature mention that the FWHM is just under 2.3 mm in the transaxial direction when single slice rebinning (SSRB) and 2D filtered back-projection (FBP) is used for reconstruction, and 1.3 mm FWHM when resolution modeling is employed (Mackewn et al., 2015). The electronic parts are cooled with liquid and air cooling. Compressed air of 1 bar pressure flows around the electronics and the stacks are cooled down with continuous flow of cooling liquid at 15 ° C. The components of the insert inside the MR room include in addition to the PET itself, the power unit, providing individual power to each SPU. The long optic fibres lead the signal outside the MR room to the control room, where no magnetic interference is present. Also, outside the MR room is the water cooling system and the data acquisition computer. The air cooling

is provided by the hospital supply, inside the MR room.

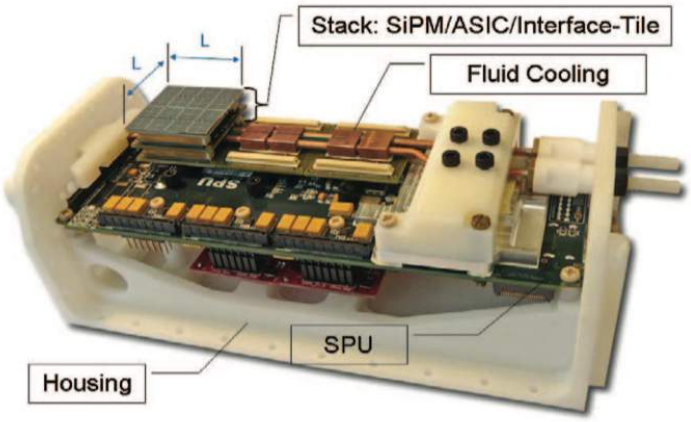

Fig. 5.3 HYPERimage module with one stack installed. (Schulz et al. (2009), ©IEEE 2009)

Raw data from the PET insert is passed to a DELL server (128 *GByte* RAM, 4 $\times$ AMD Quad Core CPU). The data are stored and processed in order to give a data stream of detection coincidences in listmode format. This listmode format contains information regarding the crystal/stack/module of origin, along with timing and energy information. The file is formatted as a binary file with no header file. For information about crystal, stack or module, a short integer is reserved. A floating point, 32 bit number is reserved for the timing information. In total, 20 Bytes are reserved for each event. The acquisition and monitoring of the scanner is performed with *'HYPERION'* - software designated for this generation of PET inserts. Through HYPERION, the user can perform all necessary functions the scanner can provide and also monitor the system. This software is located in a PC, separate from the DELL server but connected through Ethernet cable.

The RF-coil used with this PET scanner is attached to the scanner between the perspex bed and the PET modules. It is equipped with a 2-channel, 16 element transmit/receive birdcage coil. The transaxial field of view of the coil is 140 mm and the axial 120 mm. The signal is transferred to the MR with a custom made acquisition unit. Because of the large field of view, this MR coil is particularly suitable for imaging rabbits.

For simultaneous acquisitions, the scanner is placed on top of the MR patient bed and secured with use of plastic screws. With the use of the MR positioning lasers, the centre of the PET scanner's field of view is aligned approximately with the magnet isocentre. After placing the PET scanner inside the MR gantry, further MR table movement is avoided. This helps the conservation of alignment of PET with MR during the various experiments. Because of the nature of the scanner, an alignment test should be repeated in each experiment. The complete system with the power supply and optic fibres connected is presented in figure 5.2. Figure 5.4 is a representative image of a simultaneous acquisition for the HYPERimage scanner. The phantom contains small spheres and it has been reconstructed with OSEM reconstruction (5 subsets, 7 iterations). Resolution modelling was used during the reconstruction (Mackewn et al., 2012, 2015).

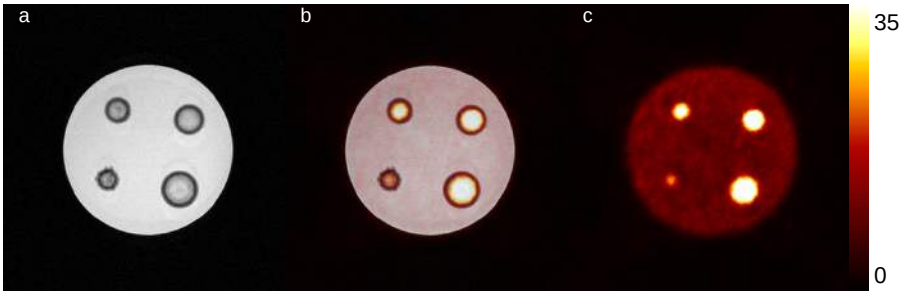

Fig. 5.4 Simultaneously acquired images of a phantom containing four small spheres with internal diameters of 3.95 *mm*, 4.95 *mm*, 6.23 *mm* and 7.86 *mm*. a) MR image, b) fused PET/MR image and c) PET image

5.2.2 Importing HYPERimage raw data into the STIR library

STIR reads sinograms in interfile format or ECAT files. The lack of sinogram output by the HYPERimage scanner led to the need to convert the data to this format. The data conversion from the raw hyperimage listmode file format to sinograms, compatible with STIR library (version 2.2), was achieved by customizing the relevant sub-routines of the STIR library. The modified function is based upon the algorithm that converts GATE data into

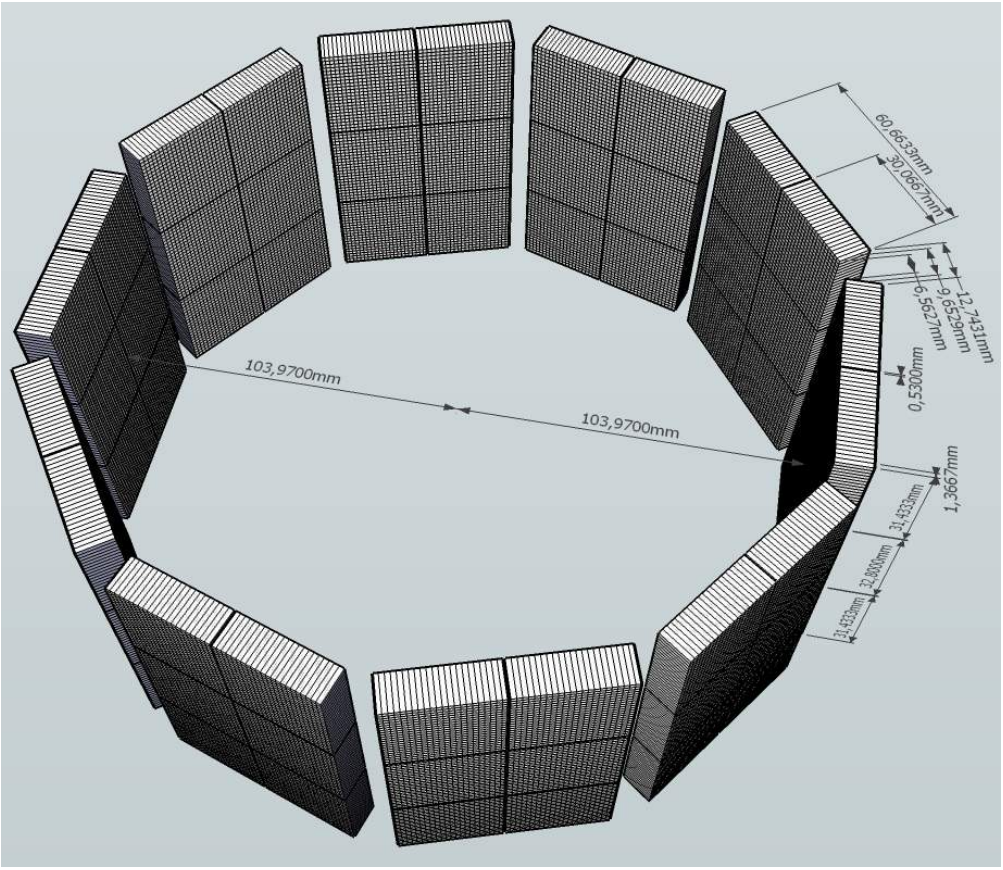

Fig. 5.5 3D representation of HYPERimage's stacks and modules. (Salomon et al. (2012), ©IEEE 2012)

STIR sinogram format. The implementation includes the creation of a lookup table, which converts the crystal/stack/module orientation into sinogram coordinates and maps each Line of Response to the corresponding sinogram location. During this conversion of the listmode data, the gap between modules must be taken into account and this was addressed by creating additional non-active crystals in order to fill the gaps. The gaps are treated in this way because of limitations in the reconstruction algorithm. STIR assumes that a PET scanner has a cylindrical form, where the detectors are equally spaced around the perimeter of each ring. If the areas with no crystals are not included, crystals will be assigned to locations where there should be gaps, and the final geometry is deformed. Therefore, the areas without detection crystals are also considered part of the scanner and the geometry. The gap between each module is 6.56 mm, as it is presented in 5.5. Given that each crystal has 1.3 width, the best approximation is the addition of 5 ”inactive” crystals into the sinogram between modules, in order to preserve the scanner's geometry in reconstruction. The effect of having "virtual" crystals that do not acquire any data must be dealt within the rest of the reconstruction process.

5.2.3 Normalization of PET data

A common problem with the PET detectors in general is the non homogeneity of the detection process. Some of the detectors may be more sensitive than others. This fluctuation of sensitivity has to be compensated and corrected during PET reconstruction. The reconstruction provided with the PET insert is optimized for self normalization. This feature is not available in STIR algorithms, where the normalization scan has to be taken into account. For this scanner therefore, a normalization sinogram has been constructed with the following method.

As figure 5.6 describes, a homogeneous phantom with diameter of 94 mm and width 40 mm was scanned. The phantom is presented in figure 5.7. The phantom was placed in the

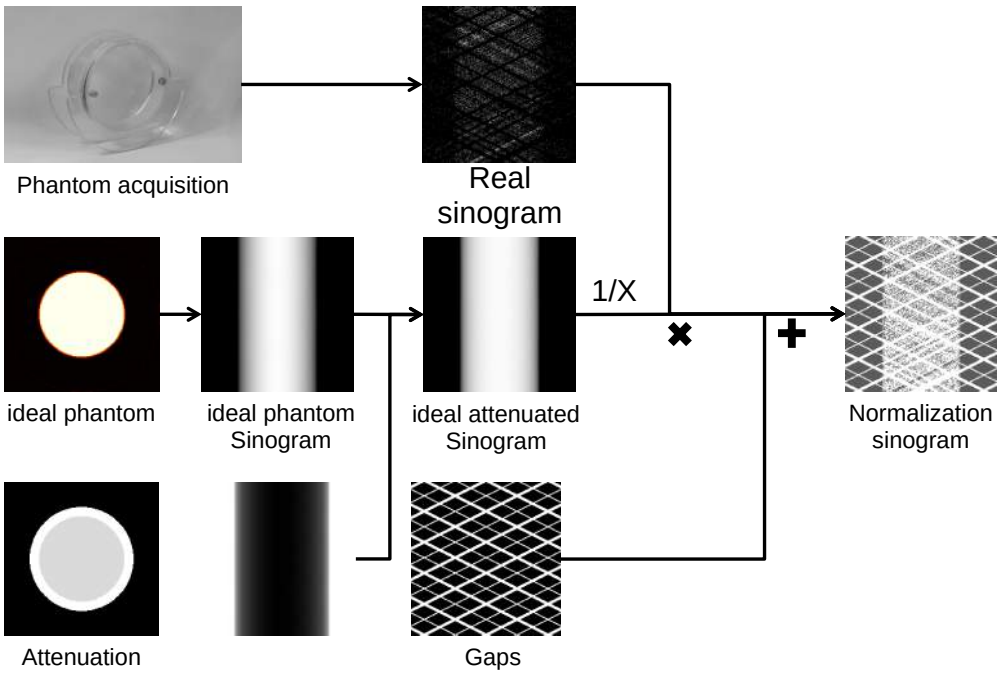

Fig. 5.6 Workflow for the production of normalization sinogram

isocentre of the scanner. The known dimensions of this phantom were used for the generation of a computational phantom which is forward projected with fwdtest STIR utility. By forward projecting the ideal emission and attenuation factors, we simulate an ideal acquisition of the phantom. The normalization sinogram is created by dividing the real acquisition of the homogeneous phantom with the ideal phantom. An addition to this procedure is the gap treatment during the normalization phase. A high value of normalization will suppress any signal from the gap areas and it will enhance the surrounding signal. For STIR, the value of the gaps is recommended to be higher than 5×10^6.

This sinogram is used for the normalization of PET sinograms during the reconstruction. It is simply multiplied with the attenuation coefficient of the sinogram under normalization.

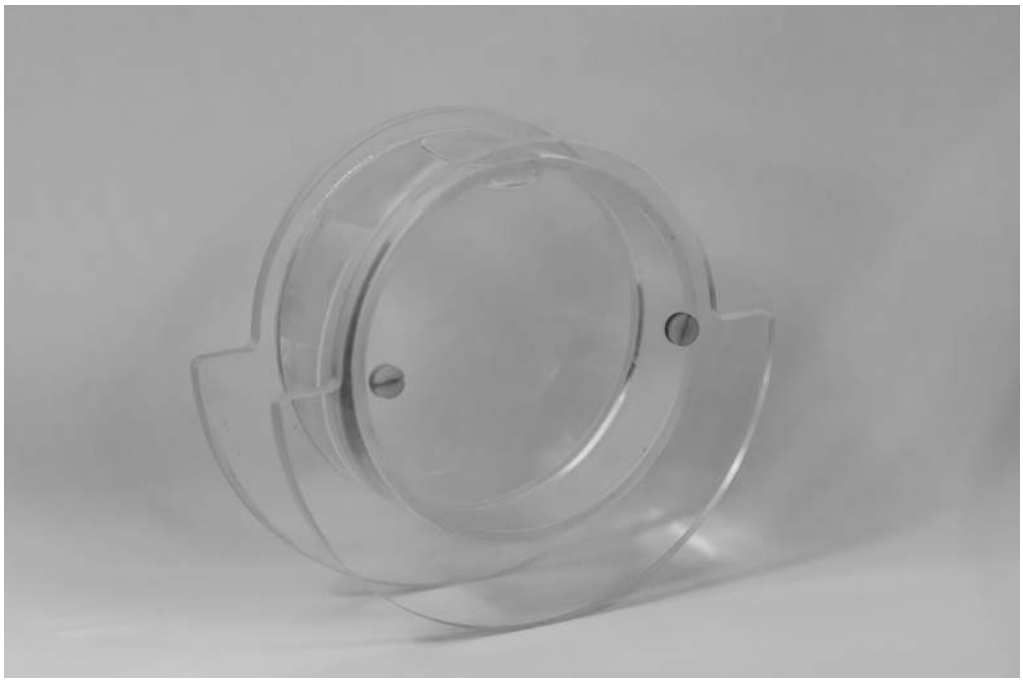

Fig. 5.7 Homogeneous phantom for normalization scan

5.2.4 Creation of phantom motion within the PET-MR field of view

In order to evaluate effectiveness of simultaneously acquired MR to correct for effects of motion on PET images , it is necessary to acquire PET-MR data from a moving non-rigid phantom within the PET-MR field of view. Various approaches to this problem were implemented in the experiments performed with both the PANDA and Hyperimage scanners. The motion generation is a key factor of the methodology and a computer controlled motor unit can help apply specific motion patterns to the phantom, capable for methodology evaluation. A motor unit is not only responsible to provide a pattern of motion but also to imitate realistic motion patterns. The realism is determined by the similarity of a motion pattern with one observed in humans. Furthermore, the MR environment is inhospitable for ferromagnetic and conducting equipment, including electrical motors. The goal of each of these motor units is to transfer motion inside the MR, with high precision and as safely as possible, causing negligible interference to the PET or MR operation.

For the HYPERimage PET insert, PVA cryogel phantom acquisitions are the most appropriate. As described in a previous chapter, the motion of the PVA cryogel cannot be considered as rigid. The motor unit for this case has to provide and maintain the appropriate deformation to the phantom. The motion can provide a crushing effect, as described in Chapter 3, or any other stress, as deemed necessary for the experiment.

The initial step requires the use of a stepper motor. Where continuous motion is not important, motors with low torque could be utilized for stop and shoot acquisitions. In these acquisitions the motor has to get to a certain position and stay there for an amount of time. The stepper motor used was a Sanyo Denki at $1A$ functional current. This motor unit has been described in Chapter 3. The main purpose of this stepper motor for the PVA phantoms is the stabilization in different positions and the acquisition of various static MR and PET images. The transfer of motion is performed with use of a hydraulic system.

For reproduction of continuous motion, a servo motor has been utilized. The experimental setup includes a Parker servo motor (N series, 3 A. current, VAC) driven by a Parker Gemini GV servo driver. By providing one digital pulse to the servo driver, the motor moves for one step. A data stream of pulses can generate continuous motion of the motor. The motion signal is given by an Arduino MEGA 2560 (D'ausilio, 2012), a USB based hardware I/O unit with digital and analogue interface capabilities. It is programmable and can perform autonomous tasks, without continuous connection with a computer. Here, the Arduino was programmed to receive via USB the target position and calculate speed, number of iterations and execute the data transmission to the servo driver. More specifically; Arduino receives a 4 bytes integer number every 0.1 s. This number is the target position for the servo motor. By already knowing the origin and the destination point, the Arduino calculates the number of necessary steps or revolutions, as known to servo motors and divides the number with the time interval of 0.1 s in order to find the period of each step. The orientation of rotation is calculated also by subtracting the origin and destination position. Finally, the Arduino trans-

mits the step action signal, along with the orientation of rotation. The code for the Arduino can be found in Appendix A.2. The 4 byte coordinates are finally transmitted to the Arduino by a homemade Java script via USB. These coordinates are given by a pre-produced waveform, depending on the experimental needs. The signal transfer was repeated every 0.1 s. This setup can reproduce any custom motion patterns with time interval of 0.1 s per step. However, this time interval may change depending the requirements. Also the Java script can be found in Appendix A.3. Figure 5.8 shows the chain of information passing from the computer to the motor unit.

The servo motor transfers the motion to the phantom through a hydraulic pump, described in Figure 5.9. The design of this pump is similar to a "pump jack", and transforms the circular motion from the servo motor into reciprocating motion. For highest durability, the frame of this pump is made out of metal. As a hydraulic pump, 10 ml syringe has been used and mounted upon the metallic structure. This pump was connected with a long 5 m PVC tube, capable to transfer the hydraulic pressure inside the MRI gantry. This PVC tube was 4 mm thick wall thickness of 1 mm. The hydraulic fluid used in this occasion was deionized water.

The use of hard plastic coated tube keeps the compression losses to a minimum. The use of similar water pistons at both ends of the hydraulic system ensures a 1 to 1 ratio of displacement. Figure 5.10 represents the two different receiver models used for these experiments. The main principal is the translation of pressure into deformation of the target. The first design was used for cylindrical phantoms with small diameter and the main motion can be characterized by expansion of the walls while compressed. The second design is for phantoms with large diameter. In this case, the structure helps the imitation of diaphragm motion.

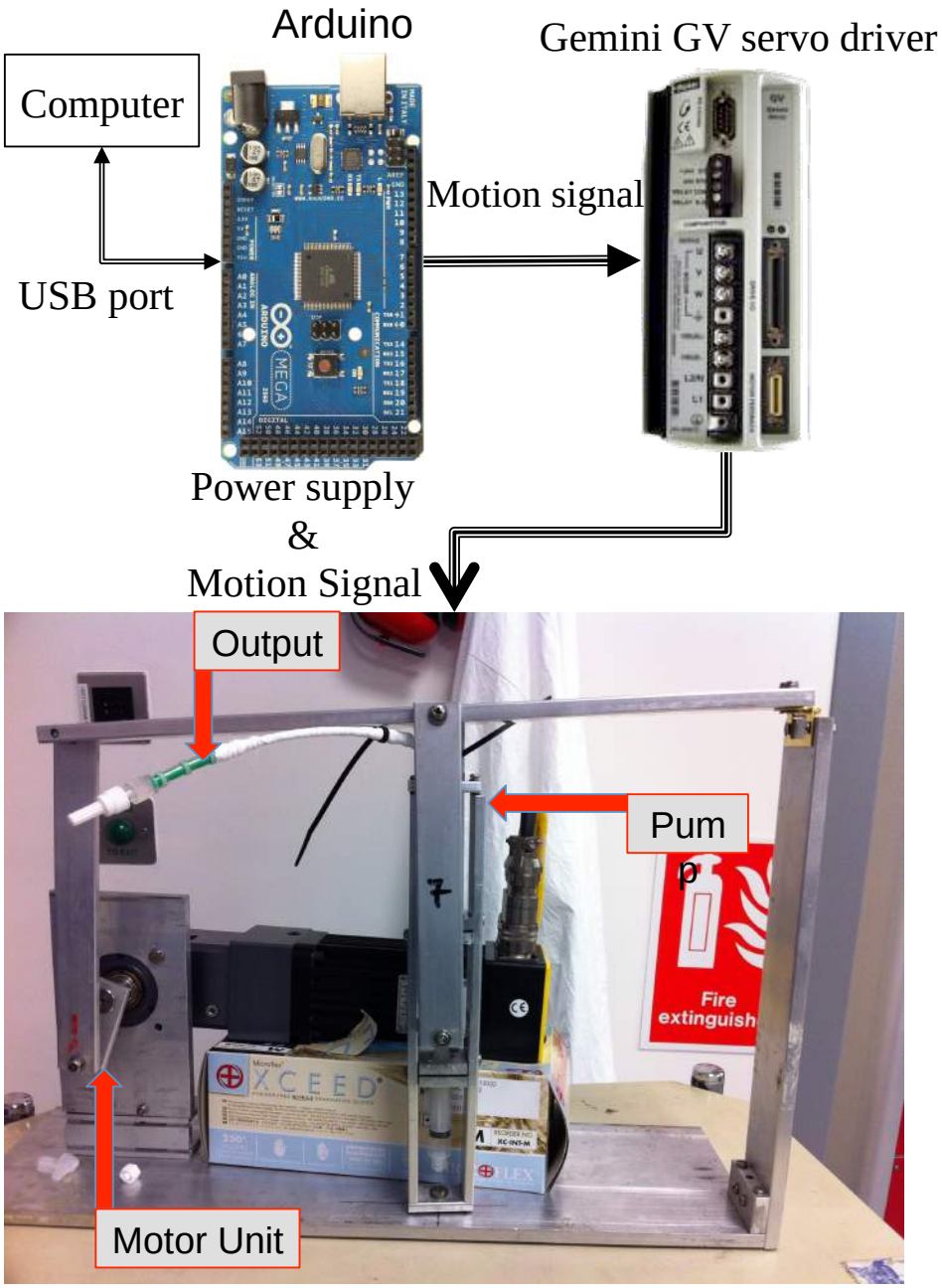

Fig. 5.8 All the stages for signal transfer. From the computer to Arduino, to the Parker Gemini GV servo driver to the servo motor and the hydraulic pump

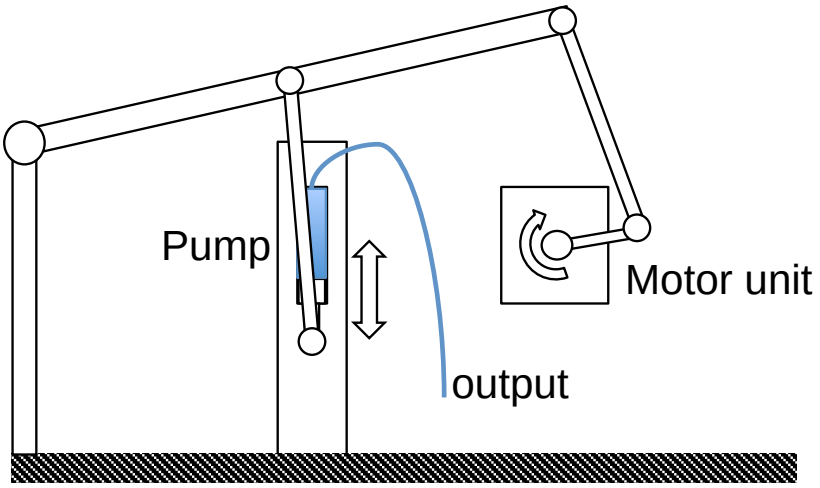

Fig. 5.9 Hydraulic pump schematics and graphical representation of function

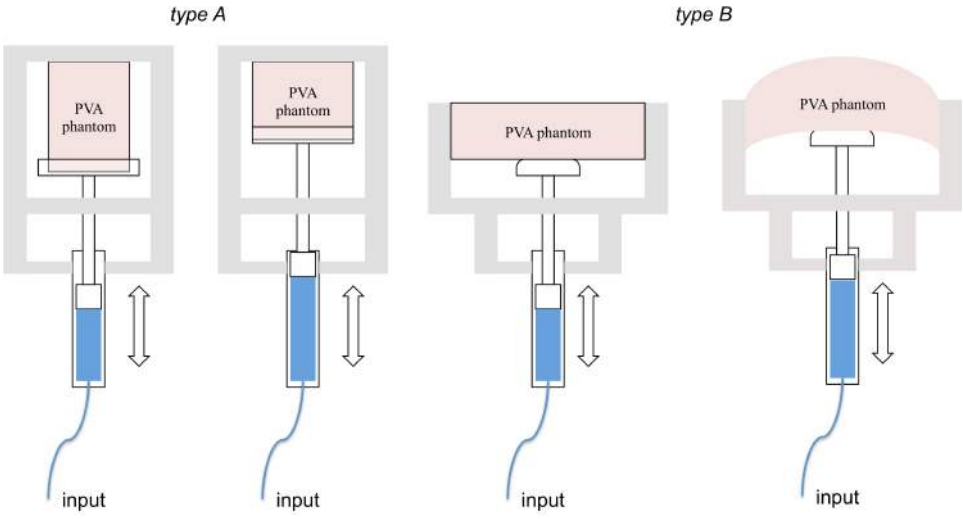

Fig. 5.10 Hydraulic pump for the two different phantom designs

5.2.5 Phantom and design adaptation

Figure 5.10 presents the two different phantoms generated for these experiments. *Phantom A*, used in the stop-and-shoot experiment, is similar to the one presented in previous studies with a hot radioactive lesion in the centre of it and a non-radioactive background. *Phantom B*, used in the continuous motion experiment, has a different design. The diameter is bigger, the height is smaller and it contains different sizes of small spheres from 3 to 7 mm in diameter. Each sphere has four times higher radioactivity concentration than the background. The two phantoms also undergo different motor-driven deformation patterns. *phantom A* undergoes a simple compression, whilst *phantom 2* undergoes a non-uniform compression (similar to the motion of the diaphragm) with the centre of the phantom moving with the highest amplitude. Figure 5.10 demonstrates each type of phantom and the corresponding deformation under compression

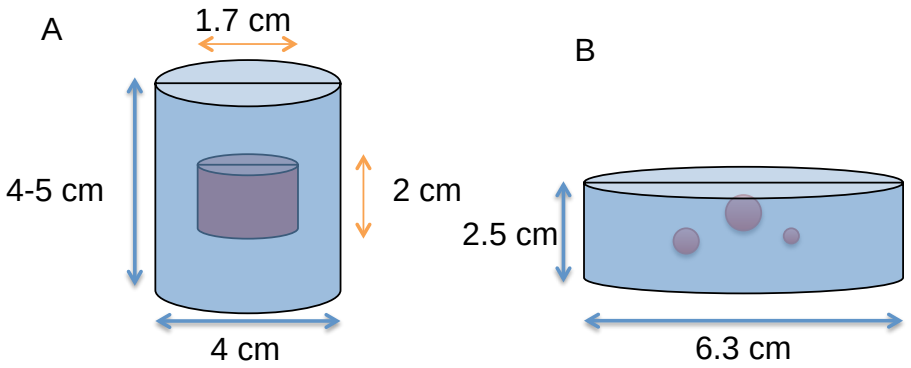

Fig. 5.11 Cryogel phantom with dimensions dedicated for small animal imaging systems with (A) a single hot region phantom with non-radioactive background and (B) a multiple lesion phantom and 4 to 1 lesion to background ratio

5.3 First experiment: 3D PET-MR with stop-and-shoot acquisition

As an early step into the use of the HYPERimage scanner and prior to the synchronization and registration methodology was available, the stop and shoot experiment was performed. In this solution, a cylindrical phantom, with diameter of 4 cm and height of 5 to 6 cm has been placed in different degrees of compression and measured with the HYPERimage scanner. The resulting PET and MR images have been used for motion correction with two correction methodologies.

5.3.1 Experimental set-up

For this experiment, the HYPERimage PET insert was used along with the Philips Achieva 3T MR. No specific motion pattern was necessary because of the nature of the experiment. As in previous demonstrations, a stepper motor (Sanyo Denki CO., Ltd.) was used to generate the increments of the motion, from uncompressed to fully compressed status. Totally, 9 gates were acquired in both PET and MR. The PET acquisition for each gate lasted two minutes, after this time period, the phantom was moved to the next position and the next acquisition was initiated for PET and MR. For each of these 9 positions of the phantom, an MR scan was performed using a gradient echo sequence for dynamic acquisitions with 1.2 *mm* isotropic spatial resolution and 0.515 *s* temporal resolution for a total volume acquisition (TR / TE 2.4 *ms* / 0.85 *ms* 20° flip angle). Spatial alignment of PET and MR co-ordinate systems was performed manually, with use of visual landmarks upon the phantom such as a 1 mm diameter glass rod, visible in both PET and MR. After acquisition, decay was taken into account and used to correct the intensity of each acquisition.

5.3.2 Motion correction

The motion estimation from the MR gates was performed with use of the hierarchical adaptive local affine registration toolkit, developed by Buerger et al. (2011). The methodology followed the motion estimation and lead to PET motion correction is described in Tsoumpas et al. (2013) with use of STIR library (version 2.2). Eight of the nine MR gates are registered to the reference gate and the resulting motion fields were used for motion correction of the PET images. The flow chart of actions required for motion correction is presented in figure 5.24. From this flow chart, some features are absent in this experiment. These are the spatial alignment and the temporal registration. In this experiment, the automatic synchronization hardware was not introduced and the synchronization was performed with synchronised initiation of the acquisition. Temporal registration will be analysed in detail in chapter 5.4.3.

5.3.3 Results

After reconstructing and registering PET and MR data, the fused image is visible in figure 5.12 in the reference position. Figure 5.13 provides visual representation of the phantom in extreme positions. The motion correction with RTA and MCIR provided the results shown in figure 5.14. The images provided are generated after 3 iterations of the OSEM. The 3 iterations were chosen as a standard stopping limit for typical clinical PET data.

As presented in table 5.1, in this case the most extended position of the phantom has been taken as the reference. The effect of motion and the effectiveness of the motion correction algorithm is quantified here by measuring the FWHM (full width at half maximum) and FWTM (full width at tenth maximum) of the radiotracer distribution in the direction of the highest motion amplitude. Both RTA and MCIR clearly recover the FWHM from the reduced value in the blurred image back to that of the reference image. The FWTM was also the same in the reference and corrected image, but it was not reduced in the blurred

image.

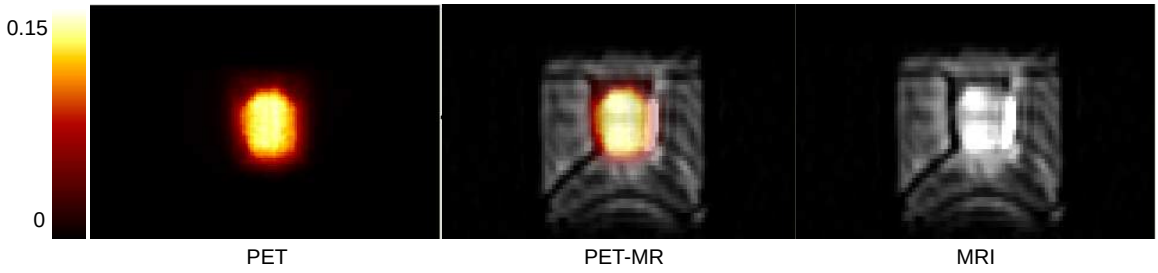

Fig. 5.12 Stop-and-shoot PET-MR acquisition at Gate 1. (Soultanidis et al. (2011), ©IEEE 2011)

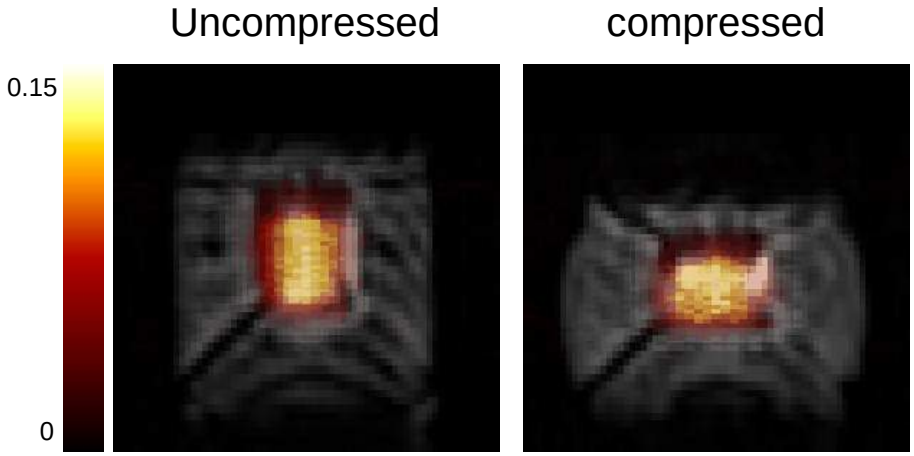

Fig. 5.13 PET-MR extremities

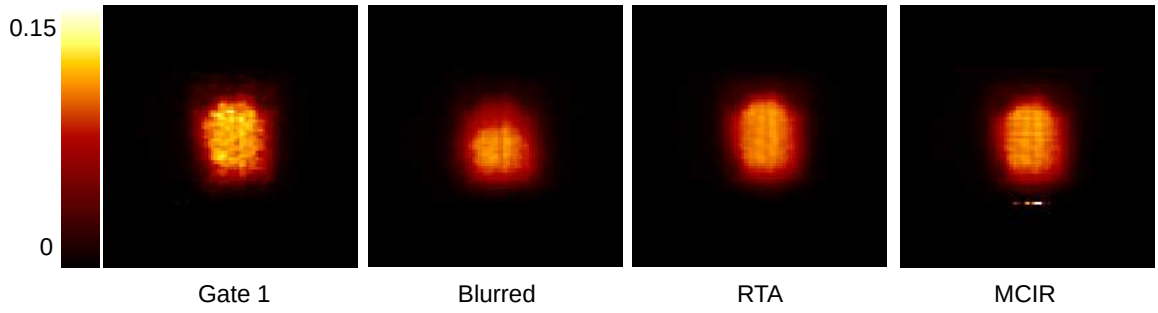

Fig. 5.14 Motion correction of stop-and-shoot PET data, with representation of a single gate (reference gate), the blurred by motion gate and the motion corrected PET with RTA and MCIR

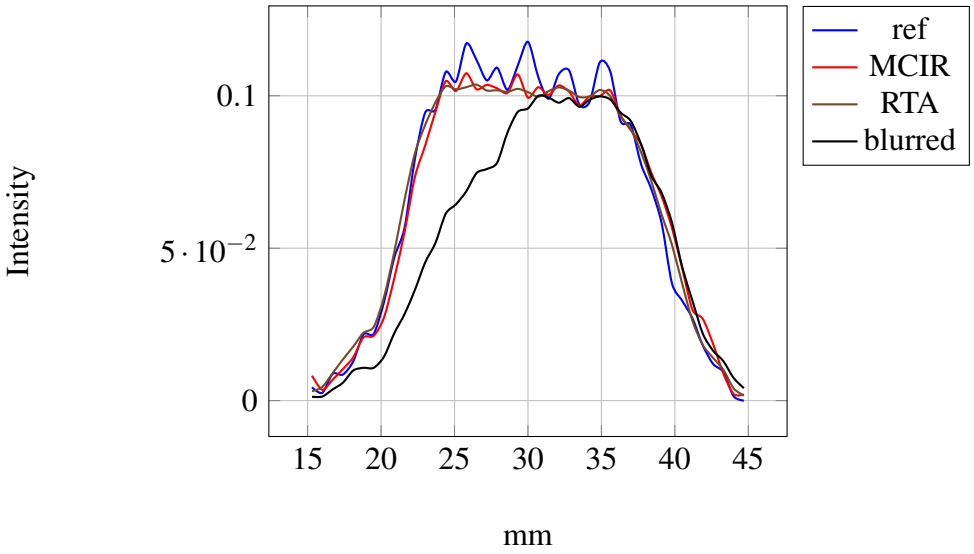

Fig. 5.15 line profiles for motion correction

Table 5.1 profile line FWHM and FWTM

	FWHM	FWTM
ref	18.2 *mm*	25.1 *mm*
blurred	16.7 *mm*	25.2 *mm*
RTA	18.2 *mm*	25.9 *mm*
MCIR	18.5 *mm*	25.1 *mm*

5.4 Second experiment: 3D PET-MR with continuous motion

The objective of this experiment is to perform simultaneous acquisition of a moving PET-MR phantom with both modalities and determine the the accuracy of motion correction in terms of image quality, quantification and creation of artefacts. The phantom selected for this experiment was the Polyvinyl Alcohol for its elastic properties and deformation abilities. The motor unit for this experiment is the PARKER servo motor, controlled by an Arduino MEGA for realistic and continuous transfer of motion. Finally, the scanner for this experiment is the HYPERimage scanner inside the Philips Achieva 3T MR.

5.4.1 Motion pattern

This real time continuous motion experiment has a variety of applied patterns. Whereas a sinusoidal motion can be created easily, real cases tend to have variations in repetition period and amplitude. Studies have been conducted of human respiratory motion patterns and the obtained information has been used as an input for these experiments. In particular, a study by Liu et al. (2007) investigates the common features of a human breathing pattern, during a PET scan. In order to investigate the effect of different displacement versus time profiles, the applied motion patterns are extracted from respiratory motion of human patient during PET acquisitions. These respiratory patterns are representative of three categories. The effects of each motion pattern and the effectiveness of motion correction upon these have been investigated on simulated datasets by Polycarpou et al. (2014). Figure 5.16 demonstrates three different motion patterns. The first motion pattern (*pattern A*) consists of 60% of the population and is characterized by long quiescent motion periods. The second motion pattern (*pattern B*) has regular quiescent motion periods and the third pattern (*pattern C*) has more random and baseline shifts (Polycarpou et al., 2014).

5.4.2 Spatial alignment

For an MR-compatible PET system that is not permanently integrated with in the MR scanner, the spatial alignment between the PET and MR may change slightly each time the PET insert is installed. The placement of the insert into the MR first determined by visual assessment. The centre of the PET insert field of view will not be always aligned with the centre of the MR field of view. Hence, for each experiment a new transformation matrix has to be created by a registration phantom. The process for acquiring registered data with a 3D PET insert is to use a registration phantom with no need for accurate placement of the PET inside the MR. After the registration phantom acquisition, the obtained transformation is applied to the experimental data. Therefore, the important components are a suitable phantom and

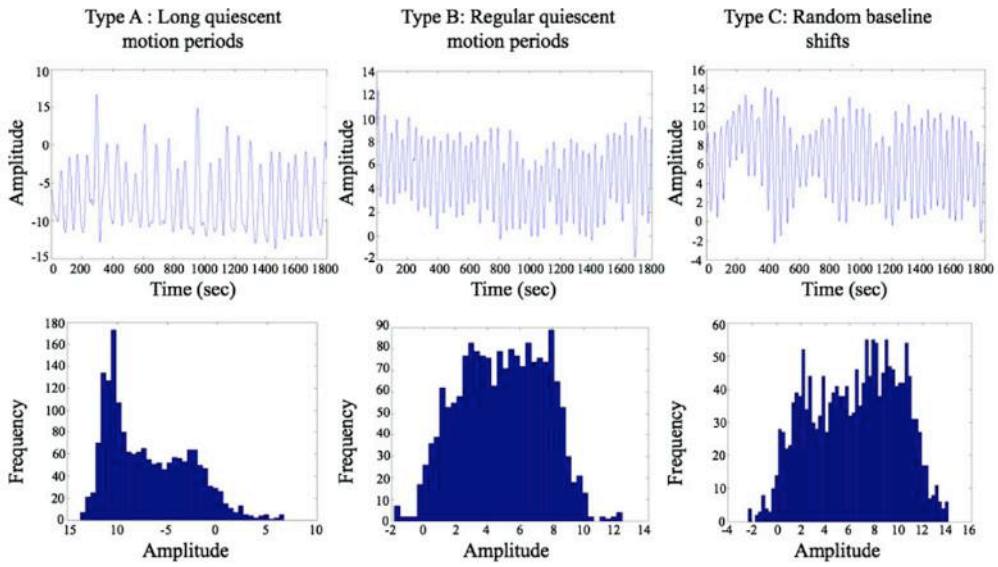

Fig. 5.16 Representation of breathing curves (top) and frequency plot (bottom) for (a) long quiescent motion periods, (b) regular quiescent motion periods and (c) for random baseline shifts (Polycarpou et al., 2014)

the registration methodology.

A phantom design for registration is presented in Chapter 2.4.1.2, where Ng et al. (2010) method is analysed. Each of these tubes is very fragile because of its small diameter and individual fill all of these tubes increase make the preparation very complex. For simplification, we connected the ends of each glass tube with rubber tubes. This method simplified the filling process, allowing every tube to be filled simultaneously and with a uniform concentration. With this concept and the use of a syringe mounting tube, spillage probabilities are minimized. The result is presented in Figure 5.17.

The straight glass tubes are made of glass with 1 *mm* inner diameter, and individual angles between each tube vary in order to give a non-repetitive pattern of cross-sections in PET and MR imaging. The phantom can be injected with radiotracer and MR contrast agent with total volume of 1 ml. The MR contrast agent is important for this scanner because the volume of liquid is very low and the coil incorporated into the HYPERimage insert (and which must be used for this alignment measurement) cannot collect a meaningful signal for

this small volume of water alone.

In the alignment procedure we have used here, the PET and MR fields of view, as defined by the co-ordinate systems in the PET and MR reconstructed images, have different origins and orientations relative to each other. The centre of the PET field of view is a fixed point defined by the detectors. The MR on the other hand can obtain a 3D volume wherever within the field of view as determined by the user. The offset of this centre is known during the MR acquisition. Furthermore, the orientation of image in MR is determined by the user for each acquisition. The MR user is free to acquire data with any orientation possible with axial, tangential or coronal slice selections. The PET and MR images may have a large distance between them and their views might be rotated. If a rigid registration algorithm is applied directly to this case, a mis-registration is possible to happen. The registration algorithm may rotate the images in a way that the registration would not provide any sensible result. With the help of the registration phantom, the first step is to align visually the PET image with the MR according to the centre of the field of view and the orientation. After the application of the first transformation, a second step is the registration of PET with MR by using rigid registration algorithm. With this registration phantom, mutual information is utilized for the registration between PET and MR. All the transformations are applied to the MR images. Every step described previously is performed with use of the IRTK software (Schnabel et al., 2001).

The two transformation steps are applied to each of the MR images. Additionally, because the centre of MR acquisition might have an offset comparing to the MR images of the registration, the difference is implemented to the MR image as an additional transformation.

5.4.3 Temporal synchronization of PET and MR acquisitions

Accurate temporal alignment of the acquisition from PET and MR is essential for MR-based PET motion correction. In the case of a PET insert, the modalities are operated indepen-

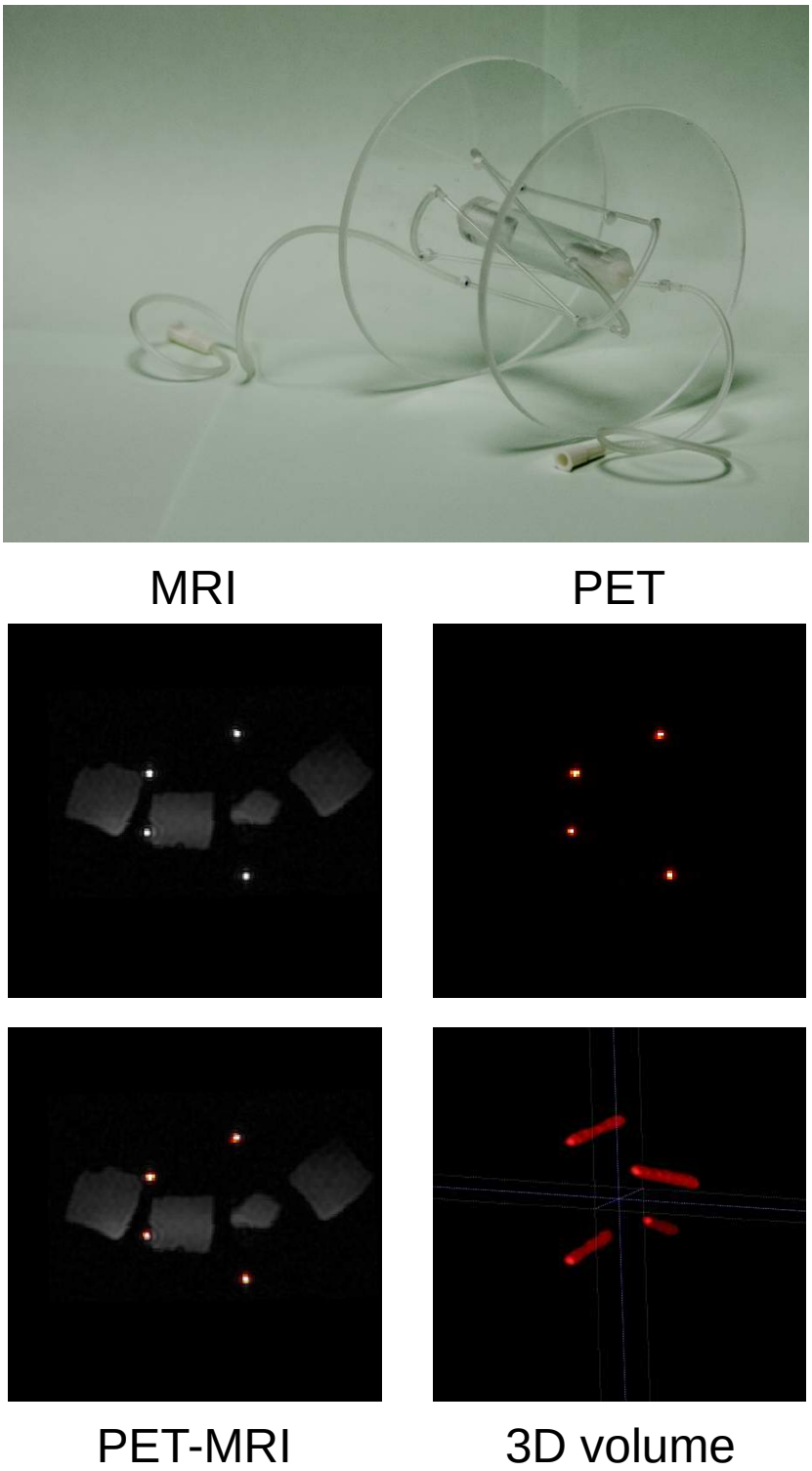

Fig. 5.17 Spatial alignment phantom and sample images. (Soultanidis et al. (2013b), ©IEEE 2013)

dently and are controlled by different computers. A communication protocol between the two modalities could share the timing information. The solution is to include the temporal information from one modality to the next. If the systems do not provide an electrical interface, the temporal information has to pass into the acquisition data stream that allows the independent PET and MR acquisitions to be synchronized (Weissler et al., 2015b).

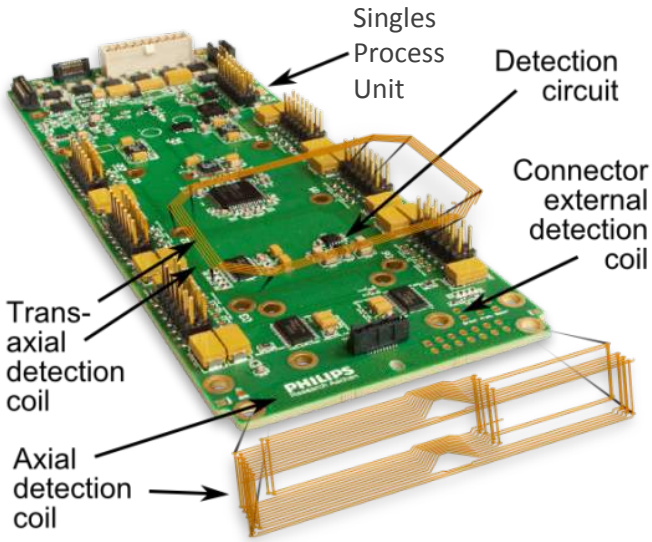

Fig. 5.18 PET module and detection coil. Exploded view with the details of the coil. (Weissler et al. (2015b), ©IEEE 2015)

Each module of the HYPERimage scanner has a detection coil for gradient variations. When the variation of the MR gradient field reaches a threshold, a trigger pulse is stored by the PET insert with a time-stamp telling the exact time the gradient change occurred. By acquiring this information, we have the capability to allocate the gradient change and correlate the PET time-stamp. Figure 5.19 demonstrates the correlation between a standard gradient echo sequence and the outcome, as captured by the gradient sensors inside the PET insert.

The experiment performed here has a specific complication. The MR protocol cannot capture more than 300 dynamic images per acquisition, because of hardware safety reasons.

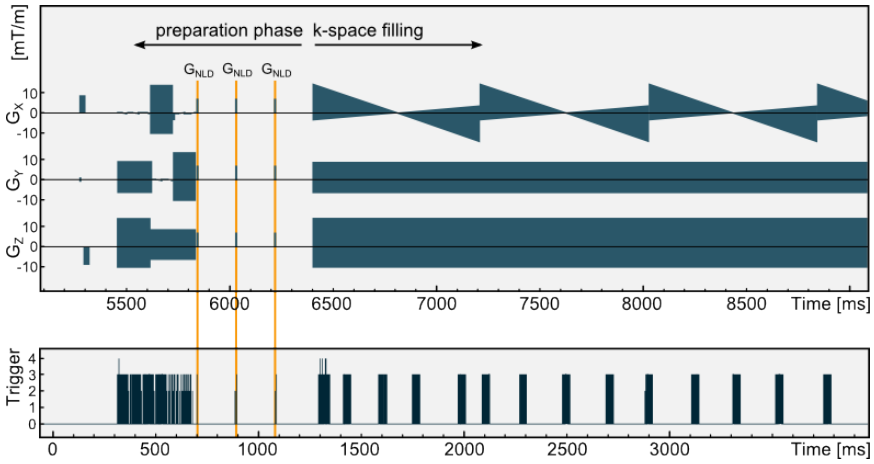

Fig. 5.19 Detail of sequence diagram (top) from a standard gradient echo survey sequence and corresponding data of the gradient detection circuit from one SPU (bottom)

Given the fact that each dynamic frame lasts for 0.515 *s*, each acquisition can last a maximum of 154.5 *s* (almost 3 min). Therefore, multiple acquisitions for each experiment have to be performed for a sufficient experiment. In the MR, none of the existing file formats, dicom or PARREC, has the possibility of storing the time stamps accurately. This is solved by synchronizing each MR acquisition individually with the PET acquisition. As figure 5.20 describes, with a continuous PET scan, multiple MR scans can be initialized in parallel with a limiting factor being the gradient capture at the beginning of each acquisition. We switch on the gradient sensor for 10 *s* and during this time period we start the MR. The first gradient change of this acquisition corresponds to the beginning of a new dynamic acquisition. The use of a 10 *s* time window for the gradient sensors serves another purpose. The firmware of the scanner provides higher priority to sensor measurements than the actual photon acquisitions. With the gradient sensor active, 50 % of the PET events are not transmitted.

The validation of synchronization is obtained from the comparison of the PET and MR motion information. Where as the MR provides motion information through an image analysis procedure (Schleyer et al., 2013), PET provides motion information through the total

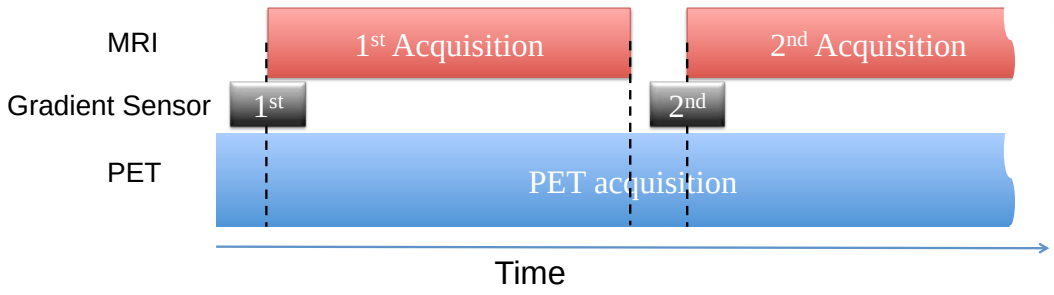

Fig. 5.20 Protocol for synchronizing PET and MR acquisition — the sensor in the PET scanner that detects the MR gradient is only switched on at the start of each simultaneous acquisition

number of counts per frame. For each MR frame, the motion amplitude was calculated with a cross-correlation technique (Sachs et al., 1994). For the corresponding PET frame, the total number of coincidences was obtained from the listmode file. Figure 5.21 demonstrates the motion, as captured by MR and PET. The amplitude alignment is not so important as the temporal alignment of local minima. Even no viable analysis can be produced reliably by this plot, for these 50 second it ha been found that the local minima of PET and MR derived signal had maximum difference of 1.03 *s*.

The immediate correlation of motion amplitude and number of counts is presented in Figure 5.22. The trendline upon the plot is a 4^{th} degree polynomial equation, where the coefficient of determination R^2 is the highest at 0.534. This value is not high enough for several reasons. Initially, it can be observed that the increase of counts does not follow the increase of displacement above 6 mm. Additionally, PET data are scattered and any correlation of them becomes difficult. Therefore, this method fails to provide a rigorous validation of synchronization between PET and MR because of the high noise levels in PET data and data behaviour. However, an interesting observation illustrated in Figure 5.21 is the relatively good correlation between motion signals that could be extracted from the counts and the motion amplitude. However, PET datasets are very noisy in order to deduce a correlation coefficient, thus this observation requires additional experimental evidence

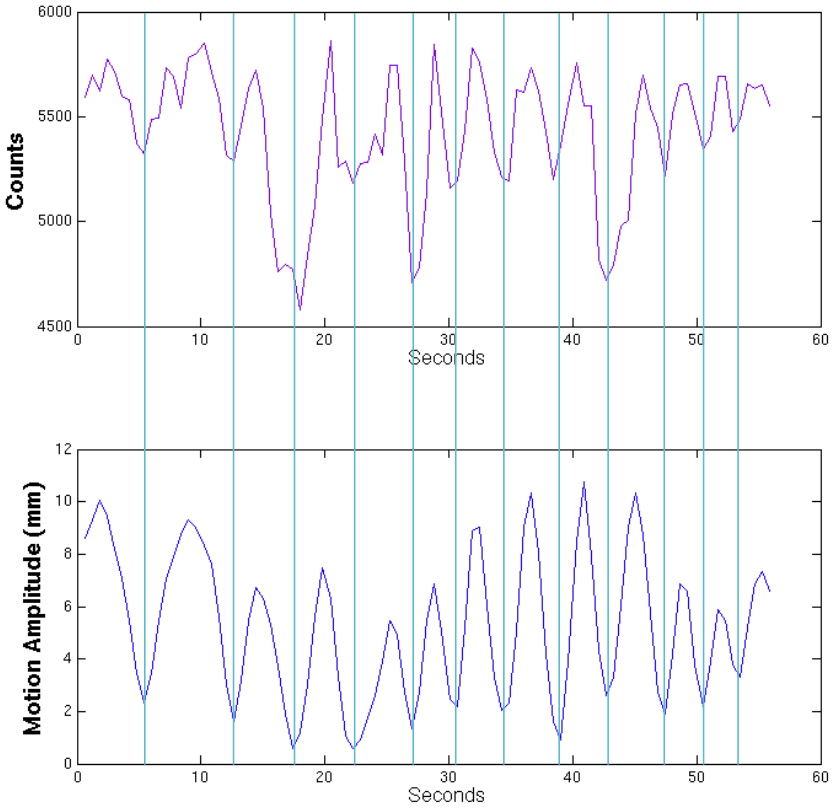

Fig. 5.21 Motion amplitude as it is captured by PET (top) and MR (bottom)

before any conclusions are drawn. A potential cause of this result may be the scanner's sensitivity. This scanner, as described by Mackewn et al. (2015) has a sensitivity of 0.6% in the centre of the scanner. This sensitivity drops more than 50% for every cm outside the centre. Therefore, the cause might be that the higher concentration volumes crossed the areas with the highest sensitivity at 6 mm of displacement and moved towards lower sensitivity areas.

This method cannot give an absolute validation of synchronization between PET and MR because of the high noise levels but it is clear that the correlation between the motion signals, captured with PET and MR is very good.

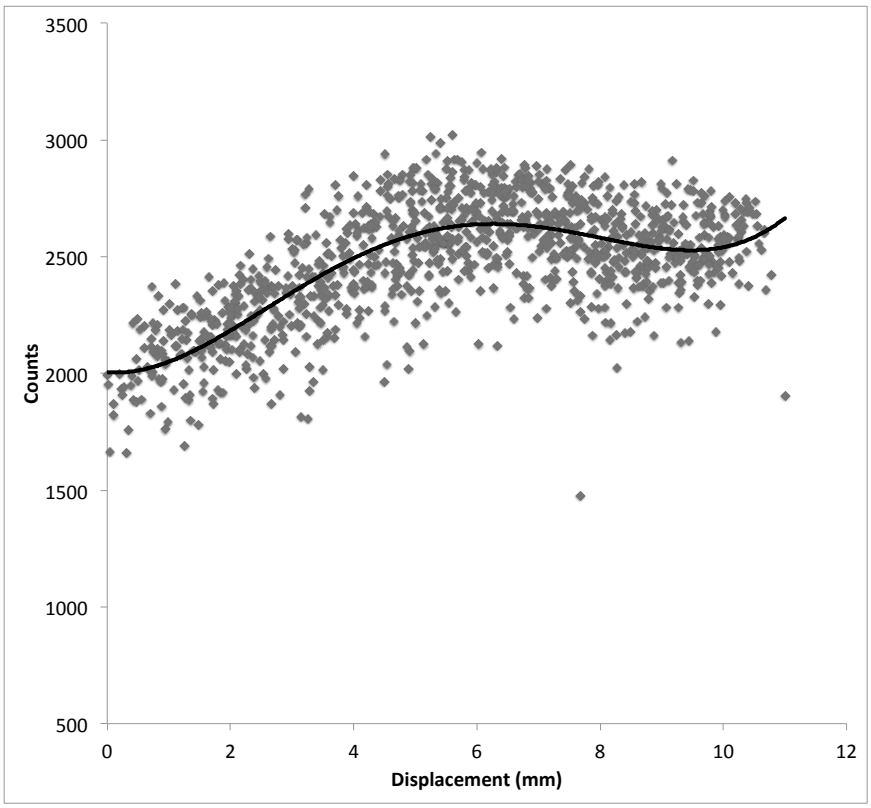

Fig. 5.22 Scatter plot of motion amplitude against number of counts per time frame.

5.4.4 PET and MR acquisition

The PET insert used for this experiment is the HYPERimage. The MR images were captured with the use of the Philips Achieva 3T scanner and a two-channel, transmit-receive coil. The motion measurement was based upon dynamic 3D images. The phantom was scanned with temporal resolution of 0.601 *s* for a total volume acquisition, matrix size $240 \times 240 \times 162$ and spatial resolution of $0.81 \times 0.81 \times 1.2$ in *mm* (TR / TE 2.4 *ms* / 0.85 *ms*, 20° flip angle). This sequence was repeated for 1200 times (721.2 *s* total).

5.4.5 Gating of MR and PET Data

The first acquired gradient trigger signifies the beginning of the MR dynamic acquisitions. Once the synchronization time stamp is known, the PET data are divided according to the

corresponding MR frames. With the duration of each frame stable and known, the time interval for each PET frame is calculated and the corresponding events are sorted into their corresponding frame. With this step, synchronized PET and MR images can be assigned to gates. For this experiment, the data were divided into 8 different gates using amplitude gating. The assignment to gates was performed by a pencil beam navigator, with motion amplitude determined from the MR images. Theoretically, any one-dimensional array inside a 3D image can serve as a pencil beam navigator, with no special acquisition. The pencil beam navigator is placed parallel to the central motion plane for maximum displacement per gate. The pencil beam navigator is extracted for each MR frame from the centre of the phantom and the amplitude of motion is calculated with a cross-correlation algorithm against a reference frame with the use of Matlab.

After taking into account the motion amplitude any MR images and the corresponding PET sinograms were divided into eight different gates. Finally, we acquired the average MR image and the total PET sinogram for each gate.

As additional information, for each MR gate, an attenuation image was created to be used for attenuation correction. The attenuation coefficient of the PVA is known from previous studies and the phantom mask is created by applying a threshold to the MR images. Within Matlab, knowing the shape of the original phantom, we measured the smallest MR intensity value in a static MR image of the phantom and set this value to be threshold to discriminate between the phantom and background. The phantom was assigned a value of 1, where the background had value equal to 0. The phantom was multiplied with the value of the attenuation coefficient for PVA, given the Table 3.7. Figure 5.23 shows an example of the segmented MR image.

Fig. 5.23 An example of image segmentation for extraction of attenuation coefficient volume.

5.4.6 Motion Correction

The motion estimation from of MR gates and subsequent PET motion correction is performed with use of the hierarchical adaptive local affine registration toolkit, developed by Buerger et al. (2011) and STIR library. Seven of the eight MR gates are registered to the reference gate and the produced motion fields were used for motion correction of the PET images. The flow chart of actions required for motion correction are presented in figure 5.24, starting from the phantom and finishing at the reconstruction and correction methodologies.

The motion correction of PET data was performed with two methods. The first is called Reconstruct-Transform-Average (RTA) and the second is called Motion Compensated Image Reconstruction (MCIR). For motion correction with RTA the images are individually reconstructed and the motion correction is applied to the images which are then averaged. In MCIR the motion correction procedure is integrated with the reconstruction, therefore the correction is applied directly to the sinograms. The relative benefits of each motion correction technique are described in a recent study by Polycarpou et al. (2012). The reconstruction of the PET data has been performed with use of the open source STIR library, release 2.4 which includes both RTA and MCIR as developed by Tsoumpas et al. (2013). The reconstruction algorithm used for this study is the OSEM (7 subsets, 5 iterations) with the scanner normalization and the attenuation correction included (Soultanidis et al., 2013b).

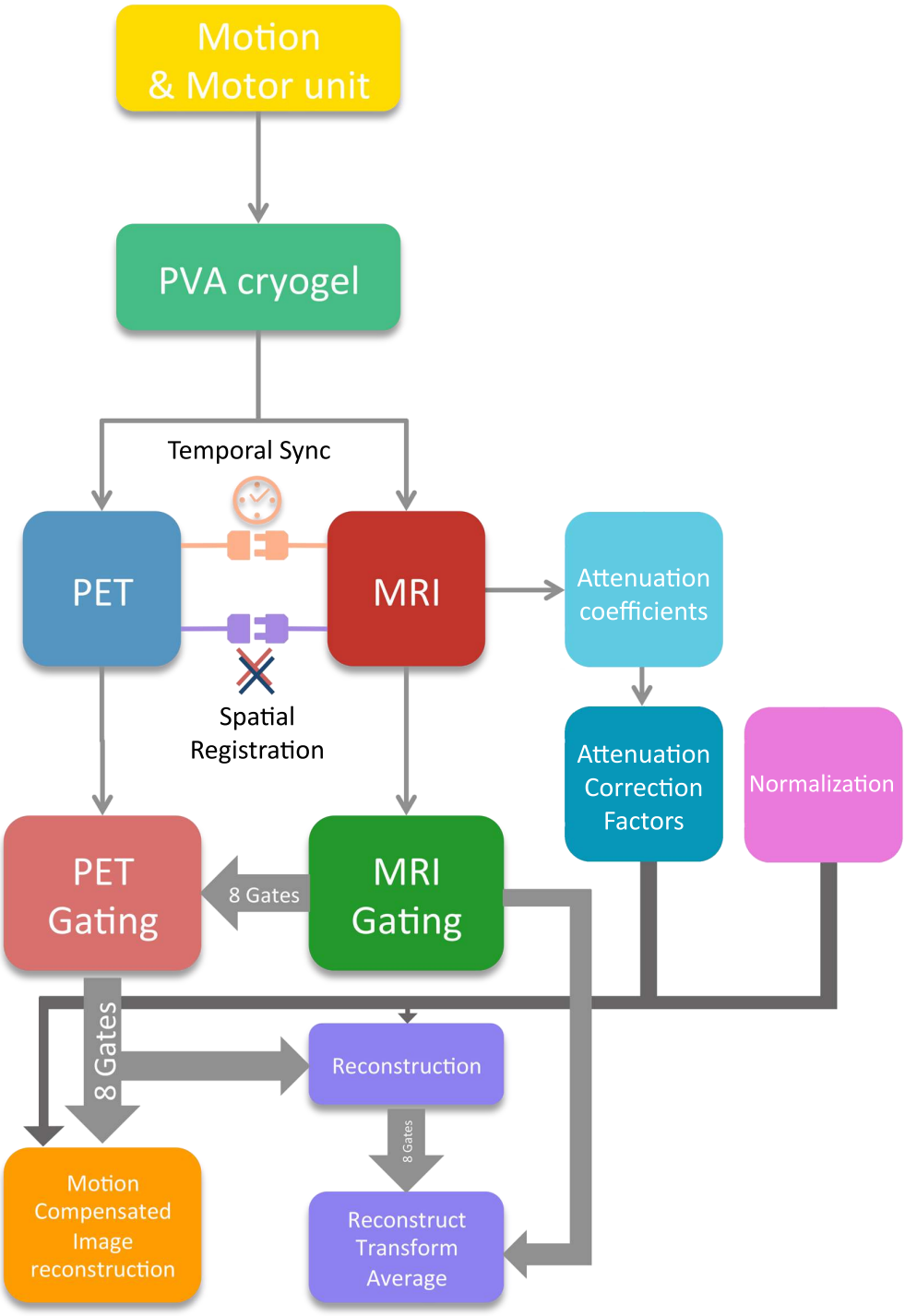

Fig. 5.24 Motion correction work flow for simultaneous PET and MR data with RTA and MCIR

Table 5.2 Statistics of static PET acquisition

	mean intensity within ROI	Standard deviation	Standard error	Volume (cm^3)
Static	1.931	0.436	0.005	0.237

5.4.7 Results

The motion reproduced inside the PET-MR system was not equally distributed between the 8 gates. Figure 5.25 shows the frequency of occurrence of each gate, for each of the three motion patterns, as obtained from the MR measurements. These reflect the expected programmed motion patterns.

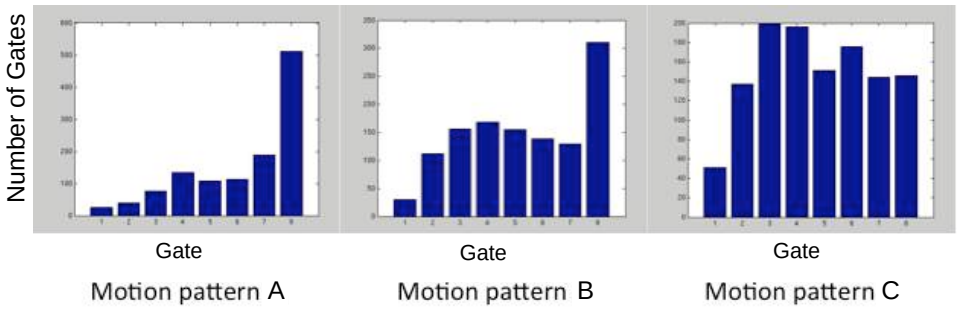

Fig. 5.25 Motion estimation with use of MR data

As can be seen in figure 5.28 the 7 mm object is visible in the phantom, but the 5 and 3 mm objects are not visible. This may be attributed to the phantom production procedure, but also in part is due to the poor SNR in these images, as obtained from the HYPERimage scanner. The PET images were reconstructed and presented after 3 iterations. This number of iterations is common within clinical practice as a stopping point.

Figure 5.26 gives the long acquisition of a static phantom in PET and the line profile in the centre of the hot lesion. Table 5.2 provide the statistical information about this long acquisition.

Figures 5.28, 5.30 and 5.32 demonstrate the effect of motion for each motion pattern and the motion correction of it. Also, for each method, a line profile has been drawn through

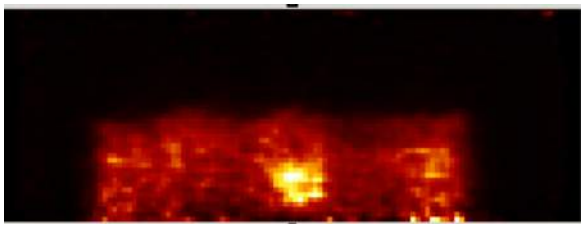

Fig. 5.26 Static PET acquisition

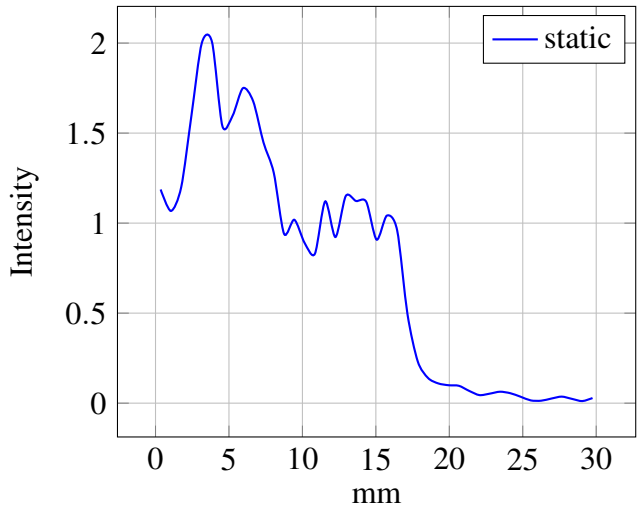

Fig. 5.27 Motion Pattern A (long quiescent period)

the centre of the hot lesion and intensity statistics have been extracted with use of PMOD analysis software (version 3.4) [1]. For each image acquired and processed, a volumetric analysis was performed, where the hot lesion was segmented with the use of PMOD. This software gave the opportunity to segment the PET images into volumes by threshold, which was set at 50% of the maximum value inside the volume. From this volumetric analysis, we had the opportunity to get the mean value of the intensity, standard deviation and standard error.

5.4.7.1 Correlation coefficients

A statistical method to calculate the effectiveness of motion correction is to correlate the obtained images with a motionless acquisition. This can be performed with use of the

[1] PMOD has been developed by PMOD Technologies Ltd. www.pmod.com

Table 5.3 Statistics of hot area in Motion Pattern A (long quiescent period)

	mean intensity within ROI	Standard deviation	Standard error	Volume (cm^3)
Static	1.931	0.436	0.005	0.237
Blurred	1.048	0.157	0.001	0.610
RTA	1.478	0.199	0.003	0.147
MCIR	1.232	0.175	0.02	0.196

Table 5.4 Statistics of hot area in Motion Pattern B (regular quiescent period)

	mean intensity within ROI	Standard deviation	Standard error	Volume (cm^3)
Static	1.931	0.436	0.005	0.237
Blurred	1.171	0.163	0.001	0.510
RTA	1.236	0.191	0.002	0.191
MCIR	1.219	0.188	0.002	0.214

Table 5.5 Statistics of hot area in Motion Pattern C (random with base shifts)

	mean intensity within ROI	Standard deviation	Standard error	Volume (cm^3)
Static	1.931	0.436	0.005	0.237
Blurred	1.070	0.152	0.001	0.624
RTA	1.146	0.174	0.001	0.383
MCIR	1.180	0.181	0.062	0.285

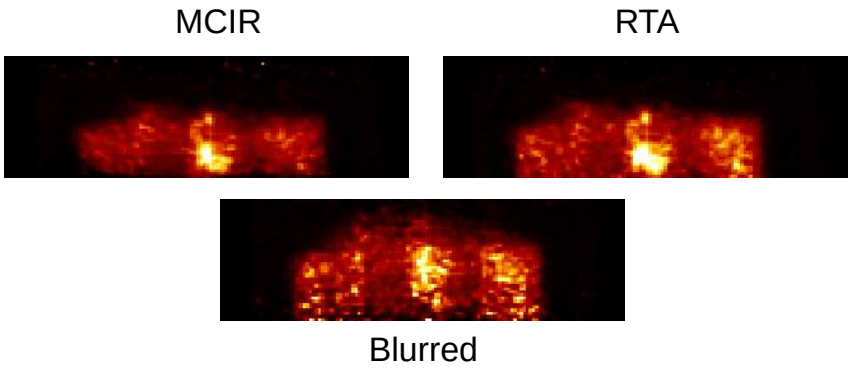

Fig. 5.28 Motion correction of motion Pattern A (long quiescent period)

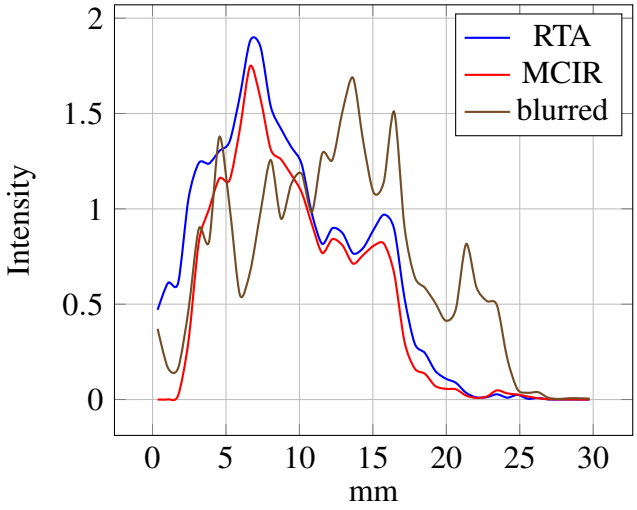

Fig. 5.29 Motion Pattern A (long quiescent period)

line profiles above and the correlation coefficient of each pairing. This coefficient can be calculated by the following equation.

$$Correlation\ coefficient = \frac{\sum_{i=1}^{n}(x_i-\bar{x})(y_i-\bar{y})}{\sqrt{\sum_{i=1}^{n}(x_i-\bar{x}_i)^2}\sqrt{\sum_{i=1}^{n}(y_i-\bar{y}_i)^2}} \tag{5.1}$$

In this equation, X and Y are the line profiles under comparison and n is the size of the line profile array. Correlation coefficient indicates the similarity of one-dimensional arrays under comparison. The output varies from -1 to 1 where 1 is perfect correlation, -1 a perfect negative correlation and 0 indicates no correlation. Therefore, a comparison of all

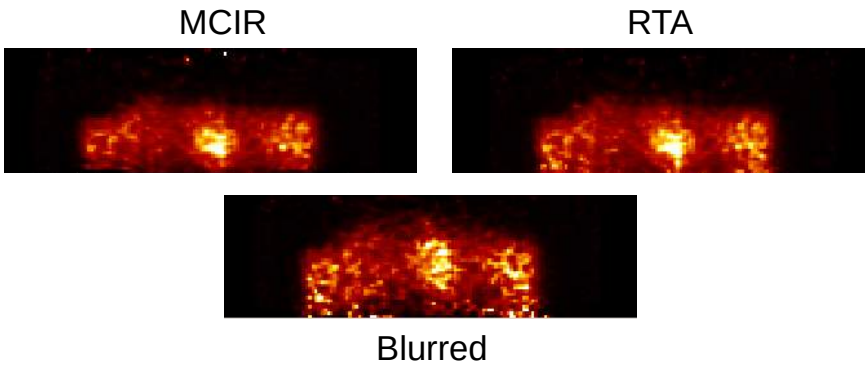

Fig. 5.30 Motion correction of motion Pattern B (regular quiescent period)

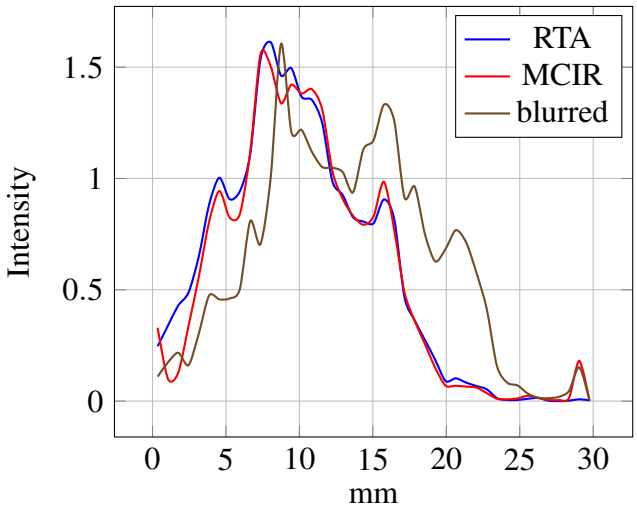

Fig. 5.31 Motion Pattern B (regular quiescent period)

line profiles with the static acquisition indicates the success of the correction.

Figure 5.34 provides the success rate of motion correction, as it is derived by the line profiles, compared with the static acquisition.

5.5 Discussion

In both experiments above, the use of PVA cryogel proven easy to use in creating a new non-rigid 3D phantom for evaluation motion correction.

For the first experiment, motion effects upon the PET image are visible on the upper

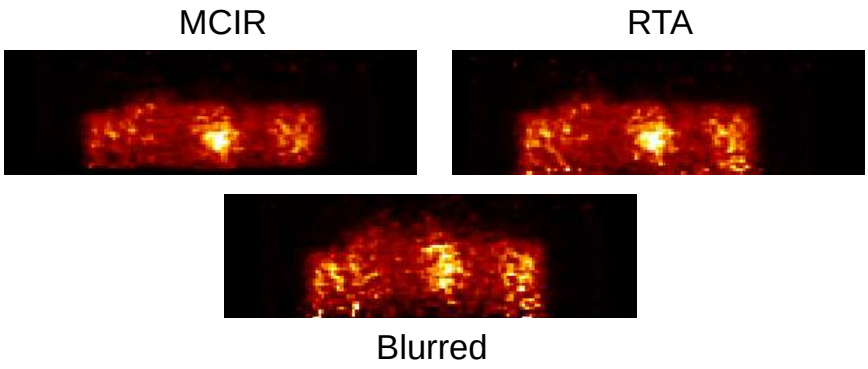

Fig. 5.32 Motion correction of motion Pattern C (random with base shifts)

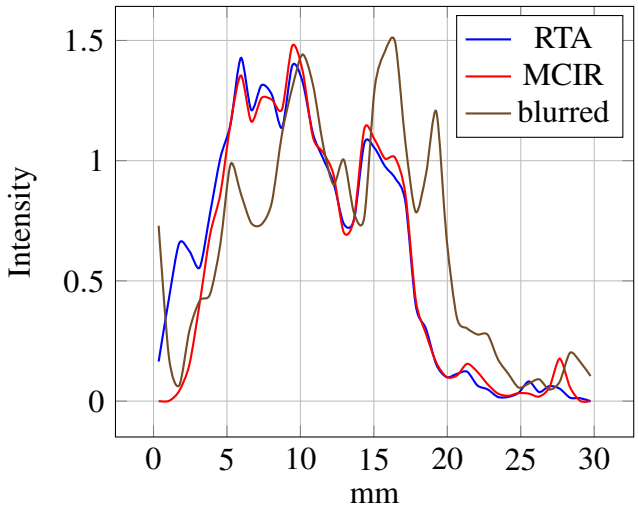

Fig. 5.33 Motion Pattern C (random with base shifts)

edge of the phantom, where the motion amplitude is high. The way this phantom moves differs from any rigid phantom in that the motion amplitude is not homogeneous in the entire phantom. Where the top part has bigger motion amplitude, the base moves slower. This is also the reason why the line profile, of the blurred image, even if is reduced in one edge, it gains full amplitude between 30-35 mm. As Table 5.1 indicates, motion correction provides recovery of FWHM with both RTA and MCIR (Figure 5.15). By comparing the corrected images with the reference gate 1, there is sufficient recovery of the PET signal intensity and furthermore lower noise is visible due to higher acquisition statistics.Whilst the image of *gate 1* alone is very noisy, the images at the full dataset appear to have good

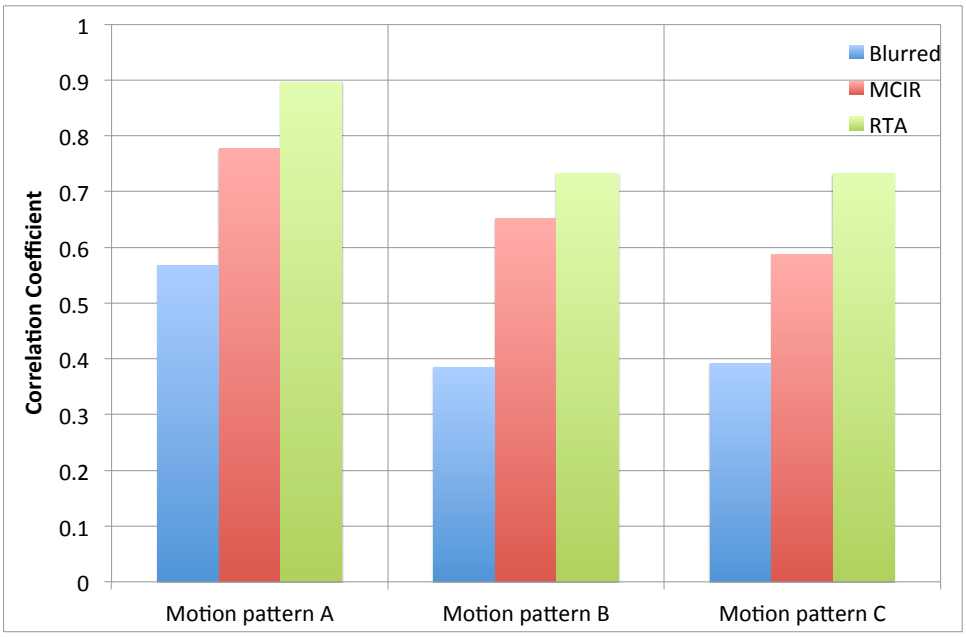

Fig. 5.34 Correlation coefficient of blurred, MCIR and RTA line profiles for three motion patterns (A, B, and C)

quality with only small alterations (some vertical streaks).

Even if the motion correction is sufficient and we have recovery of the data, it has to be emphasized that this experiment has stop-and-shoot format. With intra-frame motion absent and equal distribution of counts per gate, this acquisition is not realistic (also acquisition times were long and at low count rates). Furthermore, the absence of background activity generates a high contrast object, with few similarities to an in vivo scan. Nevertheless, his experiment gave valid information about the capabilities of PET and MR scanners. Furthermore, it was a test of the local affine registration algorithm that was used with PVA cryogel phantom, to obtain the motion fields. The lack of spatial registration and temporal synchronization were significant obstacles in this experiment. This realization was the reason to get further actions towards a hardware solution for temporal synchronization, and such a method was then implemented by our colleagues in the Sublima project (Weissler et al., 2014).

The points above were addressed with the second experiment. Motion correction with

continuous motion created the need to adapt the hardware and overcome various technical challenges, in order to perform the experiment continuously with real time motion. Also, the resolution of temporal synchronization without the need to connect both modalities physically, made true synchronized simultaneous acquisition possible.

The increase of the complexity brought new challenges to the motion correction. After establishing the use of PVA cryogel with the first experiment, the signal to background ratio increased the realism of this phantom experiment. Because of this and the unsuccessful moulding of the spheres, the 3 mm and the 5 mm spheres were not visible in images with all 3 motion patterns (although this may also be due to the poor SNR). The 7 mm sphere, even if visible, has non-spherical shape. The comparison of the recovery percentage though can reveal the success of the motion correction. In each case, the corrected images with both RTA and MCIR are visibly improved over the blurred image, though difficult to see motion pattern differences.

Due to the small FOV, the static image is very noisy. The process to extract the values is similar with the process described above; a 50 % threshold was applied to the area of the hot lesion and segmentation was performed. This gave a standard deviation of the hot area at 0.436 and standard error at 0.005 as presented in Table 5.2 due to large sample size. It is seen that we cannot get a meaningful standard error by this experiment, but the trend is that motion reduces the mean intensity and both correction methods recover it to some extent.

All corrected images show improved recovery to the blurred images. In all patterns though, as is presented by quantitative analysis there is not full recovery of the mean intensity, in comparison with the static. In all the cases, when the image is blurred, the average volume of the "hot" area is bigger as it would be expected. Literature explains this aspect as the effect of volume over-estimation due to motion. With motion correction, the volume is reduced to the value in the reference static scan. From the correlation coefficient point of view, the data do not show full recovery but the results are all improved to at least a small

extent. As it was expected by literature, the recovery is worst in motion patterns B and C. Literature indicates that MCIR, has better responce that RTA (Polycarpou et al., 2012), something that does not correspond to this experimental setup. This may be explained by the fact that with the limited 3 cm axial field of view the phantom is not entirely inside the field of view. For that reason, there might be a loss of data, due to migration of counts outside of the field of view.

It has to be noted that due to the nature of the scanner, and the small axial field of view, noise and reconstruction artefacts are concentrated at the edges of the FOV. This noise, contributes to the uncertainty during data processing. As the scanner resolution is 1.6 *mm* it is affected by partial volume effect and motion amplitude. With maximum motion amplitude at 10 *mm* the motion is visible in PET images. Furthermore, the hot area is 4 times bigger than the resolution. For these reasons the overall image quality is disappointing. So in the next chapter we describe similar experiments performed on a next generation scanner with much improved specifications.

5.6 Conclusions

This chapter has demonstrated the upgrade of motion correction complexity from simple 2D acquisitions to 3D with a SiPM PET insert. Even if the motion correction has to face stop-and-shoot data or data with continuous motion, the results show partial recovery of uptake amplitude and volume inside the hot areas. Additionally, correlation coefficient demonstrates a limited recovery of information through motion correction to the entire phantom, despite that the overall image quality is poor for both motion correction methods and for all motion patterns, to different amounts.

Chapter 6

Motion correction for 3D PET-MR with high sensitivity and resolution

6.1 Introduction

Motion correction has to be applicable to any new PET-MR system available. Therefore, the knowledge gathered by the previous experiments can be used into the next generation of PET-MR systems. The further development of HYPERimage, an analogue SiPM PET insert is the digital SiPM, Hyperion-II^D. The higher resolution and sensitivity provided by this system, indicates that motion correction is necessary, even if the motion does not have high amplitude. The new hardware, with its improvements and alterations from the predecessor brings solutions but also additional challenges to the experimental setup.

6.2 Materials and Methods

6.2.1 Scanner

This PET insert is designed to be compatible with a Philips Achieva 3T MR. The use of digital SiPMs in the Hyperion-II^D system, brings some benefits to PET-insert design. The first advantage is the smaller packaging.

Because the analogue to digital conversion board is not necessary, valuable space is saved alowing a more compact packing. As an intermediate digitizer, with its associated high power consumption, is not necessary in this design, it is possible to keep the temperature more stable compared to the previous system (Duppenbecker et al., 2012).

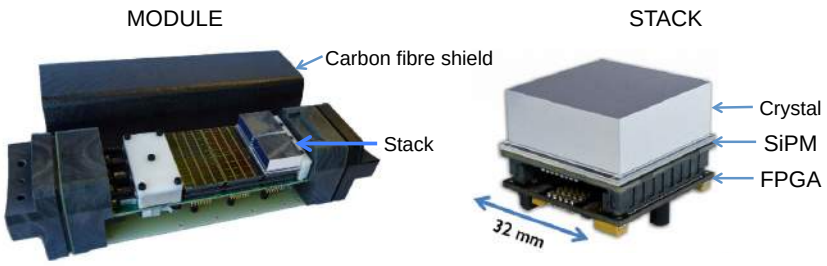

Fig. 6.1 Stack and module with use of Digital SiPM. (Duppenbecker et al. (2012), ©IEEE 2012)

These digital SiPMs are used to create a PET insert. Figure 6.1 presents the building blocks of the insert. The digital detectors(Philips Digital Photon Counting DLS 3200-22, 64 sensors, 3200 cells each) are coupled with a 30×30 LYSO crystal array (1 mm pitch, 12 mm length) and a custom made FPGA tile (Schug et al., 2014). The stacks are grouped in clusters of 6, arranged into a 2×3 grid, creating the module. 10 modules form the PET scanner with 216 mm transverse field of view and 96 mm axial field of view. The electronic parts are cooled with liquid and air cooling. Compressed air of 1 bar higher than the atmospheric pressure flows around the electronics and the stacks are cooled down with continuous flow of cooling liquid at 5 ° C (Weissler et al., 2012)(1 bar is the pressure

within the scanner). The data communication with the processing server outside the MR examination room is performed with plastic optic fibres. The housing of the module is a carbon fibre screen. This shielding shows good RF shielding, it's almost transparent to gradients (B_0 magnetic field reduction is at 0.2 ppm and maximum SNR reduction is at 13 %) and it has low attenuation of gamma radiation (Wehner et al., 2014; Weissler et al., 2015a). As with HYPERimage, the components of the insert inside the MR room include, in addition to the PET itself, the embedded power unit, providing individual power to each SPU. The long optic fibres lead the signal outside the MR room to the control room, where no magnetic interference is present. Also, outside the MR room is the water cooling system and the data acquisition computer. The air cooling is provided by the hospital supply, inside the MR room. Hyperion-II^D comes with a 12 rod bird-cage mouse Tx/Rx coil with inner diameter of 46 mm (Weissler et al., 2012). Hyperion-II^D is presented as a stand alone system in figure 6.2. In figure 6.3, the insert is in inside the MR room.

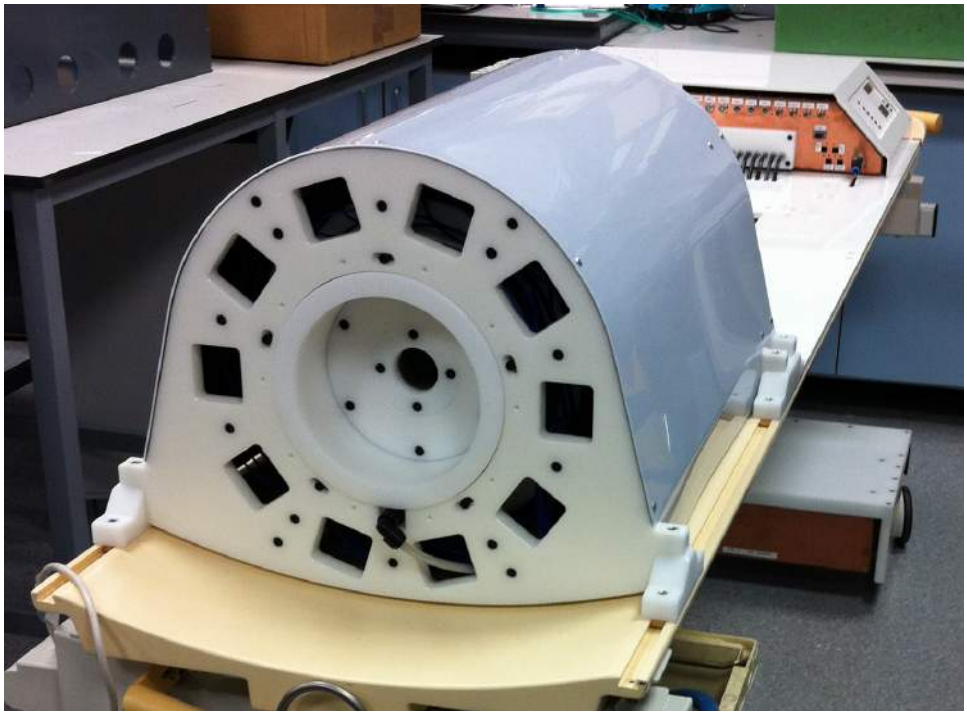

Fig. 6.2 Hyperion-II^D PET insert

Fig. 6.3 Hyperion-II^D PET insert with the Philips Achieva 3 Tesla MR scanner

The data readout methodology, is similar with HYPERimage insert with the data stored as single events and post-processed by generating a listmode file. This listmode file is encoded with information about the crystal/stack and module that a pair of events took place. A difference with HYPERimage insert is the amount of bits dedicated for the timing information, by increasing the 32 bits to 64. Therefore, each event consumes 20 bytes of space. The use of an official Philips MR table as the base improves the versatility of the system and ensures that the PET module is placed in the centre of the magnetic field.

6.2.2 Phantom

Use of PVA cryogel for this experiment is a good solution to simulate and capture motion during simultaneous PET-MR acquisition. The first obstacle to surpass is the size. The RF coil of the insert has 46 mm maximum diameter, but the minimum diameter is at 40 mm, at the entry of the gantry. There is a need then for a phantom, to be less than 40 mm diameter, and deformable. So, a scaled down cylindrical phantom was used. The new phantom has

a diameter of 30 mm and height of 40 mm. Inside the phantom, a hot spherical area is placed with a diameter of 8 mm and lesion to background ration of 4:1. Total activity of the phantom at the beginning of the experiment was 1.4 MBq. The method of preparation follows the steps described in chapter 3, with a few alterations as follows. The sphere is frozen at -80 ° C for 3 hours, then it was fixed inside the liquid PVA, which serves as the background and frozen for an additional 3 hours. Then it was removed by freezer to thaw for 3 hours. The phantom design is presented in figure 6.4.

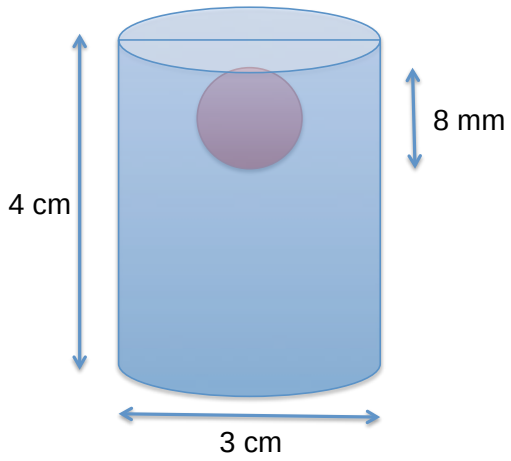

Fig. 6.4 Cryogel phantom with dimensions dedicated for the Hyperion-II^D PET insert

6.2.3 Synchronization and spatial alignment

This PET insert has similar hardware to the HYPERimage scanner. For that reason, there is no difference in the synchronization methodology between the two systems. At the beginning of each MR acquisition, the gradient sensors, attached to the PET modules, capture and store the time stamp of the first gradient change. This time stamp, is then used to split the PET data to temporal frames, synchronised with the MR acquisition.

The registration as well is performed with similar method. Even though, for this experiment, a new phantom with smaller diameter had to be designed.

6.2.4 Motion pattern

Following the motion patterns of the previous experiments, this time we concentrate upon just the most common motion pattern, which represents 60% of the population and is characterized by long quiescent motion periods. As with the previous experiment, for reproduction of continuous motion, a servo motor was utilized. The experimental set-up includes a Parker servo motor (N series, 3 Amp. current, VAC) driven by a Parker Gemini GV servo driver. By providing one digital pulse to the servo driver, the motor moves for one step. A data stream of pulses can generate continuous motion of the motor. The motion signal is given by an Arduino MEGA 2560 (D'ausilio, 2012). Arduino is a USB based hardware I/O unit with digital and analogue interface capabilities. It is programmable and can perform autonomous tasks, without continuous connection with a computer. Here, the Arduino was programmed to receive via USB the target position and calculate speed, number of iterations and execute the data transmission to the servo driver. More specifically; Arduino receives a 4 bytes integer number every 0.1 s. This number is the target position for the servo motor. By already knowing the origin and the destination point, the Arduino calculates the number of necessary steps or revolutions, as known to servo motors, and divides the number with the time interval of 0.1 s in order to find the period of each step. The orientation of rotation is calculated also by subtracting the origin and destination position. Finally, the Arduino transmits the step action signal, along with the orientation of rotation. The 4 byte coordinates were finally transmitted to the Arduino by a home-made Java script in a computer via USB. These coordinates are given by a pre-produced waveform, depending on the experiment needs. The signal transfer was repeated every 0.1 s. This set-up can reproduce any custom motion patterns with time interval of 0.1 s per step. Of course, this time interval may change, depending the requirements.

6.2.5 MR acquisition

The MR acquisition was performed with use of the mouse coil. For the motion estimation in total 5 dynamic acquisitions of 300 frames each was acquired. The MR acquisition for *phantom A* is a gradient echo with temporal resolution of 0.479 *s*, matrix size $80 \times 80 \times 45$ and spatial resolution of $0.625 \times 0.625 \times 1.0$ in *mm* (TR / TE 2.4 *ms* / 0.85 *ms*, 20° flip angle). This sequence was repeated for 1500 times (718.5 *s* total).

6.2.6 Gating of MR and PET Data

After synchronization and spatial alignment, PET and MR images can be assigned to gates. For this experiment, amplitude gating was used. The data were divided into 8 different gates, using amplitude gating. The assignment to gates was performed by pencil beam navigator, where motion amplitude is determined from the MR images. The pencil beam navigator is placed parallel to the central motion for maximum displacement per gate. The pencil beam navigator is extracted for each MR frame from the centre of the phantom and the amplitude of motion is calculated with a cross-correlation algorithm against a reference frame with use of Matlab.

After taking into account the motion amplitude, MR images and the corresponding PET sinograms were divided into eight different gates. Finally, we acquired the average MR image and the total PET sinogram for each gate.

6.2.7 Static scan

For comparison reasons, a long PET scan was performed, where during this period, the phantom was not moving. To compensate for the activity decay, the total counts of this scan match the counts of the motion experiment.

6.2.8 PET reconstruction

For reconstruction, the algorithm used is a self-normalization reconstruction algorithm, created for this particular scanner and presented by Salomon et al. (2012). This study uses a different approach to calculate the normalization matrix by comparing first the single events among crystals. With this approach, the scanner is calibrated constantly (Salomon et al., 2012). The reconstruction is performed with 1 iteration of 32 sub-iterations with 8 subsets each. After the reconsturction, PET images were filtered with a 1 mm 3D median filter.

6.2.9 Motion correction

The motion estimation of MR gates and PET motion correction is performed with use of the hierarchical adaptive local affine registration toolkit, developed by Buerger et al. (2011) and STIR library. Seven of the eight MR gates are registered to the reference gate and the resulting motion fields were used for motion correction of the PET images.

For this experiment, because the reconstruction algorithm is not capable of performing motion compensated image reconstruction, the correction applied is the reconstruct-transform-average method or RTA. In RTA, the motion fields are applied to the individual PET reconstructed images for motion correction which are then averaged. The correction of PET data has been performed with use of the open source STIR library, release 2.4.

6.3 Results

Figure 6.5 shows the frequency of each gate, as obtained from the MR measurements.

The MR images of the extreme gates are presented in figure 6.6. The maximum displacement of this phantom is calculated to be 4.2 mm.

The motion correction results of the PET data is visible in figure 6.7.

Analysis of the images was performed with the PMOD analysis software. The analysis

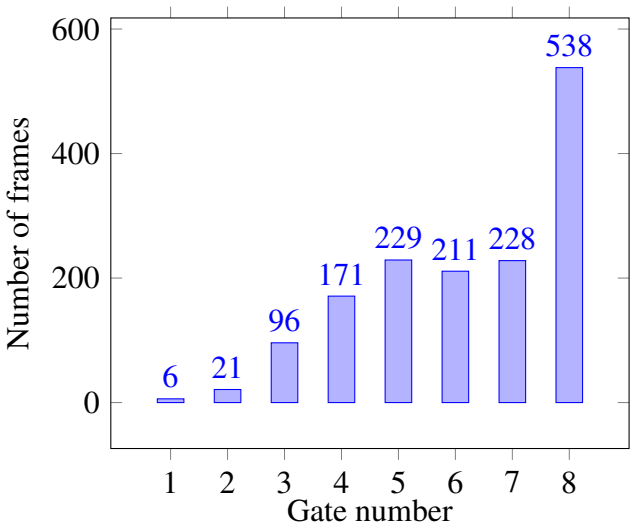

Fig. 6.5 Motion estimation with use of MR data

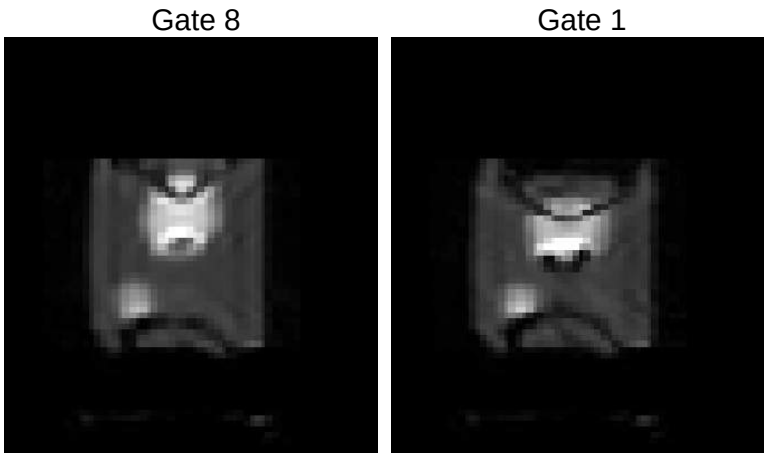

Fig. 6.6 MR image of gate 1 in comparison to gate 8

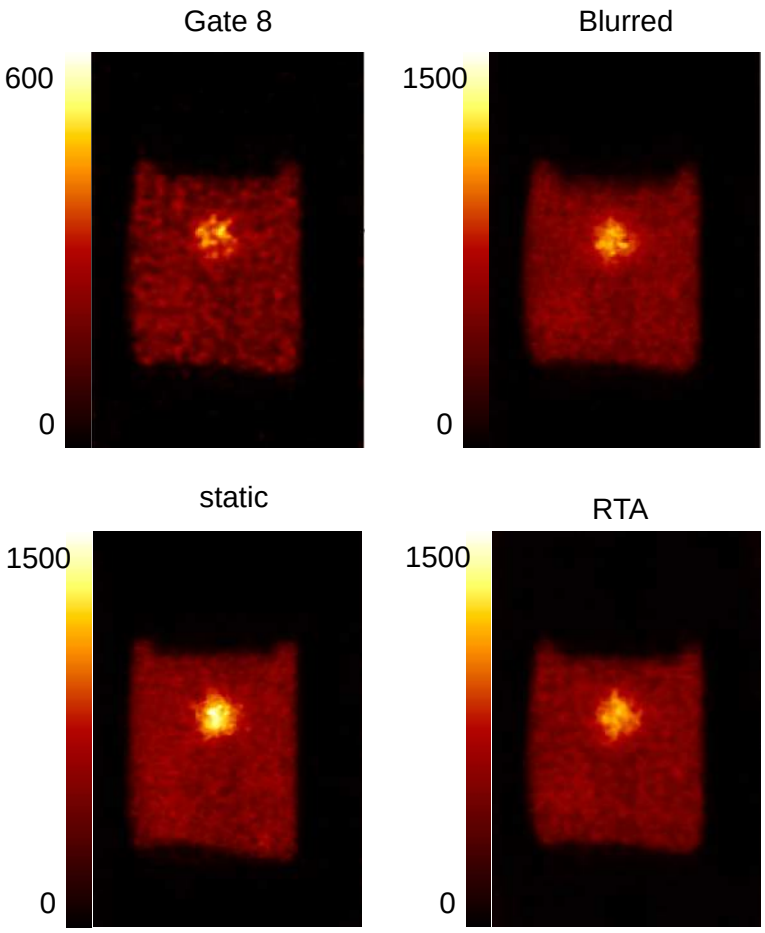

Fig. 6.7 A comparison of reconstructed PET data between a single gate, motion blurred image, the motion corrected (with RTA) and the static image

Table 6.1 Amplitude of intensity in hot area

	Mean intensity within ROI	Standard deviation	Standard error	Volume (cm^3)	Contrast
Static	1101	111	0.87	0.252	1.9
RTA	930	98	0.70	0.302	1.9
Blurred	865	102	0.63	0.393	1.59
Gate 8	979	104	0.81	0.257	1.7

Table 6.2 Volume estimates

	Ideal	MRI	PET
Volume (cm^3)	0.268	0.272	0.252
Variation	–	1.5 %	6.2 %

was concentrated upon the hot lesion in the centre of the phantom. The results are extracted by automatic volume segmentation. The volume segmentation was performed by using thresshold of 50% of the maximum value. The results of this analysis are presented in table 6.1. Results by gate 8 are normalized to fit the other results by multiplying the duration factor of its gate. For each segmented volume total number of voxels is found. Standard error has been calculated by dividing the standard deviation with the square root of the voxel population. The table contains the mean, standard deviation and standard error values of the hot area and the contrast ratio with respect to the background.

Table 6.2 provides information about the volume estimation given by the PET, the MRI after segmentation and the ideal volume of an 8*mm* sphere. The MRI segmentation has been performed by threshold of 50% of the maximum value.

6.4 Discussion

The 9 cm extended field of view of this scanner increased the sensitivity of the PET acquisition and decreased the noise, by comparison with the previous experiment. Also, the extended field of view ensured that there is no transition of activity into or out of the field of view during the motion. In the images, a difference between the blurred and the corrected images is not clearly seen as we would like. In fact both seem to provide less clear images than the static image. This might be due to the relatively small maximum motion amplitude (4.2 mm) which is smaller than the diameter (8 mm) of the hot area, so only small blurring of the hot lesion can be seen.

The quantitative results show that due to motion blurring, the mean amplitude is reduced by 21.4 % and the hot lesion is estimated to be increased in volume by 56%. RTA is able to recover the amplitude partially with 15.6 % decreased amplitude and with 20% volume overestimation which are both improved relative to the blurred image values. The additional comparisons measurements show full recovery of the lesion to background contrast ratio, by 1.59 to 1.9 with RTA motion correction, although this is not so clear usually from the images.

Note that these acquisitions were performed with motion pattern A which has long quiescent periods. Possibly more significant differences are expected for type C.

Volumetric calculations, as presented in Table 6.2 indicate an overestimation of volume by MRI and underestimation by PET. The estimated volume for PET and MRI is close to the ideal. MRI is estimated 1.5 % larger than the ideal but in this case, the big voxel size, combined with the partial volume effect might led to volume overestimation. The partial volume effect also applies in PET data as well. For these reasons the absolute alignment of volume with the ideal is not possible due to partial volume effect of PET and MRI images.

As it is expected, partial volume effect is present in this acquisition even if it is corrected partially during the reconstruction. For this experiment we used a self-normalization

reconstruction algorithm, created for this particular scanner and presented by Salomon et al. (2012). In this algorithm, PSF modelling is included to the normalization matrix.

However, motion effects are the primary target of this experiment and comparing the mean intensities is a viable method of comparison, despite the existence of partial volume effect in all acquisitions. It is proven by Polycarpou et al. (2014) that if motion has higher amplitude than the scanners resolution, motion effects upon the image are the most significant. In this experiment, the resolution of this scanner is less than 1 *mm* and the maximum motion amplitude is 4.2 *mm*. The correction of partial volume effect in correlation with motion correction though is something to be taken into account in future PET-MR motion experiments.

6.5 Conclusions

In this chapter, a fully equipped 3D PET insert was used for simultaneous PET-MR motion correction with PVA cryogel. Even the impact of motion blurring is less visible in this motion pattern, as analysed by Polycarpou et al., the effects of motion are still measured and with motion amplitude smaller than the object itself (Polycarpou et al., 2014). Given the fact that contrast recovery is successful with RTA, and the estimated volume is recovered by comparison with the motion blurred, motion correction was beneficial for this phantom experiment.

Chapter 7

General conclusion and future perspectives

The aim of this thesis is the introduction of novel methodologies and equipment for investigating motion correction during simultaneous PET-MR acquisitions. Motion correction is a field of study open for investigation and improvement. The most common use of PET; oncology, indicates that there is need for imaging of soft tissue high metabolism. Tissue during motion is affected not only by displacement but deformation as well. One aim is to mimic the elastic properties of tissue by introducing such properties. Just as for the rigid phantoms used until now, compartmentalization of the phantom into a complex structure is useful.This system moves with an appropriate MR-compatible motor unit.

The development of PVA cryogel is a solution for experiments with motion for simultaneous PET-MR. The phantom is visible in both modalities, it is adaptive to the needs of the user and it has physical properties which have been measured and characterized. The alteration of the freeze-thaw preparation resulted in some variations in elasticity, nevertheless, this was necessary for the utilization of short half-life isotopes and any changes in properties are acceptable. The Young's modulus elasticity results were acceptable for the current motor unit systems used. A disadvantage of this system is the diffusion of the iso-

tope inside the compound. Even if the rate is slow, the optimum would be the binding of the radio-molecule with the phantom. However, PVA cryogel can be a valuable phantom for simultaneous PET-MR for motion correction. It can be adapted and compartmentalized as demonstrated with the experimental studies and it can be used in other modalities such as SPECT.

Motion experiments though had to overcome a significant factor, which is the motion itself. The inhospitable environment of high magnetic field does not tolerate ferromagnetic motor units. Appropriate use of stepper motors outside the magnetic field provided the necessary input for experiments with controlled motion. Stop-and-shoot experiments are invaluable but aspects as intra-frame motion and motion artefacts are not considered. This is the reason that in the upgraded experiment with use of a stepper motor we presented successful motion correction for continuous movement. This experiment also indicated the relevant technical issues of a simultaneous acquisition such as the need for temporal synchronization and spatial alignment.

Following this experiment, and by progressing to the next generation PET scanners, the experiment becomes more complicated. PVA cryogel is used for these experiments and the success of motion correction has been investigated. The first experiment with HYPERimage PET insert is a stop-and-shoot acquisition and with no background activity. The short FOV of this scanner was a limiting factor as to how big the axial dimensions of the phantom could be during acquisition. Even with these technical difficulties, motion capture and correction was successful with RTA (Reconstruct Transform Average) and MCIR (Motion Compensated Image Reconstruction) although images of the phantom obtained with the HYPERimage scanner were of poor quality.

The next goal was to adapt the scanner setting to the needs of the experiments. This led to the establishment of synchronization methodology with use of gradient sensors in the PET insert and spatial alignment using a co-registration phantom for each experiment.

A new set of studies was initiated in which the motion pattern was fully controlled by a servo motor and the motion pattern was derived by human respiratory motion. The phantom design was also adapted to resemble the liver-lung boundary. In this experiment though, there is no method to avoid motion of radioactive areas inside and outside the PET FOV, and it is possible that this effect had an impact upon the final images. Motion correction in these experiments is effective, despite the very noisy images, due to the small FOV of the scanner.

Finally, the longer (9 cm) axial FOV provided by Hyperion-II^D gave the possibility to lower the noise and avoid "out of FOV" issues by having the entire phantom inside the FOV. With use of the PVA phantom again, the experiment incorporated the most common motion pattern and the motion correction applied is the kind of correction that can be used in any PET-MR system. The results indicate a partial recovery of the mean values in the hot area of the phantom with full recovery of the lesion to background ratio and also improvement to the volume estimation although the image quality remains poor.

A common ground of poor performance for motion correction, in all experiments, and by comparing with past studies, is the continuous motion. Intra-frame motion affects the MR images. Consequently, the motion fields by the blurred MR images affect the outcome of the PET motion correction.

To conclude, the use of an elastic phantom is justified by the physical properties of the human tissue as described by literature. The means to investigate this and provide appropriate solutions of correction can be explored with PVA cryogel. The phantom itself though cannot provide all the necessary information unless handled with the appropriate tools. Temporal synchronization is an aspect introduced by PET-MR. The accuracy of this synchronization as well as the spatial alignment are essential for accurate motion correction.

This thesis concluded with the performance of experiments using the next generation of MR-compatible PET insert. The future development of this work may include further de-

velopment of the PVA cryogel with more investigation of ways to eliminate diffusion. Also, dedicated moulds can be designed and standard operating procedures can be established for automated phantom production. The size of PVA phantom for clinical use is also worthy of investigation. Furthermore, there are many other polymers that can be investigated, in elastic or inelastic form, creating as complex distributions as the experimental setup requires. Finally, PVA cryogel with continuous motion could be used to determine the standards of data handling and gating of PET-MR scanners.

References

Abd Rahni, A. A., Lewis, E., Guy, M., Goswami, B., and Wells, K. (2011). A Particle Filter Approach to Respiratory Motion Estimation in Nuclear Medicine Imaging. *IEEE Transactions on Nuclear Science*, 58(5):2276–2285.

Alnowami, M., Lewis, E., Guy, M., and Wells, K. (2010). Marker-less tracking for respiratory motion correction in nuclear medicine. *IEEE Nuclear Science Symposium and Medical Imaging Conference (NSS/MIC)*, pages 3118–3121.

Anderson, C. (1932). The apparent existence of easily deflectable positives. *Science*, 76:238–239.

Bai, W. J. and Brady, M. (2011). Motion Correction and Attenuation Correction for Respiratory Gated PET Images. *IEEE Transactions on Medical Imaging*, 30(2):351–365.

Bartling, S. H., Stiller, W., Grasruck, M., Schmidt, B., Peschke, P., Semmler, W., and Kiessling, F. (2007). Retrospective motion gating in small animal CT of mice and rats. *Investigative Radiology*, 42(10):704–14.

Blume, U., Orbell, J., Waltham, M., Smith, A., Razavi, R., and Schaeffter, T. (2009). 3D T(1)-mapping for the characterization of deep vein thrombosis. *MAGMA*, 22(6):375–83.

Buerger, C., Schaeffter, T., and King, A. P. (2011). Hierarchical adaptive local affine registration for fast and robust respiratory motion estimation . *Medical Image Analysis*, 15(4):551 – 564.

Bushberg, J. T. (1994). *The essential physics of medical imaging*. Williams and Wilkins, Baltimore.

Buzhan, P., Dolgoshein, B., Filatov, L., Ilyin, A., Kaplin, V., Karakash, A., Klemin, S., Mirzoyan, R., Otte, A. N., Popova, E., Sosnovtsev, V., and Teshima, M. (2006). Large area silicon photomultipliers: Performance and applications. *Nuclear Instruments & Methods in Physics Research Section A-Accelerators Spectrometers Detectors and Associated Equipment*, 567(1):78–82.

Cao, Z., Gilland, D., Mair, B., and Jaszczak, R. (2003). Three-dimensional motion estimation with image reconstruction for gated cardiac ECT. *IEEE Transactions on Nuclear Science*, 50(3):384–388.

Catana, C., Benner, T., van der Kouwe, A., Byars, L., Hamm, M., Chonde, D. B., Michel, C. J., El Fakhri, G., Schmand, M., and Sorensen, A. G. (2011). MRI-assisted PET motion correction for neurologic studies in an integrated MR-PET scanner. *Journal of Nuclear Medicine*, 52(1):154–61.

Catana, C., Wu, Y. B., Judenhofer, M. S., Qi, J. Y., Pichler, B. J., and Cherry, S. R. (2006). Simultaneous acquisition of multislice PET and MR images: Initial results with a MR-compatible PET scanner. *Journal of Nuclear Medicine*, 47(12):1968–1976.

Cherry, S. R., Shao, Y. P., Siegel, S., Silverman, R. W., Mumcuoglu, E., Meadors, K., and Phelps, M. E. (1996). Optical fiber readout of scintillator arrays using a multi-channel PMT: A high resolution PET detector for animal imaging. *IEEE Transactions on Nuclear Science*, 43(3):1932–1937.

Cherry, S. R., Sorenson, J. A., and Phelps, M. E. (2012). *Physics in nuclear medicine*. Elsevier Health Sciences, Baltimore.

Chu, K. C., Jordan, K. J., Battista, J. J., Van Dyk, J., and Rutt, B. K. (2000). Polyvinyl alcohol-Fricke hydrogel and cryogel: two new gel dosimetry systems with low Fe3+ diffusion. *Physics in Medicine and Biology*, 45(4):955–69.

Chu, K. C. and Rutt, B. K. (1997). Polyvinyl alcohol cryogel: an ideal phantom material for MR studies of arterial flow and elasticity. *Magnetic Resonance in Medicine*, 37(2):314–9.

Chun, S. Y., Reese, T. G., Ouyang, J., Guerin, B., Catana, C., Zhu, X., Alpert, N. M., and El Fakhri, G. (2012). MRI-Based Nonrigid Motion Correction in Simultaneous PET/MRI. *Journal of Nuclear Medicine*.

Crum, W. R., Camara, O., and Hawkes, D. J. (2007). Methods for inverting dense displacement fields: evaluation in brain image registration. *Medical Image Computing and Computer-Assisted Intervention*, 10(Pt 1):900–7.

D'ausilio, A. (2012). Arduino: A low-cost multipurpose lab equipment. *Behavior Research Methods*, 44(2):305–313.

Dawood, M., Büther, F., Stegger, L., Jiang, X., Schober, O., Schäfers, M., and Schäfers, K. P. (2009). Optimal number of respiratory gates in positron emission tomography: a cardiac patient study. *Medical Physics*, 36(5):1775–84.

Dawood, M., Lang, N., Jiang, X., and Schäfers, K. P. (2006). Lung motion correction on respiratory gated 3-D PET/CT images. *IEEE Transactions on Medical Imaging*, 25(4):476–85.

de Rosales, R. T. (2014). Potential clinical applications of bimodal PET-MRI or SPECT-MRI agents. *Journal of labelled compounds & radiopharmaceuticals*, 57(4):298–303.

Delso, G., Furst, S., Jakoby, B., Ladebeck, R., Ganter, C., Nekolla, S. G., Schwaiger, M., and Ziegler, S. I. (2011). Performance Measurements of the Siemens mMR Integrated Whole-Body PET/MR Scanner. *Journal of Nuclear Medicine*, 52(12):1914–1922.

Dietrich, L., Jetter, S., Tücking, T., Nill, S., and Oelfke, U. (2006). Linac-integrated 4D cone beam CT: first experimental results. *Physics in Medicine and Biology*, 51(11):2939–52.

Dirac, P. A. (1931). Quantized Singularities in the Electromagnetic Field. *Proceedings of the Royal Society of London. Series A, Containing Papers of a Mathematical and Physical Character*, A133:60–72.

Duboeuf, F., Basarab, A., Liebgott, H., Brusseau, E., Delachartre, P., and Vray, D. (2009). Investigation of PVA cryogel Young's modulus stability with time, controlled by a simple reliable technique. *Medical Physics*, 36(2):656–61.

Duppenbecker, P., Weissler, B., Gebhardt, P., Schug, D., Wehner, J., Marsden, P., and Schulz, V. (2012). Development of an MRI compatible digital SiPM based PET detector stack for simultaneous preclinical PET/MRI. *IEEE Nuclear Science Symposium and Medical Imaging Conference (NSS/MIC)*, pages 3481–3483.

Fieseler, M., Kugel, H., Gigengack, F., Kosters, T., Buther, F., Quick, H. H., Faber, C., Jiang, X. Y., and Schafers, K. P. (2013). A dynamic thorax phantom for the assessment of cardiac and respiratory motion correction in PET/MRI: A preliminary evaluation. *Nuclear Instruments & Methods in Physics Research Section A-Accelerators Spectrometers Detectors and Associated Equipment*, 702:59–63.

Frach, T., Prescher, G., Degenhardt, C., de Gruyter, R., Schmitz, A., and Ballizany, R. (2009). The Digital Silicon Photomultiplier - Principle of Operation and Intrinsic Detector Performance. *2009 IEEE Nuclear Science Symposium Conference Record, Vols 1-5*, pages 1959–1965.

Fromageau, J., Brusseau, E., Vray, D., Gimenez, G., and Delachartre, P. (2003). Characterization of PVA cryogel for intravascular ultrasound elasticity imaging. *IEEE Transactions on Ultrasonics Ferroelectrics and Frequency Control*, 50(10):1318–1324.

Fromageau, J., Gennisson, J. L., Schmitt, C., Maurice, R. L., Mongrain, R., and Cloutier, G. (2007). Estimation of polyvinyl alcohol cryogel mechanical properties with four ultrasound elastography methods and comparison with gold standard testings. *IEEE Transactions on Ultrasonics Ferroelectrics and Frequency Control*, 54(3):498–509.

Garlick, P. B., Marsden, P. K., Cave, A. C., Parkes, H. G., Slates, R., Shao, Y. P., Silverman, R. W., and Cherry, S. R. (1997). PET and NMR dual acquisition (PANDA): Applications to isolated, perfused rat hearts. *NMR in Biomedicine*, 10(3):138–142.

Gigengack, F., Ruthotto, L., Burger, M., Wolters, C. H., Jiang, X., and Schafers, K. P. (2012). Motion correction in dual gated cardiac PET using mass-preserving image registration. *IEEE Transactions on Medical Imaging*, 31(3):698–712.

Guerin, B., Cho, S., Chun, S. Y., Zhu, X., Alpert, N. M., El Fakhri, G., Reese, T., and Catana, C. (2011). Nonrigid PET motion compensation in the lower abdomen using simultaneous tagged-MRI and PET imaging. *Medical Physics*, 38(6):3025–3038.

Hammer, B. E., Christensen, N. L., and Heil, B. G. (1994). Use of a Magnetic-Field to Increase the Spatial-Resolution Positron Emission Tomography. *Medical Physics*, 21(12):1917–1920.

Herrmann, K., Kohan, A., Gaeta, M., Rubbert, C., Vercher-Conejero, J., Paspulati, R., Antonis, K., Mansoori, B., Faulhaber, P., Avril, N., and Ros, P. (2013). PET/MRI: Applications in Clinical Imaging. *Current Radiology Reports*, 1(3):161–176.

Hill, B., Back, S. A., Lepage, M., Simpson, J., Healy, B., and Baldock, C. (2002). Investigation and analysis of ferrous sulfate polyvinyl alcohol (PVA) gel dosimeter. *Physics in Medicine and Biology*, 47(23):4233–46.

Hudson, H. M. and Larkin, R. S. (1994). Accelerated image reconstruction using ordered subsets of projection data. *IEEE Transactions on Medical Imaging*, 13(4):601–9.

Judenhofer, M. S. and Cherry, S. R. (2013). Applications for Preclinical PET/MRI. *Seminars in Nuclear Medicine*, 43(1):19–29.

Kalender, W. A., Rienmüller, R., Seissler, W., Behr, J., Welke, M., and Fichte, H. (1990). Measurement of pulmonary parenchymal attenuation: use of spirometric gating with quantitative CT. *Radiology*, 175(1):265–8.

Keereman, V., Fierens, Y., Broux, T., De Deene, Y., Lonneux, M., and Vandenberghe, S. (2010). MRI-based attenuation correction for PET/MRI using ultrashort echo time sequences. *Journal of Nuclear Medicine*, 51(5):812–8.

King, A. P., Buerger, C., Tsoumpas, C., Marsden, P. K., and Schaeffter, T. (2012). Thoracic respiratory motion estimation from MRI using a statistical model and a 2-D image navigator. *Medical Image Analysis*, 16(1):252–64.

Kolb, A., Wehrl, H. F., Hofmann, M., Judenhofer, M. S., Eriksson, L., Ladebeck, R., Lichy, M. P., Byars, L., Michel, C., Schlemmer, H. P., Schmand, M., Claussen, C. D., Sossi, V., and Pichler, B. J. (2012). Technical performance evaluation of a human brain PET/MRI system. *European Radiology*, 22(8):1776–1788.

Krouskop, T. A., Wheeler, T. M., Kallel, F., Garra, B. S., and Hall, T. (1998). Elastic moduli of breast and prostate tissues under compression. *Ultrasonic Imaging*, 20(4):260–274.

Kubo, H. D. and Hill, B. C. (1996). Respiration gated radiotherapy treatment: a technical study. *Physics in Medicine and Biology*, 41(1):83–91.

Kyme, A., Se, S., Meikle, S., Angelis, G., Ryder, W., Popovich, K., Yatigammana, D., and Fulton, R. (2014). Markerless motion tracking of awake animals in positron emission tomography. *IEEE Transactions on Medical Imaging*, PP(99):1–1.

Kyme, A. Z., Zhou, V. W., Meikle, S. R., and Fulton, R. R. (2008). Real-time 3D motion tracking for small animal brain PET. *Physics in Medicine and Biology*, 53(10):2651.

Kyriakou, E. and McKenzie, D. R. (2012). Changes in lung tumor shape during respiration. *Physics in Medicine and Biology*, 57(4):919–35.

Lamare, F., Ledesma Carbayo, M. J., Cresson, T., Kontaxakis, G., Santos, A., Le Rest, C. C., Reader, A. J., and Visvikis, D. (2007). List-mode-based reconstruction for respiratory motion correction in PET using non-rigid body transformations. *Physics in Medicine and Biology*, 52(17):5187–204.

Langen, K. M. and Jones, D. T. (2001). Organ motion and its management. *International Journal of Radiation, Oncology, Biology, Physics*, 50(1):265–78.

Lee, V. S. (2006). *Cardiovasculat MRI: physical principles to practical protocols*. Lippincott Williams & Wilkins, Philadelphia.

Lentschig, M. G., Reimer, P., Rausch-Lentschig, U. L., Allkemper, T., Oelerich, M., and Laub, G. (1998). Breath-hold gadolinium-enhanced MR angiography of the major vessels at 1.0 T: dose-response findings and angiographic correlation. *Radiology*, 208(2):353–7.

Li, T., Thorndyke, B., Schreibmann, E., Yang, Y., and Xing, L. (2006a). Model-based image reconstruction for four-dimensional PET. *Medical Physics*, 33(5):1288–98.

Li, X. A., Stepaniak, C., and Gore, E. (2006b). Technical and dosimetric aspects of respiratory gating using a pressure-sensor motion monitoring system. *Medical Physics*, 33(1):145–54.

Ling, C. C., Humm, J., Larson, S., Amols, H., Fuks, Z., Leibel, S., and Koutcher, J. A. (2000). Towards multidimensional radiotherapy (MD-CRT): biological imaging and biological conformality. *International Journal of Radiation, Oncology, Biology, Physics*, 47(3):551–60.

Liu, H. H., Balter, P., Tutt, T., Choi, B., Zhang, J., Wang, C., Chi, M., Luo, D., Pan, T., Hunjan, S., Starkschall, G., Rosen, I., Prado, K., Liao, Z., Chang, J., Komaki, R., Cox, J. D., Mohan, R., and Dong, L. (2007). Assessing respiration-induced tumor motion and internal target volume using four-dimensional computed tomography for radiotherapy of lung cancer. *International Journal of Radiation, Oncology, Biology, Physics*, 68(2):531–40.

Lucas, A. J., Hawkes, R. C., Ansorge, R. E., Williams, G. B., Nutt, R. E., Clark, J. C., Fryer, T. A., and Carpenter, T. A. (2006). Development of a combined microPET((R))-MR system. *Technology in Cancer Research & Treatment*, 5(4):337–341.

Lukas, L. A., Surry, K. J. M., and Peters, T. M. (2001). Temperature dosimetry using MR relaxation characteristics of poly(vinyl alcohol) cryogel (PVA-C). *Magnetic Resonance in Medicine*, 46(5):1006–1013.

Mackewn, J., Lerche, C., Sunassee, K., de Rosales, R., Phinikaridou, A., Salomon, A., Ayres, R., Tsoumpas, C., SouItanidis, G., Schaeffter, T., Marsden, P., and Schulz, V. (2012). PET performance evaluation of a pre-clinical SiPM based MR-compatible PET scanner. *IEEE Nuclear Science Symposium and Medical Imaging Conference (NSS/MIC)*, pages 2776–2779.

Mackewn, J., Lerche, C., Weissler, B., Sunassee, K., de Rosales, R., Phinikaridou, A., Salomon, A., Ayres, R., Tsoumpas, C., Soultanidis, G., Gebhardt, P., Schaeffter, T., Marsden, P., and Schulz, V. (2015). PET Performance Evaluation of a Pre-Clinical SiPM-Based MR-Compatible PET Scanner. *Nuclear Science, IEEE Transactions on*, 62(3):784–790.

Mackewn, J. E., Strul, D., Hallett, W. A., Halsted, P., Page, R. A., Keevil, S. F., Williams, S. C. R., Cherry, S. R., and Marsden, P. K. (2005). Design and development of an MR-compatible PET scanner for imaging small animals. *IEEE Transactions on Nuclear Science*, 52(5):1376–1380.

Madsen, E. L. and Fullerton, G. D. (1982). Prospective tissue-mimicking materials for use in NMR imaging phantoms. *Magnetic Resonance in Imaging*, 1(3):135–41.

Makowski, M. R., Wiethoff, A. J., Blume, U., Cuello, F., Warley, A., Jansen, C. H., Nagel, E., Razavi, R., Onthank, D. C., Cesati, R. R., Marber, M. S., Schaeffter, T., Smith, A., Robinson, S. P., and Botnar, R. M. (2011). Assessment of atherosclerotic plaque burden with an elastin-specific magnetic resonance contrast agent. *Nature Medicine*, 17(3):383–8.

Malone, I. B., Ansorge, R. E., Williams, G. B., Nestor, P. J., Carpenter, T. A., and Fryer, T. D. (2011). Attenuation correction methods suitable for brain imaging with a PET/MRI scanner: a comparison of tissue atlas and template attenuation map approaches. *Journal of Nuclear Medicine*, 52(7):1142–9.

Manjeshwar, R., Tao, X., Asma, E., and Thielemans, K. (2006). Motion compensated image reconstruction of respiratory gated PET/CT. *3rd IEEE International Symposium on Biomedical Imaging: Nano to Macro, 2006*, pages 674–677.

Martínez-Möller, A., Bundschuh, R., Riedel, M., Navab, N., Ziegler, S., Schwaiger, M., and Nekolla, S. (2007). Comparison of respiratory sensors and its compliance for respiratory gating in emission tomography. *Journal of Nuclear Medicine*, 48(supplement 2):426P–426P.

Martinez-Möller, A., Souvatzoglou, M., Delso, G., Bundschuh, R. A., Chefd'hotel, C., Ziegler, S. I., Navab, N., Schwaiger, M., and Nekolla, S. G. (2009). Tissue classification as a potential approach for attenuation correction in whole-body PET/MRI: evaluation with PET/CT data. *Journal of Nuclear Medicine*, 50(4):520–6.

Mathur-De Vre, R., Grimee, R., Parmentier, F., and Binet, J. (1985). The use of agar gel as a basic reference material for calibrating relaxation times and imaging parameters. *Magnetic Resonance in Medicine*, 2(2):176–9.

Muehllehner, G., Wake, R. H., and Sano, R. (1981). Standards for performance measurements in scintillation cameras. *Journal of Nuclear Medicine*, 22(1):72–7.

Nakamura, H., Ito, N., Kotake, F., Mizokami, Y., and Matsuoka, T. (2000). Tumor-detecting capacity and clinical usefulness of SPIO-MRI in patients with hepatocellular carcinoma. *Journal of Gastroenterology*, 35(11):849–55.

Nehmeh, S. A. and Erdi, Y. E. (2008). Respiratory motion in positron emission tomography/computed tomography: a review. *Seminars in Nuclear Medicine*, 38(3):167–76.

Nehmeh, S. A., Erdi, Y. E., Pan, T., Pevsner, A., Rosenzweig, K. E., Yorke, E., Mageras, G. S., Schoder, H., Vernon, P., Squire, O., Mostafavi, H., Larson, S. M., and Humm, J. L. (2004). Four-dimensional (4D) PET/CT imaging of the thorax. *Medical Physics*, 31(12):3179–86.

Ng, T. S. C., Procissi, D., Wu, Y., and Jacobs, R. E. (2010). A robust coregistration method for in vivo studies using a first generation simultaneous PET/MR scanner. *Medical Physics*, 37(5):1995–2003.

Nguyen, T.-N., Moseley, J. L., Dawson, L. A., Jaffray, D. A., and Brock, K. K. (2008). Adapting population liver motion models for individualized online image-guided therapy. *Conf Proc IEEE Eng Med Biol Soc*, 2008:3945–8.

Ozhasoglu, C. and Murphy, M. J. (2002). Issues in respiratory motion compensation during external-beam radiotherapy . *International Journal of Radiation, Oncology, Biology, Physics*, 52(5):1389 – 1399.

Picard, Y. and Thompson, C. J. (1997). Motion correction of PET images using multiple acquisition frames. *IEEE Transactions in Medical Imaging*, 16(2):137–44.

Pichler, B., Lorenz, E., Mirzoyan, R., Pimpl, W., Roder, F., Schwaiger, M., and Ziegler, S. I. (1998). Performance test of a LSO-APD PET module in a 9.4 Tesla magnet. *1997 IEEE Nuclear Science Symposium - Conference Record, Vols 1 & 2*, pages 1237–1239.

Polycarpou, I., Tsoumpas, C., King, A. P., and Marsden, P. K. (2014). Impact of respiratory motion correction and spatial resolution on lesion detection in PET: a simulation study based on real MR dynamic data. *Physics in Medicine and Biology*, 59(3):697–713.

Polycarpou, I., Tsoumpas, C., and Marsden, P. K. (2012). Analysis and comparison of two methods for motion correction in PET imaging. *Medical Physics*, 39(10):6474–83.

Qiao, F., Pan, T., Clark, J. W., and Mawlawi, O. R. (2006). A motion-incorporated reconstruction method for gated PET studies. *Physics in Medicine and Biology*, 51(15):3769–83.

Renker, D. (2002). Properties of avalanche photodiodes for applications in high energy physics, astrophysics and medical imaging. *Nuclear Instruments & Methods in Physics Research Section A-Accelerators Spectrometers Detectors and Associated Equipment*, 486(1-2):164–169.

Riegel, A. C., Bucci, M. K., Mawlawi, O. R., Johnson, V., Ahmad, M., Sun, X., Luo, D., Chandler, A. G., and Pan, T. (2010). Target definition of moving lung tumors in positron emission tomography: correlation of optimal activity concentration thresholds with object size, motion extent, and source-to-background ratio. *Medical Physics*, 37(4):1742–52.

Rietzel, E., Chen, G. T. Y., Choi, N. C., and Willet, C. G. (2005). Four-dimensional image-based treatment planning: Target volume segmentation and dose calculation in the presence of respiratory motion. *International Journal of Radiation, Oncology, Biology, Physics*, 61(5):1535–50.

Sachs, T. S., Meyer, C. H., Hu, B. S., Kohli, J., Nishimura, D. G., and Macovski, A. (1994). Real-time motion detection in spiral MRI using navigators. *Magnetic Resonance in Medicine*, 32(5):639–45.

Salomon, A., Goldschmidt, B., Botnar, R., Kiessling, F., and Schulz, V. (2012). A self-normalization reconstruction technique for PET scans using the positron emission data. *IEEE Transactions on Medical Imaging*, 31(12):2234–40.

Schleyer, P. J., O'Doherty, M. J., Barrington, S. F., Morton, G., and Marsden, P. K. (2013). Comparing approaches to correct for respiratory motion in NH3 PET-CT cardiac perfusion imaging. *Nuclear Medicine Communications*, 34(12):1174–84.

Schleyer, P. J., Thielemans, K., and Marsden, P. K. (2014). Extracting a respiratory signal from raw dynamic PET data that contain tracer kinetics. *Physics in Medicine and Biology*, 59(15):4345–56.

Schnabel, J., Rueckert, D., Quist, M., Blackall, J., Castellano-Smith, A., Hartkens, T., Penney, G., Hall, W., Liu, H., Truwit, C., Gerritsen, F., Hill, D., and Hawkes, D. (2001). A Generic Framework for Non-rigid Registration Based on Non-uniform Multi-level Free-Form Deformations. *Medical Image Computing and Computer-Assisted Intervention – MICCAI 2001*, 2208:573–581.

Schug, D., Lerche, C., Dueppenbecker, P., Gebhardt, P., Goldschmidt, B., Salomon, A., Wehner, J., Weissler, B., Kiessling, F., and Schulz, V. (2014). PET performance evaluation of a preclinical digital PET/MRI insert. *EJNMMI Physics, PSMR-2014 conference*, 1(Suppl 1):A3.

Schulz, V., Solf, T., Weissler, B., Gebhardt, P., Fischer, P., Ritzert, M., Mlotok, V., Piemonte, C., Zorzi, N., Melchiorri, M., Vandenberghe, S., Keereman, V., Schaeffter, T., and Marsden, P. K. (2009). A Preclinical PET/MR Insert for a Human 3T MR Scanner. *2009 IEEE Nuclear Science Symposium Conference Record, Vols 1-5*, pages 2577–2579, 4204.

Schulz, V., Weissler, B., Gebhardt, P., Solf, T., Lerche, C., Fischer, P., Ritzert, M., Mlotok, V., Piemonte, C., Goldschmidt, B., Vandenberghe, S., Salomon, A., Schaeffter, T., and Marsden, P. (2011). SiPM based preclinical PET/MR insert for a human 3T MR: first imaging experiments. *IEEE Nuclear Science Symposium and Medical Imaging Conference (NSS/MIC)*, pages 4467–4469.

Segars, W. P., Tsui, B. M. W., Frey, E. C., Johnson, G. A., and Berr, S. S. (2004). Development of a 4-D digital mouse phantom for molecular imaging research. *Molecular Imaging and Biology*, 6(3):149–59.

Serway, R. A. and Jewett, J. W. (2004). *Physics for scientists and engineers, with modern physics*. Thomson-Brooks/Cole, Belmont, CA, 6th edition.

Shao, Y., Cherry, S. R., Farahani, K., Slates, R., Silverman, R. W., Meadors, K., Bowery, A., Siegel, S., Marsden, P. K., and Garlick, P. B. (1997). Development of a PET detector system compatible with MRI/NMR systems. *IEEE Transactions on Nuclear Science*, 44(3):1167–1171.

Shechter, G., Ozturk, C., Resar, J., and McVeigh, E. (2004). Respiratory motion of the heart from free breathing coronary angiograms. *IEEE Transactions on Medical Imaging*, 23(8):1046–1056.

Smith, R. L., Wells, K., Jones, J., Dasari, P., Lindsay, C., and King, M. (2013). Toward a framework for high resolution parametric respiratory motion modelling. *IEEE Nuclear Science Symposium and Medical Imaging Conference (NSS/MIC)*, pages 1–4.

Sodickson, L., Bowman, W., Stephenson, J., and Weinstein, R. (1961). Single-quantum annihilation of positrons. *Physical Review*, 124:1851–1861.

Soultanidis, G., Mackewn, J., Tsoumpas, C., and Marsden, P. (2013a). PVA Cryogel for Construction of Deformable PET-MR Visible Phantoms. *IEEE Transactions on Nuclear Science*, 60(1):95–102.

Soultanidis, G., Polycarpou, I., Weissler, B., Lerche, C., Mackewn, J., Ayres, R., Tsoumpas, C., Schulz, V., and Marsden, P. (2013b). Demonstration of motion correction for PET-MR with PVA cryogel phantoms. *IEEE Nuclear Science Symposium and Medical Imaging Conference (NSS/MIC)*, pages 1–4.

Soultanidis, G. M., Mackewn, J. E., Lerche, C. W., Tsoumpas, C., Buerger, C., Szanda, I., Halsted, P., Schaeffter, T., Schulz, V., and Marsden, P. K. (2011). Design and development of phantoms capable of continuous motion during simultaneous PET-MR acquisitions.

IEEE Nuclear Science Symposium and Medical Imaging Conference (NSS/MIC), pages 3567–3571.

Surry, K., Austin, H., Fenster, A., and Peters, T. (2004). Poly(vinyl alcohol) cryogel phantoms for use in ultrasound and MR imaging. *Physics in Medicine and Biology*, 49(24):5529–5546.

Szanda, I., Mackewn, J., Patay, G., Major, P., Sunassee, K., Mullen, G. E., Nemeth, G., Haemisch, Y., Blower, P. J., and Marsden, P. K. (2011). National Electrical Manufacturers Association NU-4 Performance Evaluation of the PET Component of the NanoPET/CT Preclinical PET/CT Scanner. *Journal of Nuclear Medicine*, 52(11):1741–7.

Taylor, K. M. L., Rieter, W. J., and Lin, W. (2008). Manganese-based nanoscale metal-organic frameworks for magnetic resonance imaging. *Journal of the American Chemical Society*, 130(44):14358–9.

Taylor, R. M., Huber, D. L., Monson, T. C., Ali, A.-M. S., Bisoffi, M., and Sillerud, L. O. (2011). Multifunctional iron platinum stealth immunomicelles: targeted detection of human prostate cancer cells using both fluorescence and magnetic resonance imaging. *Journal Nanoparticle Research*, 13(10):4717–4729.

Thielemans, K., Tsoumpas, C., Mustafovic, S., Beisel, T., Aguiar, P., Dikaios, N., and Jacobson, M. W. (2012). STIR: software for tomographic image reconstruction release 2. *Physics in Medicine and Biology*, 57(4):867–83.

Tsoumpas, C., Mackewn, J. E., Halsted, P., King, A. P., Buerger, C., Totman, J. J., Schaeffter, T., and Marsden, P. K. (2010). Simultaneous PET-MR acquisition and MR-derived motion fields for correction of non-rigid motion in PET. *Annals of Nuclear Medicine*, 24(10):745–50.

Tsoumpas, C., Polycarpou, I., Thielemans, K., Buerger, C., King, A. P., Schaeffter, T., and Marsden, P. K. (2013). The effect of regularization in motion compensated PET image reconstruction: a realistic numerical 4D simulation study. *Physics in Medicine and Biology*, 58(6):1759–73.

Vandenberghe, S., D'Asseler, Y., Van de Walle, R., Kauppinen, T., Koole, M., Bouwens, L., Van Laere, K., Lemahieu, I., and Dierckx, R. A. (2001). Iterative reconstruction algorithms in nuclear medicine. *Computerized Medical Imaging and Graphics*, 25(2):105–11.

Von Siebenthal, M. (2008). *Analysis and modelling of respiratory liver motion using 4DMRI*. PhD thesis, ETH Zurich.

Wehner, J., Weissler, B., Dueppenbecker, P., Gebhardt, P., Schug, D., Ruetten, W., Kiessling, F., and Schulz, V. (2014). PET/MRI insert using digital SiPMs: Investigation of MR-compatibility . *Nuclear Instruments & Methods in Physics Research Section A: Accelerators, Spectrometers, Detectors and Associated Equipment*, 734, Part B(0):116 – 121.

Weissler, B., Gebhardt, P., Diippenbecker, P., Goldschmidt, B., Salomon, A., Schug, D., Wehner, J., Lerche, C., Wirtz, D., Renz, W., Schumacher, K., Zwaans, B., Marsden, P., Kiessling, F., and Schulz, V. (2012). Design concept of world's first preclinical PET/MR insert with fully digital silicon photomultiplier technology. *IEEE Nuclear Science Symposium and Medical Imaging Conference (NSS/MIC)*, pages 2113–2116.

Weissler, B., Gebhardt, P., Duppenbecker, P., Wehner, J., Schug, D., Lerche, C., Goldschmidt, B., Salomon, A., Verel, I., Heijman, E., Perkuhn, M., Heberling, D., Botnar, R., Kiessling, F., and Schulz, V. (2015a). A Digital Preclinical PET/MRI Insert and Initial Results. *IEEE Transactions in Medical Imaging*.

Weissler, B., Gebhardt, P., Lerche, C., Soultanidis, G., Wehner, J., Heberling, D., and Schulz, V. (2014). PET/MR synchronization by detection of switching gradients. *EJNMMI Physics, PSMR-2014 conference*, 1(Suppl 1):A4.

Weissler, B., Gebhardt, P., Lerche, C., Soultanidis, G., Wehner, J., Heberling, D., and Schulz, V. (2015b). PET/MR Synchronization by Detection of Switching Gradients. *Nuclear Science, IEEE Transactions on*, 62(3):650–657.

Westbrook, C. and Kaut, C. (1998). *MRI in practice*. Blackwell Science, Oxford England ; Malden, MA, USA, 2nd edition.

White, N., Roddey, C., Shankaranarayanan, A., Han, E., Rettmann, D., Santos, J., Kuperman, J., and Dale, A. (2010). PROMO: Real-time prospective motion correction in MRI using image-based tracking. *Magnetic Resonance in Medicine*, 63(1):91–105.

Wollenweber, S. D., Gopalakrishnan, G., Thielemans, K., and Manjeshwar, R. M. (2012). Evaluation of the Accuracy and Robustness of a Motion Correction Algorithm for PET Using a Novel Phantom Approach. *IEEE Transactions on Nuclear Science*, 59(1):123–130.

Yang, J., Yamamoto, T., Cho, B., Seo, Y., and Keall, P. J. (2012). The impact of audiovisual biofeedback on 4D PET images: results of a phantom study. *Medical Physics*, 39(2):1046–57.

Yeh, W. C., Li, P. C., Jeng, Y. M., Hsu, H. C., Kuo, P. L., Li, M. L., Yang, P. M., and Lee, P. H. (2002). Elastic modulus measurements of human liver and correlation with pathology. *Ultrasound in medicine & biology*, 28(4):467–74.

Yoon, H. S., Ko, G. B., Il Kwon, S., Lee, C. M., Ito, M., Song, I. C., Lee, D. S., Hong, S. J., and Lee, J. S. (2012). Initial Results of Simultaneous PET/MRI Experiments with an MRI-Compatible Silicon Photomultiplier PET Scanner. *Journal of Nuclear Medicine*, 53(4):608–614.

Yushkevich, P. A., Piven, J., Hazlett, H. C., Smith, R. G., Ho, S., Gee, J. C., and Gerig, G. (2006). User-guided 3D active contour segmentation of anatomical structures: significantly improved efficiency and reliability. *Neuroimage*, 31(3):1116–28.

Zhang, T., Keller, H., O'Brien, M. J., Mackie, T. R., and Paliwal, B. (2003). Application of the spirometer in respiratory gated radiotherapy. *Medical Physics*, 30(12):3165–71.

Appendix A

Motor Units Source code

A.1 Phidgets stepper motor (C++)

The Following code corresponds to the Phidgets stepper motor algorithm, This algorithm is capable for the following actions:

- Performance of sinusoidal motion with given period and amplitude of rotation
- Performance of continuous rotation, with constant speed.
- Load text files containing motion positions and renew the position of the stepper motor every 0.110 sec
- Load files provided by motion modelling text files
- Drive Phidgets stepper motor in parallel with Arduino by triggering of the input.

```
1 // Stepper motor drive
2 //Simple driving of a stepper motor, based upon the -stepper simple - ↩
    example of phidgets library
```

```
3  //Created in 2011 by Georgios Soultanidis
4
5
6
7  #include <stdio.h>
8  #include <phidget21.h>
9  #include <unistd.h>
10 #include <time.h>
11 #include <sys/time.h>
12 #include <math.h>
13
14 #define PI 3.14159265
15 #define file_size 3315
16
17 int AttachHandler(CPhidgetHandle stepper, void *userptr)
18 {
19     int serialNo;
20     const char *name;
21
22     CPhidget_getDeviceName (stepper, &name);
23     CPhidget_getSerialNumber(stepper, &serialNo);
24     printf("%s %10d attached!\n", name, serialNo);
25
26     return 0;
27 }
28
29 int DetachHandler(CPhidgetHandle stepper, void *userptr)
30 {
31     int serialNo;
32     const char *name;
33
34     CPhidget_getDeviceName (stepper, &name);
```

```
35      CPhidget_getSerialNumber(stepper, &serialNo);
36      printf("%s %10d detached!\n", name, serialNo);
37
38      return 0;
39  }
40
41  int ErrorHandler(CPhidgetHandle stepper, void *userptr, int ErrorCode, ↩
        const char *Description)
42  {
43      printf("Error handled. %d - %s\n", ErrorCode, Description);
44      return 0;
45  }
46
47  int PositionChangeHandler(CPhidgetStepperHandle stepper, void *usrptr, ↩
        int Index, __int64 Value)
48  {
49      printf("Motor: %d > Current Position: %lld\n", Index, Value);
50      return 0;
51  }
52
53  //Display the properties of the attached phidget to the screen. We ↩
        will be displaying the name, serial number and version of the ↩
        attached device.
54  int display_properties(CPhidgetStepperHandle phid)
55  {
56      int serialNo, version, numMotors;
57      const char* ptr;
58
59      CPhidget_getDeviceType((CPhidgetHandle)phid, &ptr);
60      CPhidget_getSerialNumber((CPhidgetHandle)phid, &serialNo);
61      CPhidget_getDeviceVersion((CPhidgetHandle)phid, &version);
62
```

```
63      CPhidgetStepper_getMotorCount (phid, &numMotors);
64
65      printf("%s\n", ptr);
66      printf("Serial Number: %10d\nVersion: %8d\n# Motors: %d\n", serialNo
            , version, numMotors);
67
68      return 0;
69  }
70
71  int stepper_simple()
72  {
73      int i,test,multiplier,temp,temp2,result;
74      __int64 curr_pos,target_pos;
75      const char *err;
76      double minAccel, maxVel;
77      int stopped;
78      //float start_time;
79      clock_t start_time;
80      int s_value;
81
82      //Declare an stepper handle
83      CPhidgetStepperHandle stepper = 0;
84
85      //create the stepper object
86      CPhidgetStepper_create(&stepper);
87
88      //Set the handlers to be run when the device is plugged in or opened
            from software, unplugged or closed from software, or generates
            an error.
89      CPhidget_set_OnAttach_Handler((CPhidgetHandle)stepper, AttachHandler
            , NULL);
```

```
90    CPhidget_set_OnDetach_Handler((CPhidgetHandle)stepper, DetachHandler↩
          , NULL);
91    CPhidget_set_OnError_Handler((CPhidgetHandle)stepper, ErrorHandler, ↩
          NULL);
92
93    //Registers a callback that will run when the motor position is ↩
          changed.
94    //Requires the handle for the Phidget, the function that will be ↩
          called, and an arbitrary pointer that will be supplied to the ↩
          callback function (may be NULL).
95    CPhidgetStepper_set_OnPositionChange_Handler(stepper, ↩
          PositionChangeHandler, NULL);
96
97    //open the device for connections
98    CPhidget_open((CPhidgetHandle)stepper, -1);
99
100   //get the program to wait for an stepper device to be attached
101   printf("Waiting for Phidget to be attached....");
102   if((result = CPhidget_waitForAttachment((CPhidgetHandle)stepper, ↩
          10000)))
103   {
104      CPhidget_getErrorDescription(result, &err);
105      printf("Problem waiting for attachment: %s\n", err);
106      return 0;
107   }
108
109   //Display the properties of the attached device
110   display_properties(stepper);
111
112   //read event data
113   printf("Reading.....\n");
114
```

```
115     //This example assumes stepper motor is attached to index 0
116
117     //Set up some initial acceleration and velocity values
118     CPhidgetStepper_getAccelerationMin(stepper, 0, &minAccel);
119     CPhidgetStepper_setAcceleration(stepper, 0, minAccel*2);
120     CPhidgetStepper_getVelocityMax(stepper, 0, &maxVel);
121     CPhidgetStepper_setVelocityLimit(stepper, 0, maxVel/2);
122
123     //display current motor position if available
124     if(CPhidgetStepper_getCurrentPosition(stepper, 0, &curr_pos) == ↩
          EPHIDGET_OK)
125         printf("Motor: 0 > Current Position: %lld\n", curr_pos);
126
127     //keep displaying stepper event data until user input is read
128     printf("Press any key to continue\n");
129
130
131     //change the motor position
132     //we'll set it to a few random positions to move it around
133
134     //Step 1: Position 0 - also engage stepper
135     printf("Set to position 0 and engage. Press any key to Continue\n");
136     getchar();
137
138     CPhidgetStepper_setCurrentPosition(stepper, 0, 0);
139     CPhidgetStepper_setEngaged(stepper, 0, 1);
140
141     CPhidgetStepper_setCurrentLimit(stepper, 1, 2.5);
142
143     //*********************************
144     int speed,samples_number,maxi_displacement,temp3;
145     float time_resol,divider;
```

```
146     struct timeval tim;
147     char file_name[20];
148     FILE * tFile;
149 
150     getchar();
151 
152 
153     printf("give the name of the file to save data: ");
154     scanf("%s",file_name);
155     printf("\n %s \n",file_name);
156     tFile=fopen(&file_name,"w");
157 
158     printf("\n Case 1: sinusoidal handle \n Case 2: speed handle \n Case↩
         3: load Paul's resp file \n Case 4: load Andy's resp file \n ↩
        Case 5: drive by Arduino trigering \n choose :");
159     scanf("%d",&s_value);
160     switch (s_value) {
161        case 1:
162        {
163           printf("\n number of samples: ");
164           scanf("%d",&samples_number);
165           printf("\n maximum displacement (revs): ");
166           scanf("%d",&maxi_displacement);
167           printf("\n temporal resolution (sec per sample): ");
168           scanf("%f",&time_resol);
169           printf("\n divider ");
170           scanf("%f",&divider);
171 
172 
173           fprintf(tFile,"number of samples: %d\n maximum displacement (↩
              revs): %d\n temporal resolution (sec per sample): %f\n ↩
              divider: %f\n\n",samples_number,maxi_displacement,↩
```

```
            time_resol,divider);
174
175
176         for(i=0;i<samples_number;i++)
177         {
178             start_time=clock();
179             while((clock()-start_time)<(time_resol*CLOCKS_PER_SEC))
180             {
181             }
182             temp=(sin(i*divider))*maxi_displacement;
183
184             CPhidgetStepper_getCurrentPosition(stepper, 0, &curr_pos);
185             gettimeofday(&tim, NULL);
186             fprintf(tFile,"%d:%d : %d \n",tim.tv_sec,tim.tv_usec,↩
                    curr_pos);
187             temp2=curr_pos;
188             temp3=temp-temp2;
189             if(temp3<0)
190             {
191                 speed=temp3/(-time_resol);
192             }
193             else {
194                 speed=temp3/time_resol;
195             }
196             //printf("                temp3: %d \n                Speed: %↩
                    d \n",temp3,speed);
197             CPhidgetStepper_setVelocityLimit(stepper, 0, speed);
198
199             CPhidgetStepper_setTargetPosition (stepper, 0, temp);
200         }
201         getchar();
202         break;
```

```
203         }
204         case 2:
205         {
206             printf("\n give speed (revs per sec): ");
207             scanf("%d",&speed);
208             CPhidgetStepper_setVelocityLimit(stepper, 0, speed);
209             CPhidgetStepper_setTargetPosition (stepper, 0, 9999999999);
210             getchar();
211             break;
212         }
213         case 3:
214         {
215             float resp_sign[file_size];
216             FILE * pFile;
217             pFile = fopen ("newfile.txt","r");
218             for(i=0;i<file_size;i++)
219             {
220                 fscanf(pFile, "%f\n", &resp_sign[i]);
221             }
222             fclose(pFile);
223 
224             printf("\n maximum displacement (revs): ");
225             scanf("%d",&maxi_displacement);
226             printf("\n temporal resolution (sec per sample): ");
227             scanf("%f",&time_resol);
228 
229             for(i=0;i<file_size;i++)
230             {
231                 start_time=clock();
232                 while((clock()-start_time)<(time_resol*CLOCKS_PER_SEC))
233                 {
234                 }
```

```
235             temp=resp_sign[i]*maxi_displacement;
236
237             CPhidgetStepper_getCurrentPosition(stepper, 0, &curr_pos);
238             gettimeofday(&tim, NULL);
239             fprintf(tFile,"%d:%d : %d \n",tim.tv_sec,tim.tv_usec,↩
                    curr_pos);
240             temp2=curr_pos;
241             temp3=temp-temp2;
242             if(temp3<0)
243             {
244                 speed=temp3/(-time_resol);
245             }
246             else {
247                 speed=temp3/time_resol;
248             }
249             //printf("                temp3: %d \n                Speed: %↩
                    d \n",temp3,speed);
250             CPhidgetStepper_setVelocityLimit(stepper, 0, speed);
251
252             CPhidgetStepper_setTargetPosition (stepper, 0, temp);
253         }
254
255         break;
256     }
257     case 4:
258     {
259         float resp_sign[12050];
260         FILE * pFile;
261         pFile = fopen ("phidgets_ready_group_1.txt","r");
262         for(i=0;i<12050;i++)
263         {
264             fscanf(pFile, "%f\n", &resp_sign[i]);
```

```
265             //printf("%f\n",resp_sign[i]);
266         }
267         fclose(pFile);
268 
269         printf("\n maximum displacement (revs): ");
270         scanf("%d",&maxi_displacement);
271         printf("\n sample resolution (sec per sample): ");
272         scanf("%f",&time_resol);
273 
274         for(i=0;i<12050;i++)
275         {
276             start_time=clock();
277             while((clock()-start_time)<(time_resol*CLOCKS_PER_SEC))
278             {
279             }
280             temp=resp_sign[i]*maxi_displacement;
281 
282             CPhidgetStepper_getCurrentPosition(stepper, 0, &curr_pos);
283             gettimeofday(&tim, NULL);
284             fprintf(tFile,"%d:%d : %d \n",tim.tv_sec,tim.tv_usec,↩
                curr_pos);
285             temp2=curr_pos;
286             temp3=temp-temp2;
287             if(temp3<0)
288             {
289                 speed=temp3/(-time_resol);
290             }
291             else {
292                 speed=temp3/time_resol;
293             }
294             //printf("                temp3: %d \n                Speed: %↩
                d \n",temp3,speed);
```

```
295             CPhidgetStepper_setVelocityLimit(stepper, 0, speed);
296
297             CPhidgetStepper_setTargetPosition (stepper, 0, temp);
298          }
299
300          break;
301       }
302          case 5:
303          {
304              float resp_sign[12050];
305           FILE * pFile;
306           pFile = fopen ("phidgets_ready_group_1.txt","r");
307           for(i=0;i<12050;i++)
308           {
309              fscanf(pFile, "%f\n", &resp_sign[i]);
310              //printf("%f\n",resp_sign[i]);
311           }
312           fclose(pFile);
313
314              printf("\n maximum displacement (revs): ");
315           scanf("%d",&maxi_displacement);
316              printf("\n sample resolution (sec per sample): ");
317           scanf("%f",&time_resol);
318
319              int infinite=0;
320              int flag = PFALSE;
321              int status= PFALSE;
322              int previous_status=PFALSE;
323              int counter=0;
324
325              while(infinite==0 || counter<12050)
326              {
```

```
327
328                 while(!flag)
329                 {
330                     CPhidgetStepper_getInputState(stepper,1,&status);
331                     if(status!=previous_status)
332                     {
333                         previous_status=status;
334                         flag=PTRUE;
335                     }
336                 }
337                 flag=PFALSE;
338
339                 CPhidgetStepper_getCurrentPosition(stepper, 0, &↩
                        curr_pos);
340                 temp=resp_sign[counter]*maxi_displacement;
341             temp2=curr_pos;
342             temp3=temp-temp2;
343             if(temp3<0)
344             {
345                 speed=temp3/(-time_resol);
346             }
347             else {
348                 speed=temp3/time_resol;
349             }
350             //printf("                temp3: %d \n                Speed: %↩
                    d \n",temp3,speed);
351             CPhidgetStepper_setVelocityLimit(stepper, 0, speed);
352
353             CPhidgetStepper_setTargetPosition (stepper, 0, temp);
354                 counter++;
355             }
356
```

```
            break;
        }
    default:
        break;
}


//_-_-_-_-_-_-_-_-_-_-_-_-_-_-_-_-_-_-_-_-_-_-_-_-_-_-_-_-_-_-_-_-_-↩
   _-_-

getchar();
CPhidgetStepper_getCurrentPosition(stepper, 0, &curr_pos);
multiplier=curr_pos/3200;
//printf("miltiplier: %d \n current position: %d\n",multiplier,↩
   curr_pos);
target_pos=(multiplier*3200);
//printf("target position: %d \n",target_pos);

CPhidgetStepper_setVelocityLimit(stepper, 0, 1000);

CPhidgetStepper_setTargetPosition (stepper, 0,target_pos);
getchar();
CPhidgetStepper_setCurrentPosition(stepper, 0, 0);

fclose(tFile);


//************************

stopped = PFALSE;
while(!stopped)
{
```

```
387         CPhidgetStepper_getStopped(stepper, 0, &stopped);
388         usleep(100000);
389     }
390 
391     CPhidgetStepper_setEngaged(stepper, 0, 0);
392 
393     printf("Press any key to end\n");
394     getchar();
395 
396     //since user input has been read, this is a signal to terminate the ↩
        program so we will close the phidget and delete the object we ↩
        created
397     printf("Closing...\n");
398     CPhidget_close((CPhidgetHandle)stepper);
399     CPhidget_delete((CPhidgetHandle)stepper);
400 
401     //all done, exit
402     return 0;
403 }
404 
405 int main(int argc, char* argv[])
406 {
407     stepper_simple();
408     return 0;
409 }
```

A.2 Arduino servo drive (Python)

This code activates the USB port and reads a 4 byte number transmitted every 0.1 sec. This number corresponds to the target coordinates. Distance from current position to target posi-

tion is calculated, intervals are estimated and date is transferred to servo motor by stepping pulses.

```
1  //drive_motor_on_the_fly
2  //gets data every 0.1 sec and drives servo to the position
3  //Georgios Soultanidis
4  //15/03/12
5
6  #define maximum 12050;
7
8  int ledPin = 11;
9  int dirPin = 12;
10 int stepPin = 13;
11 int flagPin = 10;
12 int flagState=LOW;
13 int i;
14 int time_gap;
15 double temp;
16 int incomingByte = 0;
17 char* val="0";
18
19 double interval_usec=100000;
20 int counter=0;
21 boolean flag=true;
22 boolean flag2=false;
23 int array[6];
24 short previous_position;
25 short targ_position;
26 int steps;
27
28 void setup()
```

```
29 {
30   // begin the serial communication
31   pinMode(2, OUTPUT);
32   pinMode(3, OUTPUT);
33   pinMode(4, OUTPUT);
34   pinMode(5, INPUT);
35   pinMode(flagPin ,OUTPUT);
36
37   pinMode(dirPin, OUTPUT);
38   pinMode(stepPin, OUTPUT);
39
40
41   digitalWrite(2, HIGH);
42   delay(100);
43   digitalWrite(3, HIGH);
44   delay(100);
45   digitalWrite(4, HIGH);
46   delay(100);
47   digitalWrite(2, LOW);
48   delay(100);
49   digitalWrite(3, LOW);
50   delay(100);
51   digitalWrite(4, LOW);
52   delay(100);
53   Serial.begin(14400);
54   pinMode(ledPin, OUTPUT);
55   digitalWrite(3, HIGH);
56   digitalWrite(flagPin, LOW);
57
58 }
59
60 void loop()
```

```
61 {
62
63   digitalWrite(3, LOW);
64   digitalWrite(4, HIGH);
65
66   while(flag==true)
67   {
68     flag2=false;
69     while(flag2==false)
70     {
71       if (Serial.available())
72       {
73         incomingByte = Serial.read();
74         if(incomingByte==115)
75         {
76
77           Serial.println(counter);
78           for(int i=0;i<6;i+=1)
79           {
80             val[0] = Serial.read();
81
82             int a = atoi(val);
83             Serial.println(a);
84             array[i]=a;
85             Serial.flush();
86           }
87           Serial.println("e");
88           previous_position=targ_position;
89           targ_position=array[1]*10000+array[2]*1000+array[3]*100+array↩
                 [4]*10+array[5]*1;
90           steps=(targ_position-previous_position)/10;
91           time_gap=abs(int(interval_usec/ steps))-4;
```

```
92            Serial.println(" ");
93            Serial.println(steps);
94            Serial.println(" ");
95            Serial.println(time_gap);
96            Serial.println(" ");
97
98            flag2=true;
99          }
100       }
101
102     }
103     if(flagState==LOW)
104     {
105       flagState=HIGH;
106     }
107     else
108     {
109       flagState=LOW;
110     }
111     digitalWrite(flagPin, flagState);
112
113     if(steps<0)
114     {
115       digitalWrite(dirPin,HIGH);
116       temp=abs(steps);
117       for(i=0;i<temp;i+=1)
118       {
119         unsigned long startMicros = micros();
120         digitalWrite(stepPin, HIGH);
121         delayMicroseconds(2);
122         digitalWrite(stepPin, LOW);
123         unsigned long currentMicros = micros();
```

```
124           while(currentMicros-startMicros<time_gap)
125           {
126             currentMicros=micros();
127           }
128         }
129       }
130       else if(steps>0)
131       {
132         digitalWrite(dirPin,LOW);
133         for(i=0;i<steps;i+=1)
134         {
135           unsigned long startMicros = micros();
136           digitalWrite(stepPin, HIGH);
137           delayMicroseconds(1);
138           digitalWrite(stepPin, LOW);
139           unsigned long currentMicros = micros();
140           while(currentMicros-startMicros<time_gap)
141           {
142             currentMicros=micros();
143           }
144         }
145       }
146       else
147       {
148         delay(100);
149       }
150
151
152     }
153
154 }
```

A.3 USB broadcast (Java)

This code is the transmitter of the coordinates, given by a text file and transmits the 4 byte coordinates via USB to arduino.

```
import processing.serial.*;

int mySwitch=0;
boolean flag2=false;
int counter=1;
char input;
char test;
String [] subtext;
String [] feedback;
Serial myPort;

void setup() {
  mySwitch=1;

  myPort = new Serial(this, "/dev/tty.usbmodem641", 14400);
  myPort.bufferUntil('\n');
  println("reset Arduino");
  delay(5000);
  println("begin transmision");
}

void draw() {
  if (mySwitch>0) {
    readData("/Users/georgiossoultanidis/arduino/resp_data/↩
        ready_group_3_60%.txt");
    mySwitch=0;
```

```
26  }
27  if (counter<subtext.length)
28  {
29    myPort.write("s");
30    test=subtext[counter].charAt(0);
31    myPort.write(test);
32    test=subtext[counter+1].charAt(0);
33    myPort.write(test);
34    test=subtext[counter+2].charAt(0);
35    myPort.write(test);
36    test=subtext[counter+3].charAt(0);
37    myPort.write(test);
38    test=subtext[counter+4].charAt(0);
39    myPort.write(test);
40    flag2=false;
41    while (flag2==false)
42    {
43      if (myPort.available()>0)
44      {
45        int inByte = myPort.read();
46        if (inByte==101)
47        {
48          flag2=true;
49          counter++;
50          counter++;
51          counter++;
52          counter++;
53          counter++;
54        }
55      }
56    }
57  }
```

```
58   else {
59     while (myPort.available () > 0)
60     {
61       int inByte = myPort.read();
62       char tt=char(inByte);
63       println(tt);
64     }
65   }
66 }
67
68
69 /* The following function will read from a CSV or TXT file */
70 void readData(String myFileName) {
71
72   File file=new File(myFileName);
73   BufferedReader br=null;
74   try {
75     br=new BufferedReader(new java.io.FileReader(file));
76     String text=null;
77     /* keep reading each line until you get to the end of the file */
78     while ( (text=br.readLine ())!=null) {
79       /* Spilt each line up into bits and pieces using a comma as a ↩
             separator */
80       subtext = splitTokens(text, ",");
81     }
82   }
83   catch(java.io.FileNotFoundException e) {
84     e.printStackTrace();
85   }
86   catch(IOException e) {
87     e.printStackTrace();
88   }
```

```
89    finally {
90      try {
91        if (br != null) {
92          br.close();
93        }
94      }
95      catch (IOException e) {
96        e.printStackTrace();
97      }
98    }
99  }
```